Fermi surface study of organic conductors by magnetooptical measurements

Oshima, Yugo

博士論文

Fermi Surface Study of Organic Conductors by Magnetooptical Measurements
（有機導体フェルミ面の磁気光学的研究）

平成15年3月

神戸大学大学院自然科学研究科

大島勇吾

Fermi Surface Study of Organic Conductors by Magnetooptical Measurements
有機導体フェルミ面の磁気光学的研究

Yugo Oshima
大島勇吾

(February 14, 2003)

Contents

1. General Introduction

1.1. Introduction

For a long time, organic molecules have been considered that they do *not* conduct electricity like metals. In fact, organic polymer, molecules that repeat their structure periodically in long chains, is used as an insulation around the conducting copper wires in electric cable, and it has been our common image of metals and organic molecules. However, if electrons are removed (through oxidation) or introduced (through reduction) from the polymer, these 'holes' and extra electrons can move along the molecule and becomes electrically conductive. Therefore, in the year 2000, Alan J. Heeger, Alan G. MacDiarmid and Hideki Shirakawa have been awarded the Nobel Prize in chemistry for their discovery and development of conducting polymers. Besides the discovery of these conducting polymers, another kind of "synthetic metal" has been developed which is known as an organic conductor (*or* molecular conductor). The organic conductor is literally a conductor in which the organic molecule is the constituent element of the crystal and electronic structure. In principle, the difference between the conducting polymer and organic conductor is that the former is a huge molecule which is composed of infinite atoms connected by the covalent bond, while the latter is a crystal where relatively small molecules are assembled by an interaction weaker than the covalent bond and these organic conductors have afforded many research topics both in chemistry and physics for the past few decades. The most striking event is the discovery of superconductivity in a series of quasi-one-dimensional (q1D) organic conductors, TMTSF salts [1,2], followed by a variety of quasi-two-dimensional (q2D) conductors, BEDT-TTF salts [2]. And besides, a lot of other peculiar physical phenomena, such as charge density wave (CDW) and spin density wave (SDW), have been revealed in organic conductors, which are closely related with the low dimensionality of their electronic structures. Therefore, the richness of these physical properties have activated many experimental and theoretical studies and it has been widely accepted that the electronic structures or the Fermi surface (FS) topologies play an important role in the physical properties of these materials. For this reason, the FS topologies of these salts have been studied by various high magnetic field techniques such as the measurements of Shubnikov-de Haas oscillation (SdH), de Haas-van Alphen oscillation (dHvA) and angle dependent magnetoresistance oscillation (ADMRO) [3]. Another useful technique is the 'magnetooptical measurements' which is becoming nowadays a powerful tool for FS studies. And the observation of cyclotron resonance (CR) is one of the useful and well-known technique in magnetooptical measurements. From CR measurements, we can obtain directly the information of carrier's effective mass and scattering time. Furthermore, it is also possible to speculate about the shape of the FS from angular dependence measurements of CR. After the discovery of CR in semiconductors [4] and Azbel'-Kaner type CR in metals [5], CR measurements have been performed in a variety of materials such as GaAs, alkali metals, semimetals, Cu, Sn etc. . However, few CR (or magnetooptical) measurements have been performed for organic conductors in contrast to SdH, dHvA and ADMRO measurements. For example, one of the interesting organic conductor is α-(BEDT-TTF$)_2$KHg(SCN$)_4$. It has an antiferromagnetic order below 12 K which is considered to be caused by a SDW formation [6]. Although a recently proposed B-T phase diagram based on magnetic torque measurements or NMR measurements favors a CDW scenario [7,8], there still exists no clear evidence for a lattice modulation. Therefore, the ground state of this phase is quite complex and is still under discussion. We have performed magnetooptical measurements of this salt and observed four CRs in which each effective mass was smaller than those obtained by dHvA and SdH measurements [9]. It was pointed out earlier by Singleton *et al.* [10] that this difference can be explained by the "Kohn's theorem" [11] which suggests that the CR's effective mass is independent of the electron-electron interaction and the effective mass deduced from quantum oscillation measurements is enhanced due to the not negligible electron-electron interaction in the system. However, the FS structure of this salt is very complex due to the nesting of the FS at the density wave state. Therefore, we could not clarify which resonance corresponds to the FS's closed orbit. Besides, recent magnetooptical measurements studies have shown that the mechanism responsible for the resonant absorption is quite different from the well-known conventional CR, and novel magnetooptical resonances such as periodic orbit resonance (POR) [12] and Fermi traversal resonance (FTR) [13] are proposed. The detail of these novel resonance will be described in the latter part, and we will show that some groups have reported the observation of these novel resonances in organic conductors [12-16]. As mentioned above, the FS of α-(BEDT-TTF$)_2$KHg(SCN$)_4$ is quite complex, and the observation of these novel resonances have more complicated the situation. Therefore, we have focus on the organic conductors which have a simple FS. By performing magnetooptical measurements on these kinds of salt, we will have a better understanding of the relationship between the cyclotron effective mass and Kohn's theorem, and these novel magnetooptical resonances.

1.2. The purpose of this study

This study treats the observation of a conventional CR and a novel resonance, such as POR, in several organic conductors by performing magnetooptical measurements. Measurements of q2D organic conductor θ-(BEDT-TTF)$_2$I$_3$, (BEDT-TTF)$_2$Br(DIA), (BEDT-TTF)$_3$Br(pBIB) and (BEDT-TTF)$_3$Cl(DFBIB), where all of them have a relatively simple q2D FS structure, will be presented. The details of their FS structures will be described below, however, θ-(BEDT-TTF)$_2$I$_3$ has one closed orbit and a magnetic breakdown orbit, (BEDT-TTF)$_2$Br(DIA) has only one closed orbit but an anisotropic one, (BEDT-TTF)$_3$Br(pBIB) and (BEDT-TTF)$_3$Cl(DFBIB) have also a closed orbit but the carrier density is different with the other two. From the resonance position and the linewidth, the cyclotron effective mass and the scattering time will be obtained, respectively. These obtained values will be compared with those obtained from the quantum oscillation (SdH or dHvA) measurements and the effect of interactions on the effective mass will be discussed. If there exists effective mass difference between the CR and quantum oscillations measurements, this means that the Kohn's theorem is valid (i.e. the electron-electron interactions do not contribute to the CR's effective mass) and the contribution of the interactions in the system can be argued (see also section 3.3.2). There are not many studies which treated the estimation of the contribution of electron-electron interactions. Therefore, it is worth to treat the comparison of the effective masses in this study. Furthermore, the selection rule in the observation of conventional CR and novel resonance will be discussed from the skindepth for each sample. Finally, measurements of q1D organic conductor (DMET)$_2$I$_3$ will be presented, in which the interesting novel resonance coming from q1D FS structure was observed. The Fermi velocity and the scattering time can be obtained from this novel resonance and the obtained values will be discussed and compared with the results of other measurements.

The contents of this thesis are organized as follows. Basic properties of organic conductors such as crystal and electronic structures will be explained in chapter 2. High magnetic field techniques for band structure measuring will be described in chapter 3, starting with the well known quantum oscillation measurements (SdH, dHvA oscillations) followed by ADMRO measurements and the basic principles of magnetooptical measurements. In chapter 4, experimental results of the q2D organic conductors are given. Next, experimental results of q1D organic conductor $(DMET)_2I_3$ will be described in chapter 5. Finally, the concluding remarks for the present thesis are given in chapter 6.

2. Principal Properties and Basic Principles

2.1. Charge transfer salts

Basically, the organic conductor consists of *donor* molecule and *acceptor* molecule. Figure 2-1 shows the typical organic *donor* and *acceptor* molecules which are used in organic conductors. The donor molecule becomes a cation (positive ion) by releasing its electron, while the acceptor molecule becomes an anion (negative ion) by accepting an electron. And both molecules can easily become an ionized radical. Therefore, if we combine both donor and acceptor molecules, electrons will move from the donor molecules to the acceptor molecules which will generate cation and anion radicals, and these radicals will form a salt. This is the reason why organic conductors are also called charge transfer salts.

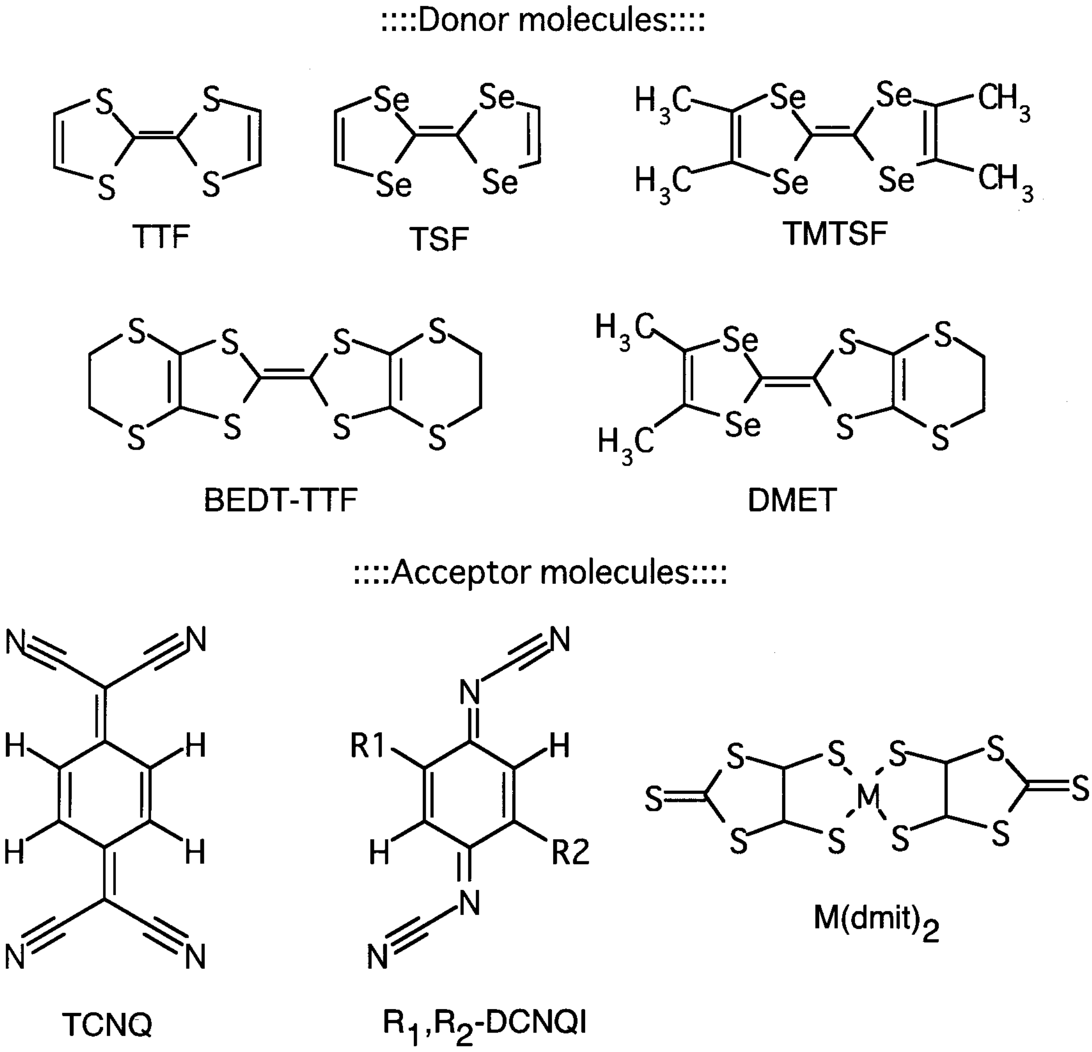

Fig. 2-1 Typical organic donor and acceptor molecules which are used in the organic conductors.

The typical derivative made from two radicals is, for example, TTF-TCNQ where the donor molecule TTF is the abbreviation of tetrathiafulvalene and the acceptor molecule TCNQ is tetracyano-p-quinodimethane. However, organic conductors are normally made from one donor (or acceptor) molecule and a simple anion (or cation) such as I_3^-, Br^-, Cl^- (or NH_4^+, Ag^+). In this case, the formed salt consists of one radical and a closed shell ion. The donor molecules have a roughly flat shape as shown in Fig. 2-1, and the molecular π-orbitals are spread out perpendicular to the molecular plane. Therefore, the donor molecules stack next to each other so that the molecular π-orbitals overlap; this enables the electrons to transfer from molecule to molecule; and form a conductive layer by releasing its electron. On the other hand, the anions form a insulating layer by accepting the released electrons. In BEDT-TTF salts, where BEDT-TTF is an abbreviation for bis(ethylenedithio) tetrathia-fulvalene, the BEDT-TTF molecules can stack in many different ways. These polymorphic phases are denoted by α, β, κ, θ, etc. and some examples of molecular stacking are shown in Fig. 2-2.

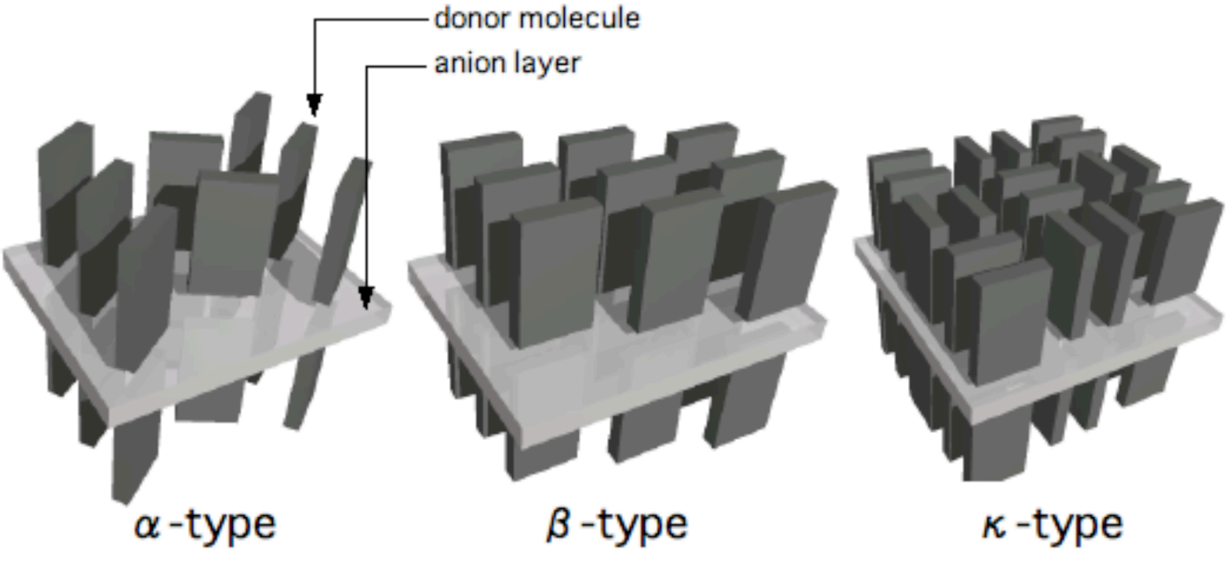

Fig. 2-2 Example of molecular stacking in organic conductors (α, β, κ -type)

The dimensionality of organic conductors strongly depend on the arrangement of the molecular packing. Within the donor molecule layer, the molecules are close enough to allow the overlapping of the molecular π orbital which means the transfer integrals of carriers for hopping between the donor molecule will be relatively large. On the other hand, in the interlayer direction, the donor molecules are well separated from each other by the sandwiched insulating anion layer which means the transfer integral will be much smaller in this direction. Therefore, it results in band structures and electronic properties which, for many purposes, can be considered to be q2D. However, not always q2D, because some β-type salts have larger transfer integral in the lateral direction than the stacking direction and this will lead to a q1D band structure. Moreover, the length between the donor molecule and the size of unit cell can be varied by using different anions. Hence, the physical properties and the FS can be different even if it has the same crystal structure with different anions.

2.2. Band structure

One peculiarity in organic conductors is the lucidity of its electronic structure. Because the constituent element of organic conductors is composed of molecules which are strongly independent (nevertheless the molecules have complicated structure), we only have to consider the situation that carriers are hopping between the molecules when calculating the electronic structure. Therefore, calculating the electronic structure of the organic conductor is much more easier than the conventional metal. This calculation approach is based upon the extreme situation that carriers are tightly bound with molecules and these carriers move to another adjacent molecule which is well-known as a tight-binding approximation. However, the point of this calculation method is that the transfer integral is calculated from the overlapping of the wavefunction, and it is called the extended Hückel method. This method has been employed on various organic conductors by different authors [17-20] and it was proved by many experimental results that this band calculation method is valid to explain the electronic structure of organic conductors.

First, let us treat the electronic structure of organic conductors in a generalized crystal lattice (Fig. 2-3).

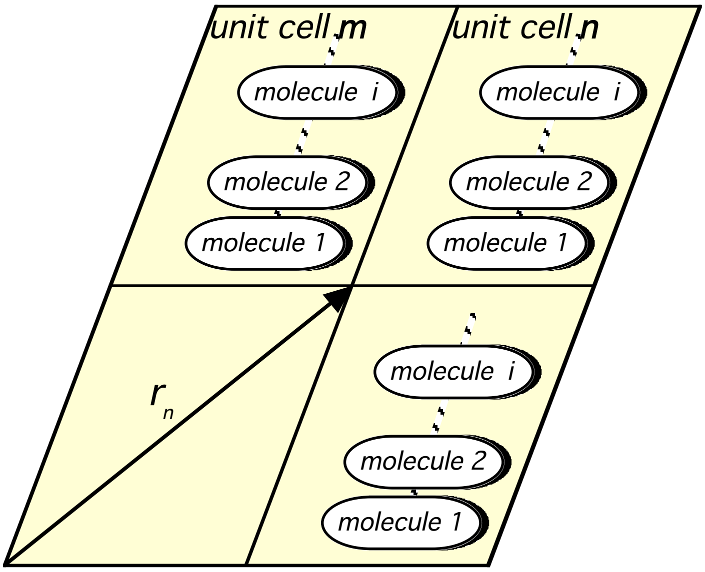

Fig. 2-3 Generalized crystal lattice for an organic conductor.

If we define the wavefunction for carriers which are at the molecule *i* of unit cell *n* as $c_{n,i}(t)$ and the transfer integral where carriers hop from molecule *j* of unit cell *m* to molecule *i* of unit cell *n* as $<n,i|H|m,j>$, the Hamiltonian equation for wavefunction $c_{n,i}(t)$ can be written as follows,

$$i\hbar\frac{dc_{n,i}(t)}{dt}=\sum_m\sum_j\langle n,i|H|m,j\rangle c_{m,j}(t). \qquad (2.1)$$

The wavefunction in a steady state can be described as $c_{n,i}(t)=A_{n,i}e^{-(i/\hbar)Et}$ and eq.(2.1) becomes

$$EA_{n,i}=E_iA_{n,i}+\sum_m\sum_j\langle n,i|H|m,j\rangle A_{m,j} \qquad (2.2)$$

where E_i is the diagonal component of the Hamiltonian matrix and it corresponds to the molecular orbital energy of molecule *i*. If we substitute $A_{n,i}=A_ie^{ikr_n}$ which is time-independent for eq.(2.2), we have

$$\left(E_i-E\right)A_i+\sum_m\sum_j\langle n,i|H|m,j\rangle A_je^{ik(r_m-r_n)}=0 \qquad (2.3)$$

and thus for a non-trivial solution, we have

$$\begin{vmatrix} E_1+\sum_m\langle n,1|H|m,1\rangle e^{ik(r_m-r_n)}-E & \sum_m\langle n,1|H|m,2\rangle e^{ik(r_m-r_n)} & \cdots \\ \sum_m\langle n,2|H|m,1\rangle e^{ik(r_m-r_n)} & E_2+\sum_m\langle n,2|H|m,2\rangle e^{ik(r_m-r_n)}-E & \cdots \\ \vdots & \vdots & \ddots \end{vmatrix}=0. \qquad (2.4)$$

From the solution of eq.(2.4), we can obtain the energy band *E(k)*. Now then, we will apply this method to the real system where molecules are stacked as shown in Fig. 2-4.

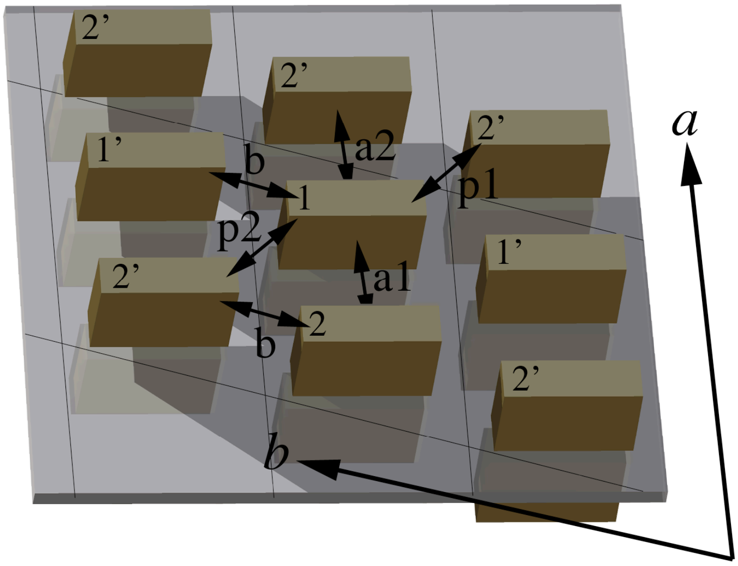

Fig. 2-4 Intermolecular interactions in β-type-like stacking.

Figure 2-4 shows the donor arrangement viewed from the axis perpendicular to *ab*-plane. The blocks represent donor molecules (BEDT-TTF, TMTSF, DMET, etc.) and each unit cell contains two donor molecules. Besides, the symmetrical translation of molecule 1 and molecule 2 is displayed by an apostrophe added on the number. As shown in Fig. 2-4, the flat donor molecules are stacked next to each other along *a*-axis. Intermolecular distance is closer along the *b*-axis rather than *a*-axis. However, this does not mean that the intermolecular interaction is larger along the *b*-axis. The hopping probability must be evaluated from the overlapping integrals of the molecular orbitals. Assuming that the donor molecules are dimerized, each intermolecular interaction will be described by the arrows with the specific letter a1, a2, b, p1 and p2 as shown in Fig. 2-4. In this case, we only have to consider the hopping of carriers from molecule 1 to 1, 1 to 2, 2 to 1 and 2 to 2. Therefore, transfer integrals of eq.(2.4) can be written as

$$\begin{aligned}&\sum_m \langle n,1|H|m,1\rangle e^{ik(r_m-r_n)} = \sum_m \langle n,2|H|m,2\rangle e^{ik(r_m-r_n)} = 2t_b\cos kb\\&\sum_m \langle n,1|H|m,2\rangle e^{ik(r_m-r_n)} = \left(\sum_m \langle n,2|H|m,1\rangle e^{ik(r_m-r_n)}\right)^* = t_{a1}+t_{a2}e^{ika}+t_{p1}e^{ik(a-b)}+t_{p2}e^{ikb}\end{aligned} \quad ,(2.5)$$

and if we took the origin of *E* to the molecular orbital energy level, eq.(2.4) becomes

$$\begin{vmatrix} 2t_b\cos kb - E & t_{a1} + t_{a2}e^{ika} + t_{p1}e^{ik(a-b)} + t_{p2}e^{ikb} \\ \left(t_{a1} + t_{a2}e^{ika} + t_{p1}e^{ik(a-b)} + t_{p2}e^{ikb}\right)^* & 2t_b\cos kb - E \end{vmatrix} = 0. \qquad (2.6)$$

By solving eq.(2.6), the following dispersion relation is obtained;

$$\begin{aligned} &E(k) = 2t_b\cos kb \pm \Delta^{1/2}, \\ &\Delta = t_{a1}^2 + t_{a2}^2 + t_{p1}^2 + t_{p2}^2 + 2t_{a1}t_{a2}\cos ka + 2(t_{a1}t_{p2} + t_{a2}t_{p1})\cos kb \qquad (2.7) \\ &+2(t_{a1}t_{p1} + t_{a2}t_{p2})\cos k(a-b) + 2t_{p1}t_{p2}\cos k(a-2b). \end{aligned}$$

The overlapping integrals of donor molecules S is obtained from the molecular orbitals of single molecule which are calculated by means of the extended Hückel method [19, 20] and the transfer integrals t are estimated using the relation $t=ES$ (E~-10eV). For example, estimated transfer integrals in eV for TMTTF salts are t_{a1}=-0.20, t_{a2}=-0.23, t_b=-0.035, t_{p1}=0.007, t_{p2}=0.020 [20]. If we put these values to eq.(2.7), band structure is obtained as shown in Fig. 2-5. The unit cell contains two donor molecules in Fig. 2-4 which means this kind of salt will form a D_2X compound where D is a donor molecule and X is an anion. As mentioned in the previous section, the donors release their electrons to the anions whose formal charge is -1. Therefore, the formal charge of a donor becomes +1/2 for D_2X compound. This means that the band is 3/4 filled because the formal charge is +2 when the highest occupied molecular orbital (HOMO) band is empty. If we numerically fill the band structure of Fig. 2-5 to 3/4, obtained FS shows a q1D structure. Most of the Bechgaard salts, where donor molecules D is TMTSF or TMTTF, have a crystal structures similar to Fig. 2-4, which leads to the q1D electronic structure.

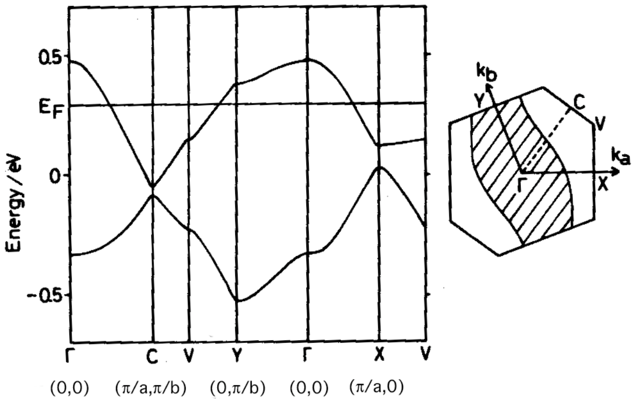

Fig. 2-5 Band structure and Fermi surface of $(TMTTF)_2X$. [20]

However, BEDT-TTF salts have a variety of crystal structures which lead to its richness of the electronic structure. Next in Fig. 2-6, we show the typical electronic structure of BEDT-TTF salts for different type of crystal structure.

θ-type has a relatively simple crystal structure. It looks like that it has a column in the *c*-axis, however, the intermolecular overlap is small in this direction and each BEDT-TTF is surrounded by six BEDT-TTF molecules forming a close packed structure in the *ac*-plane. Thus, the hopping transfer is isotropic which will lead to a cylindrical FS.

In κ-type, BEDT-TTF molecules form dimers where adjacent pairs are rotated by approximately 90° with respect to each other. The inter-dimer interaction is two-dimensional which will lead to a cylindrical FS as well.

On the other hand, the electronic structure of β-type BEDT-TTF salts are very sensitive to the difference of the anions. Basically, β-type salts are dimerized in the *p* direction and the electronic structure shows q1D structure, especially for Bechgaard salts, as mentioned above. However, the interaction are well-balanced in the *r,q* direction for β-type BEDT-TTF salts which lead to a typical cylindrical FS. However, depending on some anions, the crystal structure will change to the β'-type crystal structure. In this case, there will be a uniform interaction in the *r* direction and the band structure will be q1D. Of course, there are some exceptions concerning the electronic structure of some α,κ,β-type salts, but most of the cases can be explained by this method. And for whom that are more interested, Mori has summarized the structural properties of virtually all known BEDT-TTF salts in three excellent review articles [21-23].

<θ-type>

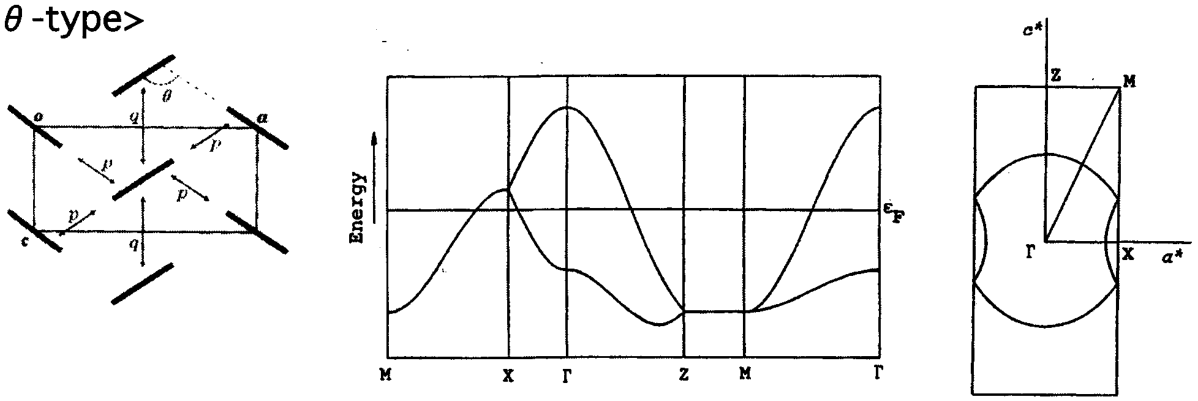

<κ-type>

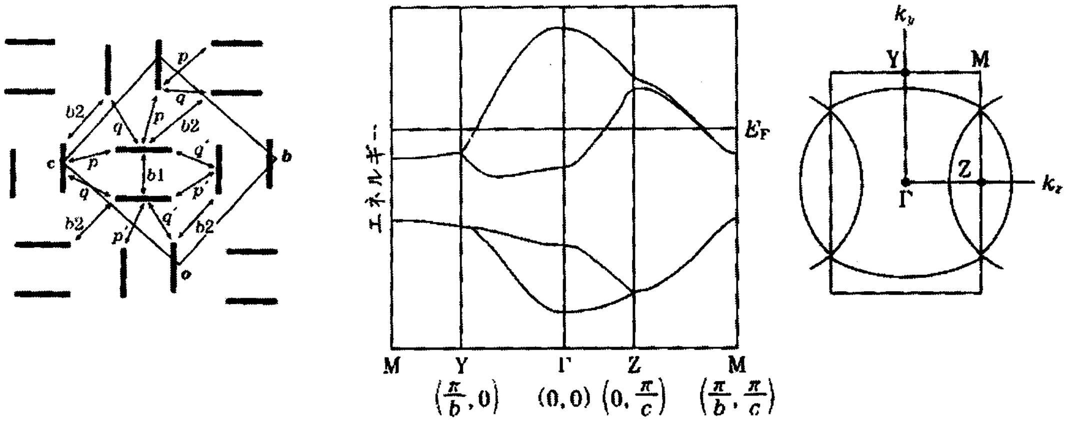

<β-type>

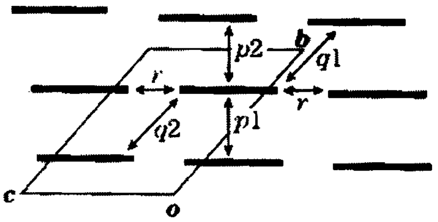

X	$S/10^{-3}$ I_3	ICl_2
$p1$	15.4	15.4
$p2$	5.6	−1.7
$q1$	4.7	7.2
$q2$	1.8	1.7
r	−2.0	0.1

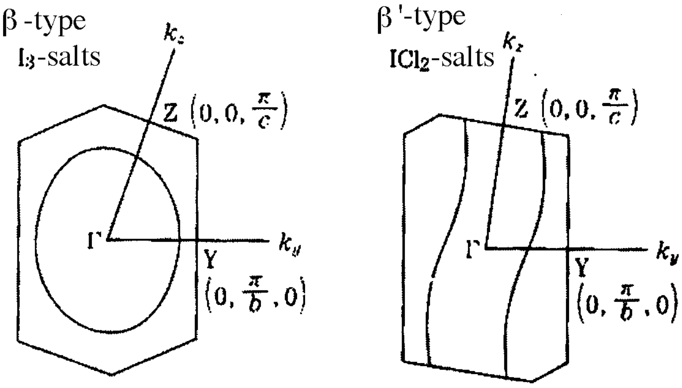
β-type I_3-salts

β'-type ICl_2-salts

Fig. 2-6 Molecular arrangement and electronic structure of θ, κ, β-type BEDT-TTF salts.

2.3. Landau quantization

There are a lot of band structure measuring techniques, such as SdH, dHvA and CR measurements, which use magnetic field to partially quantize the electronic motion. In this section, we shall treat the motion of electrons under magnetic field and we will see that the orbits of electrons will be quantized; this is known as Landau quantization.

First, let us consider the equation of motion of a band electron under an external magnetic field $\vec{B}$, i.e.

$$\hbar \frac{d\vec{k}}{dt} = -e\vec{v} \times \vec{B}, \qquad (2.8)$$

where the right-hand side is the well-known Lorentz force. Eq.(2.8) implies that the component of $\vec{k}$ parallel to $\vec{B}$ is constant as $d\vec{k}/dt$ is perpendicular to $\vec{v}$. We know that the group velocity can be written as

$$\vec{v} = \frac{1}{\hbar} \nabla_k E(k). \qquad (2.9)$$

Therefore, $d\vec{k}/dt$ will be perpendicular to $\nabla_k E(k)$ which means that the electron orbit is a constant energy. In *k*-space, the electron orbits are described by the intersection of surfaces of constant energy with plane perpendicular to $\vec{B}$ and this electron under the magnetic field will follow the orbit and oscillates with the angular frequency ω_c (i.e. cyclotron motion) where ω_c is known as cyclotron frequency and can be written as

$$\omega_c = \frac{eB}{m^*}. \qquad (2.10)$$

Now, if we consider the momentum of an electron under magnetic field, the momentum p can be described as follows,

$$\vec{p} = \hbar\vec{k} - e\vec{A}, \ \vec{B} = \nabla \times \vec{A}, \qquad (2.11)$$

where $\vec{A}$ is the magnetic vector potential (or Landau Gauge). And from the Bohr's quantization condition, the orbit under magnetic field will be quantize as,

$$\oint \vec{p} \cdot d\vec{r} = (n+\gamma)h = 2\pi(n+\gamma)\hbar, \qquad (2.12)$$

where γ is the phase factor (γ is 1/2 for a free electron) and n is an integer.
By integrating eq.(2.8) with time and using eqs.(2.11) and (2.12), we have

$$\oint \vec{p} \cdot d\vec{r} = \oint \hbar\vec{k} \cdot d\vec{r} - \oint e\vec{A} \cdot d\vec{r} = -e\oint \left(\vec{r} \times \vec{B}\right) \cdot d\vec{r} - e\int \left(\nabla \times \vec{A}\right) \cdot d\vec{\sigma}$$

$$= e\oint \vec{B} \cdot \left(\vec{r} \times d\vec{r}\right) - e\int \vec{B} \cdot d\vec{\sigma} = 2e\Phi - e\Phi = e\Phi, \qquad (2.13)$$

where Φ is the magnetic flux. Consequently, from eqs.(2.12) and (2.13), the flux will be quantize as

$$\Phi = \frac{2\pi\hbar}{e}\left(n+\frac{1}{2}\right). \qquad (2.14)$$

Here, from eq.(2.8), the relationship of the orbit's area between real space and *k*-space is

$$A_r = \left(\frac{\hbar}{eB}\right)^2 A_k, \qquad (2.15)$$

and we can describe the flux by *k*-space by using eq.(2.15) which becomes

$$\Phi = BA_r = B\left(\frac{\hbar}{eB}\right)^2 A_k = \left(\frac{\hbar}{e}\right)^2 \frac{A_k}{B}. \qquad (2.16)$$

Therefore, from eqs.(2.14) and (2.16), the relation between the orbit's area *A* in *k*-space and the magnetic field *B* will be

$$A = A_k = \left(n+\frac{1}{2}\right)\frac{2\pi e}{\hbar}B. \qquad (2.17)$$

If we separate the wave vector *k* to the wave vector perpendicular and parallel to the field, the eigen energy of free electron can be written as

$$\varepsilon = \frac{\hbar^2}{2m_e}\left(k_{plane}^2 + k_z^2\right) = \frac{\hbar^2}{2m_e}\left(\frac{A}{\pi} + k_z^2\right). \qquad (2.18)$$

Then, from eqs.(2.17) and (2.18), we have

$$\varepsilon = \hbar\frac{eB}{m_e}\left(n+\frac{1}{2}\right) + \frac{\hbar^2}{2m_e}k_z^2. \qquad (2.19)$$

If we treat eq.(2.19) in a 2D electron system, the second term of eq.(2.19) will be zero and from eq.(2.10), we obtain

$$\varepsilon = \hbar\omega_c\left(n+\frac{1}{2}\right). \qquad (2.20)$$

Therefore, we can see that the energy of electron's motion under the magnetic field is completely quantized and these quantized energy levels are called Landau levels. We will show in the next chapter, some high field techniques which use this Landau quantization. However, we have considered above in the case of free electron, but in practice, we will have to replace the mass of free electron m_e to the effective mass m^* for Bloch electrons.

2.4. Organic conductors which have a simple Fermi surface

Before we enter the next chapter, we will give a short introduction of the sample we have measured for this study. We note that the aim of this study is to perform magnetooptical measurements of the organic conductors which have a simple FS. Therefore, we have tried to choose organic conductors whose transport measurements have already been done and the FS is well known. We will show some basic properties and also the results of band structure measuring measurements of the sample. Therefore, we advice for the reader who are not familiar with these measurement techniques (i.e. dHvA, SdH and ADMRO) to read the next section first.

-θ-(BEDT-TTF)$_2$I$_3$-

θ-(BEDT-TTF)$_2$I$_3$ was first discovered on the way of developing the organic superconductor β-(BEDT-TTF)$_2$(I$_3$)$_{1-x}$(AuI$_2$)$_x$ from the aim of controlling the transition temperature T_c by introducing impurities in the anion sites [24]. However, it was found that the obtained crystal was an unexpected new conductor which has a θ-type crystal structure [25]. We show in Fig. 2-7, the orthorhombic crystal structure of θ-(BEDT-TTF)$_2$I$_3$ viewed from the *b*-axis where each BEDT-TTF is surrounded by six BEDT-TTF molecules forming a close packed structure in the *ac*-plane [25] and the hopping transfer is isotropic which means that the FS will be cylindrical.

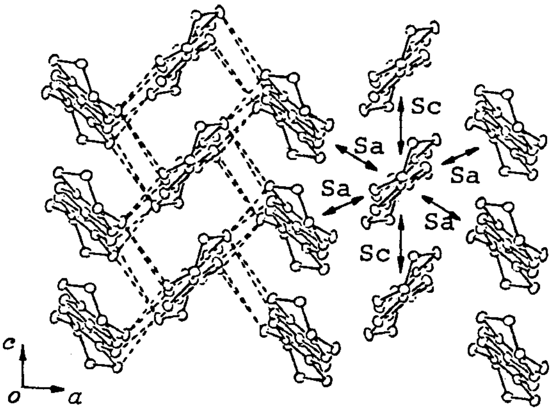

Fig. 2-7 The crystal structure of θ-(BEDT-TTF)$_2$I$_3$. [25]

Fig. 2-8 shows the in-plane resistivity measurements of several θ-(BEDT-TTF)$_2$I$_3$. The conductivity at room temperature is around 50 Scm^{-1}, however, some samples show a superconducting transition at T_c=3.6 K and some do not show any phase transition at low temperature [26].

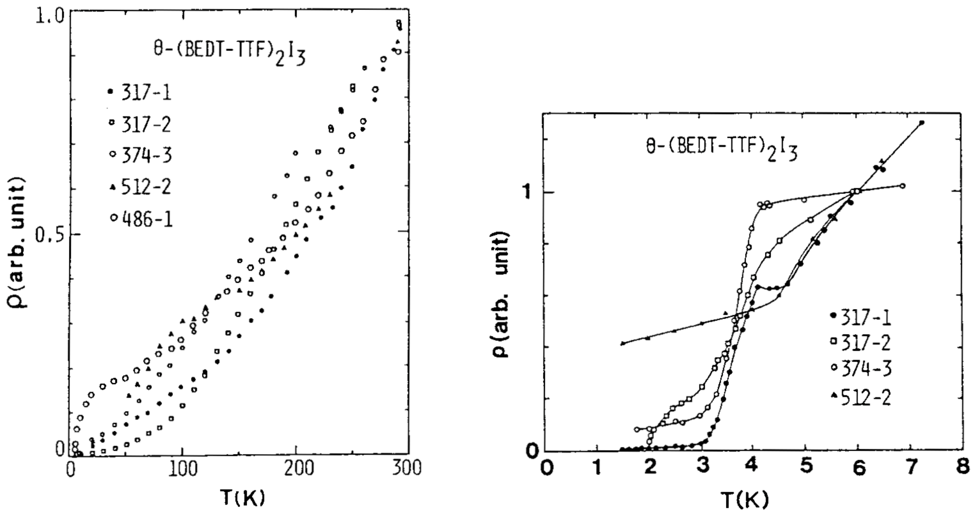

Fig. 2-8 The in-plane resistivity of θ-(BEDT-TTF)$_2$I$_3$ as a function of temperature. [26]

We now know, from X-ray analysis, that this sample dependence comes from the unique character of θ-(BEDT-TTF)$_2$I$_3$ where most of the sample have twin domain and the superconductivity is thought to occur at the boundary of this twin domain [27,28]. Therefore, it is known that high purity samples are metallic and do not show any phase transition at low temperature [29]. Moreover, the residual resistivity ratio (RRR), where RRR is the resistivity ratio of room temperature and liquid helium temperature, is nearly 1000 for θ-(BEDT-TTF)$_2$I$_3$ which suggests very good sample quality. On the other hand, the FS structure of θ-(BEDT-TTF)$_2$I$_3$ has taken a long time to come to a conclusion due to its twin domain character. There are two ways of describing the crystal structure, one is the orthorhombic crystal structure which is based on an 'average' of the crystal structure of the twin domain, and the other is monoclinic structure where the sublattices of the I_3 molecule are considered (this one is considered to be the final crystal structure) [27]. The relation of the crystal axes between monoclinic and orthorhombic crystal structure are $a_m=2c_o$, $b_m=a_o$, $c_m=b_o$-c_o where the subindexes *m* and *o* correspond to monoclinic and orthorhombic, respectively.

In Fig. 2-9, we show the band calculation of θ-(BEDT-TTF)$_2$I$_3$ considering the orthorhombic crystal structure (Fig. 2-7) [25]. The band calculation has been done by the extended Hückel method (see section 2.2) and the overlap integral, as seen in Fig. 2-7, is taken as S_c=-6.4x10^{-3}, S_a=-4.2x10^{-3}. The energy band has a relatively simple structure which is degenerated between ZM and MX and the FS shows an ideal 2D shape. However, FS formed a closed pocket along MX, because the lattice constant a_o is twice the value of c_o. On the other hand, Tamura *et al.* have measured the optical reflectance of θ-(BEDT-TTF)$_2$I$_3$ [30] and they have obtained the transfer integral t_a=0.080 eV, t_c=0.046 eV from the Drude's fit of their data. This value t_a/t_c~1.7 , where transfer integral is proportional to the overlap integral, is very different with the overlap integral used for the band calculation which is S$_a$/S$_c$~0.66. Therefore, Tamura *et al.* have recalculated the energy band from the optical measurements data which is shown in Fig. 2-10 [30].

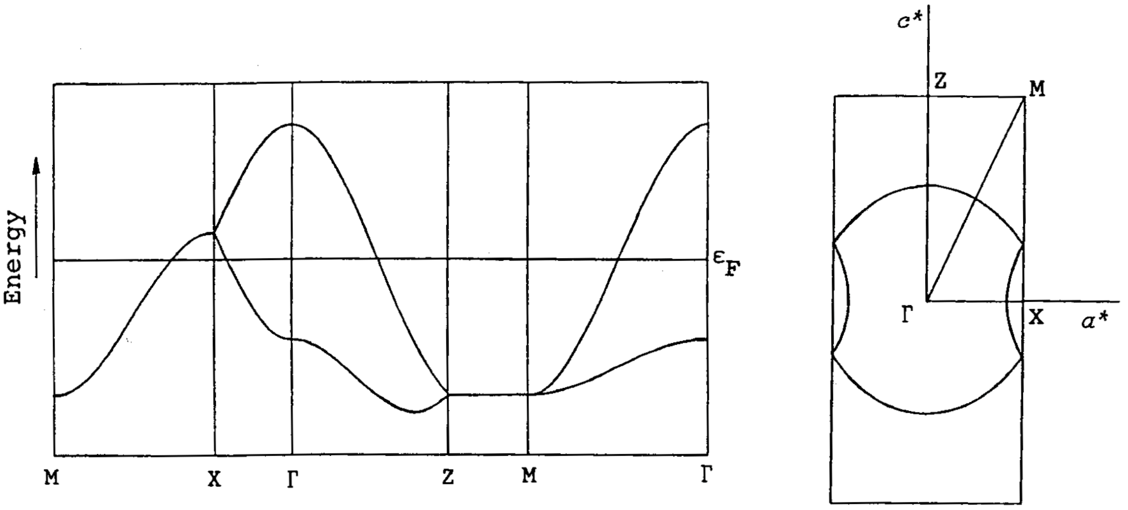

Fig. 2-9 The band calculation of θ-(BEDT-TTF)$_2$I$_3$ by considering the orthorhombic lattice. [25] The left shows the energy dispersion and the right shows the Fermi surface.

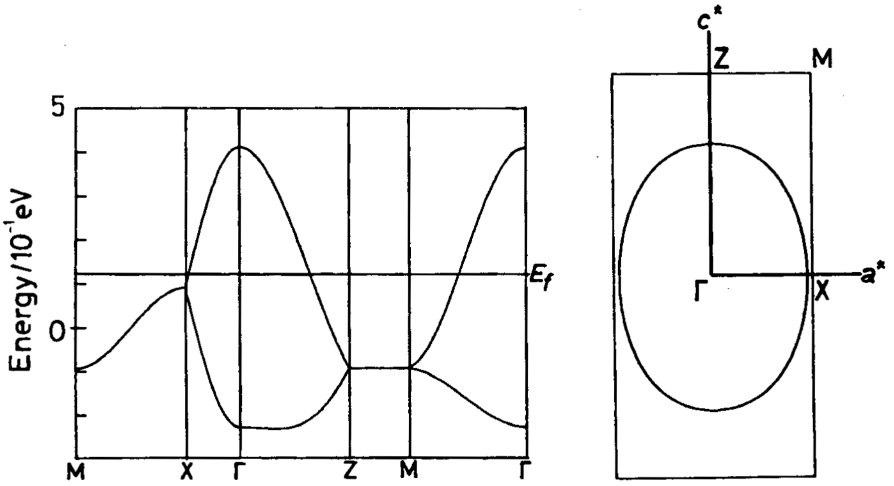

Fig. 2-10 Recalculated energy band of θ-(BEDT-TTF)$_2$I$_3$ from the optical measurements data. [30] The left shows the energy dispersion and the right shows the Fermi surface.

Unlike the former FS, which shows the ideal 2D shape, the recalculated FS shows a very anisotropic one. However, this calculation have been also considered for the orthorhombic lattice. Thus, if we consider the monoclinic lattice where $a_m=2c_o$, the zone boundary will be in the middle of ΓZ which suggests that there will be a closed pocket between ΓZ (a_m-axis) and a magnetic breakdown orbit. This discrepancy of the FS has been a puzzle and it was needless to say that quantum oscillations measurements were needed to clarify the shape of the FS.

The dHvA measurements have been performed by Tokumoto *et al.* and Tamura *et al.,* and their observation of dHvA oscillation when the field is applied perpendicular to the *ab*-plane (i.e. conducting plane) is presented in Fig. 2-11 [31-34]. We can see, at the left side of Fig. 2-11, very beautiful oscillation of the magnetization (i.e. dHvA oscillation) and very clear saw-tooth-shaped dHvA oscillation has also been observed, when the magnetization is plotted as a function of the inverse field, which suggests that the system is highly two dimensional. The Fourier transform spectrum of the dHvA oscillation shows the fundamental frequency of 4290 T corresponding to 100 % of the Brillouin zone (up-right of Fig. 2-11). Lower frequency of 789 T corresponding to 20 % of the Brillouin zone has also been observed. This favors the latter recalculated model where there are a pocket at zone boundary (20 % of the Brillouin zone) and a magnetic breakdown orbit (100 % of the Brillouin zone). Tamura *et al.* have observed also dHvA oscillation with nodes at 12, 15, 20 T at T=0.89 K as shown in the bottom-right of Fig. 2-11. This nodes is due to the two close frequency components at 4440 and 4494 T (100 % of the Brillouin zone), and the lower frequency of 814 T (20 % of the Brillouin zone) is also observed. These results are consistent with the previous results of Tokumoto *et al.* The beat behavior may come from the minimum (4440 T) and maximum (4494 T) of the cross-sectional area of q2D FS, however, they have conclude that these beats are composed of the contributions from the twin domain [34]. The conclusive FS topology from dHvA studies is shown in Fig. 2-12. It was concluded that the lower frequency component around 800 T in dHvA oscillation corresponds to the α-orbits which is the closed orbit around the zone boundary (20 % of the Brillouin zone) and the fundamental frequency around 4400 T corresponds to the β-orbit which is the magnetic breakdown orbit (100 % of the Brillouin zone).

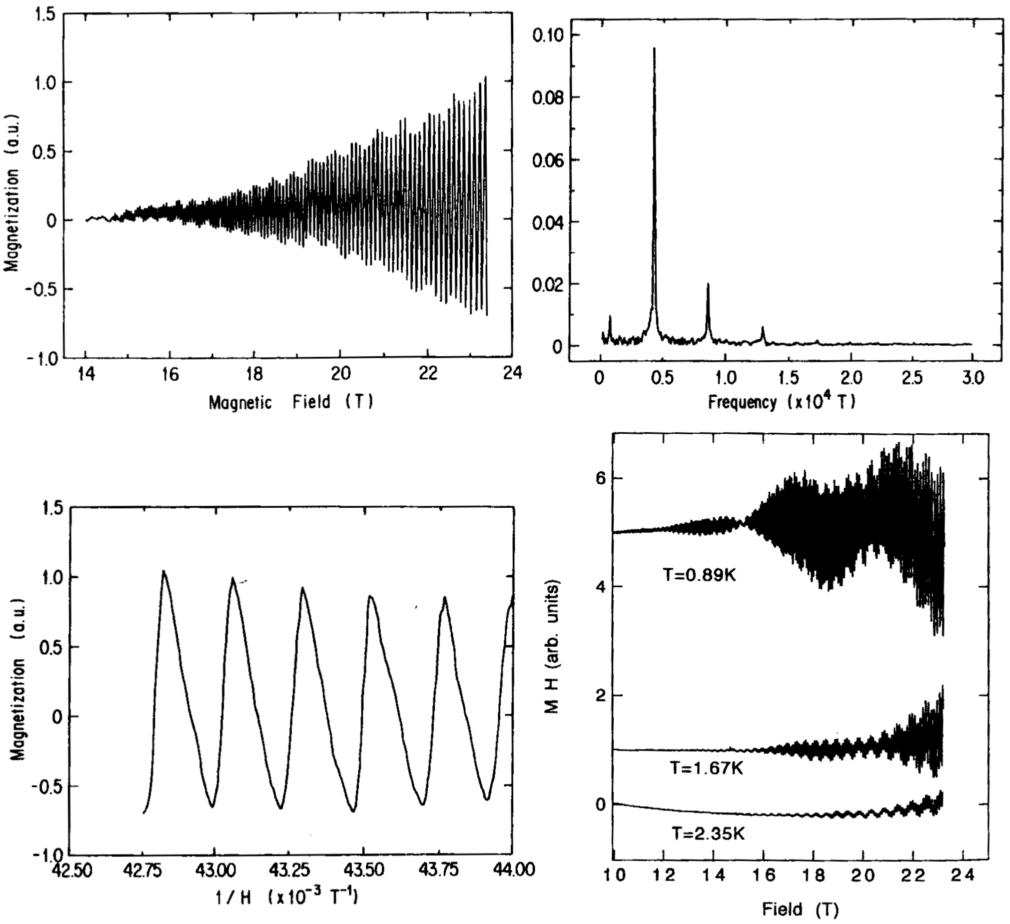

Fig. 2-11 Magnetization of θ-(BEDT-TTF)$_2$I$_3$ at 0.5 K. Beautiful dHvA oscillations are observed (at the up-left). The Fourier transform spectrum of the dHvA oscillation (at the up-right). Magnetization of θ-(BEDT-TTF)$_2$I$_3$ as a function of the inverse field (at the bottom-left). Another magnetization of θ-(BEDT-TTF)$_2$I$_3$ which shows distinct beat. (at the bottom-right). [31-34]

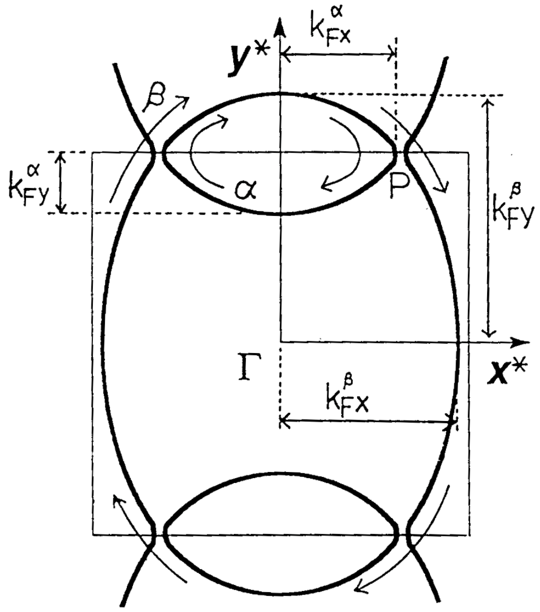

Fig. 2-12 The Fermi surface topology concluded from dHvA studies. [34]
x* and y * corresponds to *b* and *a*-axis, respectively.

Moreover, the effective mass for each orbit have been obtained by fitting the Lifshitz-Kosevich formula to the temperature dependence of the Fourier spectrum's amplitude as shown in Fig. 2-13 and the obtained effective masses are 2.0m_e and 3.6m_e for α and β-orbits, respectively.

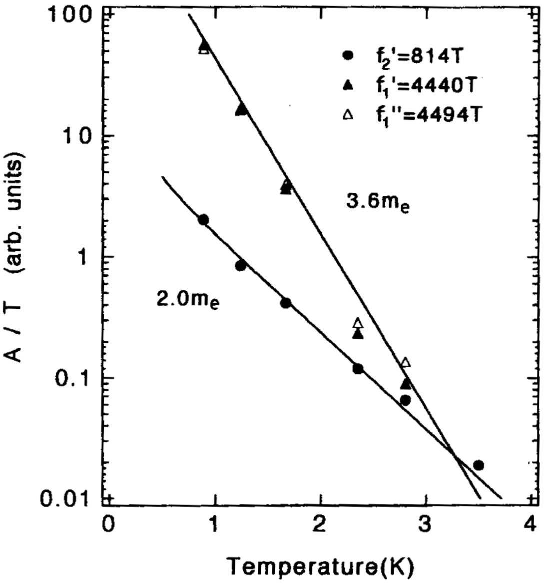

Fig. 2-13 The mass-plot, the plot of A/T versus T, where A is the amplitude of the Fourier component at each frequency. [34]

It is very important to mention about the magnetoresistance of θ-(BEDT-TTF)$_2$I$_3$, because ADMRO was observed for the first time in θ-(BEDT-TTF)$_2$I$_3$. Fig. 2-14 shows the first observation of ADMRO by Kajita *et al.* and we can see that the oscillation is not depending on the magnetic field strength but on the field direction [35].

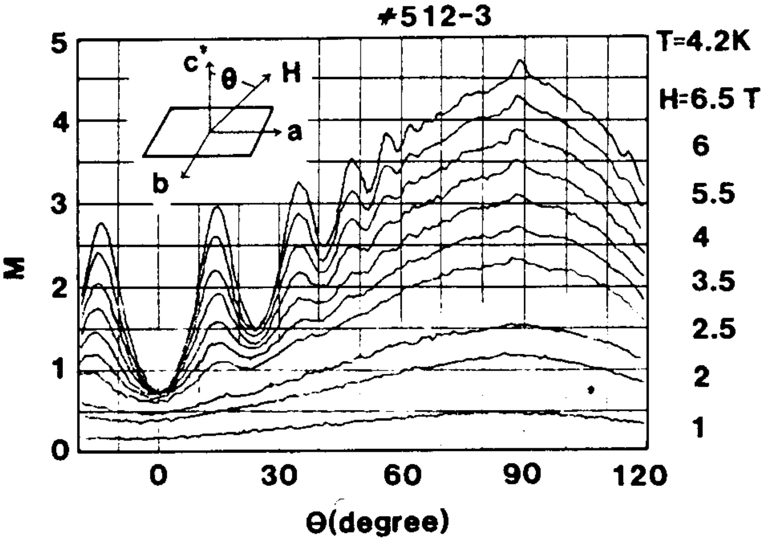

Fig. 2-14 Magnetoresistance plotted against the magnetic field direction. Magnetic field is rotated in the *ac**-plane. *ab*-plane is the conducting plane. [35]

We leave the explanation of the origin of this oscillation for the next section, however, we can obtain the Fermi wave number k_F from the periodicity of the peak in magnetoresistance by the formula

$$k_F = \frac{\pi}{d\cdot(\Delta\tan\theta)}, \qquad (2.21)$$

where d is the interlayer distance of adjacent conducting plane. The periodicity of the peaks in Fig. 2-14, which is $\Delta\tan\theta=0.39$, corresponds to the Fermi wave number parallel to a-axis $k_{F,//a}$~0.48 Å^{-1}. This value is in a good agreement with the magnetic breakdown orbit (β-orbit) size deduced from Fig. 2-12 but no oscillation corresponding to the closed α-orbit was observed. However, Terashima *et al.* have reexamined the ADMRO of θ-(BEDT-TTF)$_2$I$_3$ where short-period and long-period oscillations were observed [36]. They have performed ADMRO measurements at 1.7 K in the *ac**-and *bc**-plane and they have observed short-period and long-period oscillations for each plane. The obtained Fermi wave number parallel to *a*- and *b*-axes were $k_{F,//a}$~0.12 Å^{-1}, $k_{F,//b}$~0.20 Å^{-1} for the short-period and $k_{F,//a}$~0.44 Å^{-1}, $k_{F,//a}$~0.27 Å^{-1} for the long-period, respectively, and these values support the FS deduced from dHvA measurements.

Magnetoresistivity measurements in the higher field have also been performed and SdH oscillations were clearly observed [29,34]. We show SdH oscillations in the high magnetic field range in Fig. 2-15 and the inset shows its corresponding Fourier spectrum [29]. The magnetic field is applied perpendicular to the *ab*-plane.

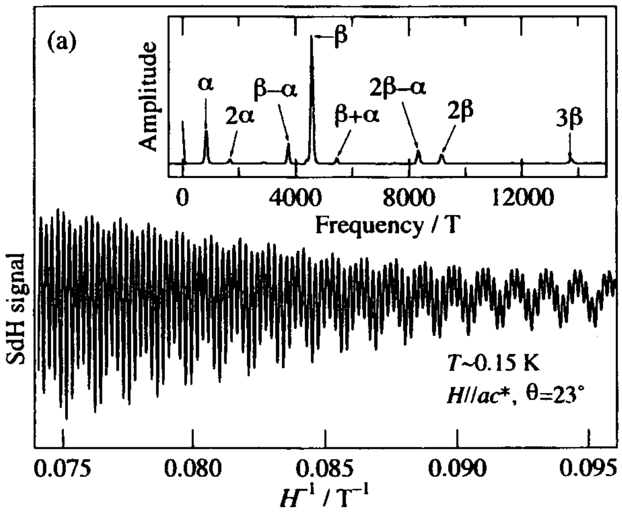

Fig. 2-15 SdH oscillations of θ-(BEDT-TTF)$_2$I$_3$ in the high magnetic field range. The inset shows its corresponding Fourier spectrum. [29]

The Fourier spectrum shows two fundamental frequencies noted by the symbol α and β and their combination frequencies. The frequencies are 779 T and 4243 T for α and β, respectively, where the corresponding cross-sectional areas are 19% and 102% of the Brillouin zone, respectively. Therefore, α and β oscillations can be attributed to the closed orbit around the zone boundary and the magnetic breakdown orbit, respectively. Furthermore, these frequencies show 1/cosθ dependence which suggests that the FS is cylindrical (θ is the angle between the magnetic field and the *c**-axis). The obtained effective masses for α and β-orbits correspond to $1.8m_e$ and $3.5m_e$, respectively. These results are consistent with the dHvA results. However, some novel oscillations were observed below 3 T (Fig. 2-16).

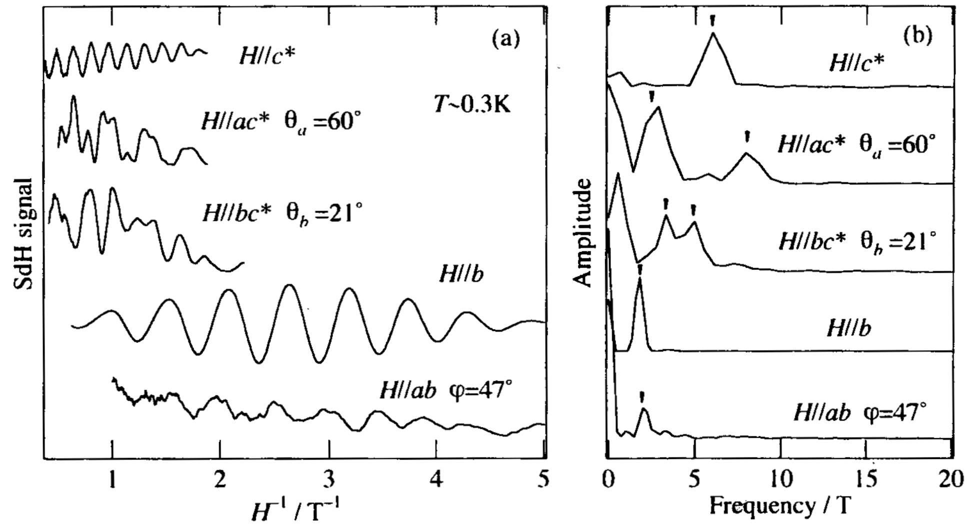

Fig. 2-16 SdH oscillations in a low magnetic field range (left). Its corresponding Fourier spectra (right). [29]

These novel oscillations are observed even for the magnetic field parallel to the conducting plane which suggest the FS are three dimensional [29]. The three dimensional FSs have the cross-sectional areas of only 0.1% of the Brillouin zone and the effective mass is estimated as $0.05m_e$ and $0.014m_e$. However, the origin of these new FSs is unknown.

In summary, the FS of θ-(BEDT-TTF)$_2$I$_3$ is concluded to be as Fig. 2-12 after many studies. The FS consists of a closed orbit at the zone boundary (α-orbit) and a magnetic breakdown orbit (β-orbit). The obtained effective masses for α and β orbits are $2.0m_e$ and $3.6m_e$ from dHvA measurements and $1.8m_e$ and $3.5m_e$ from SdH measurements, respectively.

-(BEDT-TTF)$_2$Br(DIA), (BEDT-TTF)$_3$Br(pBIB), (BEDT-TTF)$_3$Cl(DFBIB)-

Recently, Yamamoto *et al.* have succeeded to fabricate the supramolecular assemblies with halide anions (Cl^- or Br^-) and neutral molecules in BEDT-TTF salts [37-39]. (BEDT-TTF)$_2$Br(DIA), (BEDT-TTF)$_3$Br(pBIB) and (BEDT-TTF)$_3$Cl(DFBIB) are one of these novel organic conductors which are containing supramolecular assemblies where neutral molecules are DIA (diiodoacetylene), pBIB (p-bis(iodoethynyl)benzene) and DFBIB (1,4-difluoro-2,5-bis(iodoethynyl)benzene), respectively (Fig. 2-17).

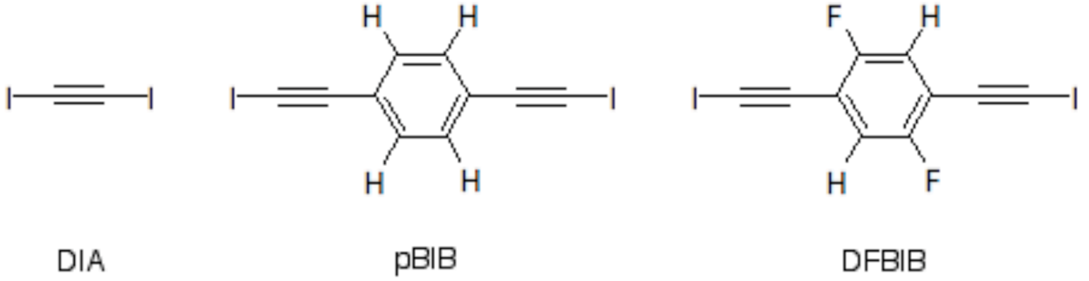

Fig. 2-17 Schematic drawings of supramolecular assemblies, DIA, pBIB and DFBIB.

One of the interesting features of the structure is that the supramolecular assemblies, which consist of neutral molecules and halide anions, form one dimensional chains and the donor molecules (i.e. BEDT-TTF) fit into the channels formed by these chains. And it may suggest the possibility of "fractional band-filling control" by changing 1D supramolecular assemblies with a different period. As shown in Fig. 2-17, the molecular length of pBIB and DFBIB are longer than DIA. Therefore, the donor/anion ratio is 2:1 for (BEDT-TTF)$_2$Br(DIA) and 3:1 for (BEDT-TTF)$_3$Br(pBIB) and (BEDT-TTF)$_3$Cl(DFBIB) as shown in the crystal structure of Fig. 2-18.

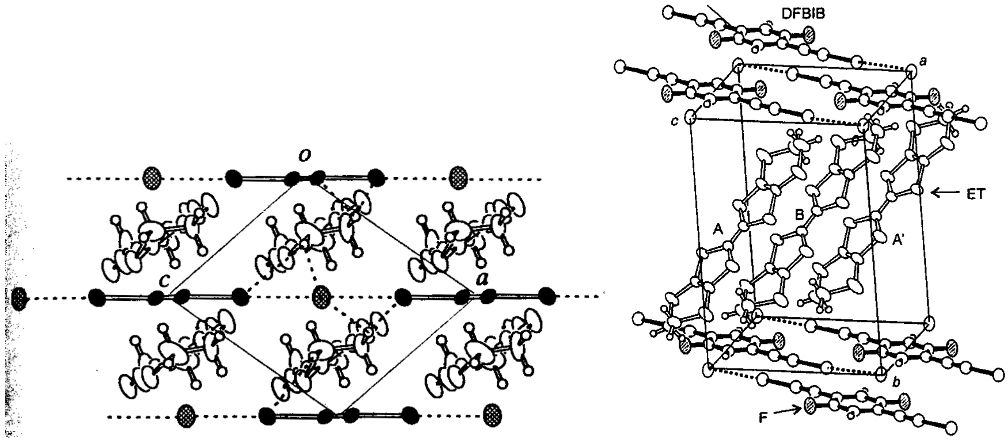

Fig. 2-18 Crystal structure of (BEDT-TTF)$_2$Br(DIA) and (BEDT-TTF)$_3$Cl(DFBIB). [38,39]

The band structure for each salt is very simple and the FS is estimated to have a simple closed orbit from the band calculation. The FS of (BEDT-TTF)$_2$Br(DIA) is shown in Fig. 2-19(a), and it has a very anisotropic (elliptic) FS extended to the $k_{a*}+k_{c*}$ direction. On the other hand, the FSs of (BEDT-TTF)$_3$Br(pBIB) and (BEDT-TTF)$_3$Cl(DFBIB) are also anisotropic (Fig. 2-19(b)), but less anisotropic than the (BEDT-TTF)$_2$Br(DIA) salt's FS. The FS's anisotropy of (BEDT-TTF)$_3$Br(pBIB) and (BEDT-TTF)$_3$Cl(DFBIB) differs a little bit and this is due to the anisotropic chemical pressure of its supramolecular assemblies. The ratio of the long axis to the short axis of the ellipse is 1.22 for (BEDT-TTF)$_3$Br(pBIB) and 1.39 for (BEDT-TTF)$_3$Cl(DFBIB) [39].

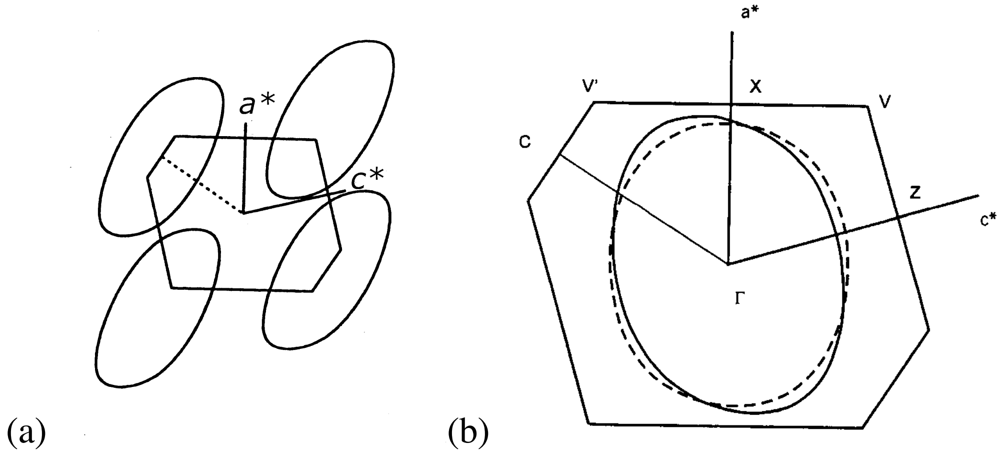

Fig. 2-19 (a) Fermi surface of (BEDT-TTF)$_2$Br(DIA). [38] (b)Fermi surface of (BEDT-TTF)$_3$Br(pBIB) (broken line), (BEDT-TTF)$_3$Cl(DFBIB) (solid line). [39]

(BEDT-TTF)$_2$Br(DIA) is metallic down to 0.3 K and RRR is fairly large (about 1500). Magnetoresistivity measurements of (BEDT-TTF)$_2$Br(DIA) have been done by Uji *et al.* [40,41] and Fig. 2-20 shows the angular dependence of the magnetoresistance at 13.5 T for azimuthal angle ϕ=-30°. ADMRO is observed in a wide angle region and the polar plot of k_F is shown in the inset of Fig. 2-20 where it shows a 2D FS with an elliptic cross-sectional area. The area is estimated to be 47% of the first Brillouin zone which is consistent with the band calculation [40].

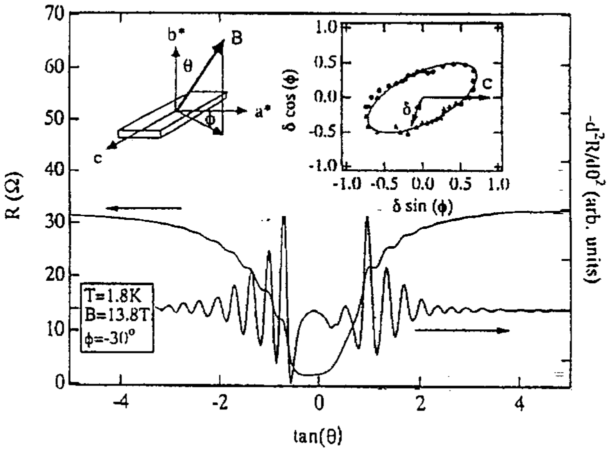

Fig. 2-20 Magnetoresistance of (BEDT-TTF)$_2$Br(DIA) along *b**-axis and the second derivative curve as a function of θ. The inset shows polar plot of the period of ADMRO. [40]

Fig. 2-21 shows the magnetoresistance measurement of (BEDT-TTF)$_2$Br(DIA) where the magnetic field was applied perpendicular to the conducting plane (*B*//*b**) up to 14 T. SdH oscillations were observed in the high and low field region [40,41].

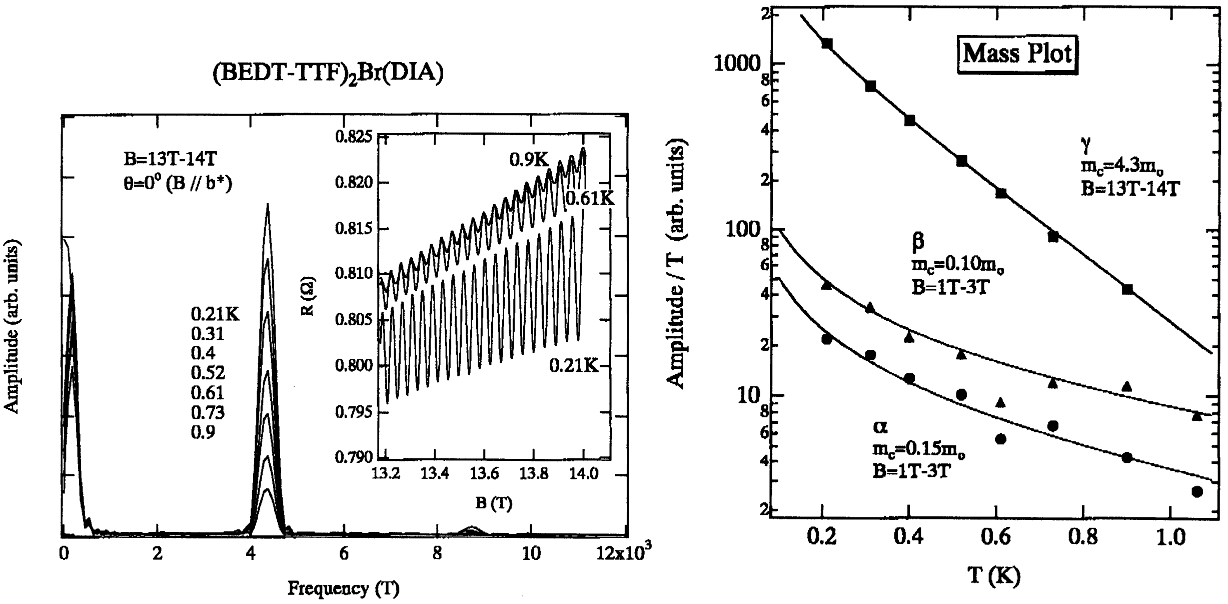

Fig. 2-21 The Fourier spectrum of the SdH oscillations (left) and the mass plot (right). [41]

In the high field region, only one SdH oscillation with the frequency 4300 T (γ-orbit) is observed which corresponds to 51% of the first Brillouin zone. This is consistent with the ADMRO result. In the low field region, there exist two distinct SdH oscillations with the frequencies of 12.5 T (β-orbit) and 9 T (α-orbit), whose cross-sectional areas are 0.15% and 0.11% of the Brillouin zone, respectively. All the frequencies follow the 1/cosθ dependence which suggest that the observed FSs have the cylindrical shape. However, the origin of the low frequency oscillations are not so clear. The effective masses for each orbit are obtained from the mass plot (Fig. 2-21) and are $0.15m_e$, $0.10m_e$ and $4.3m_e$ for α, β and γ-orbits, respectively.

$(BEDT\text{-}TTF)_3Br(pBIB)$ and $(BEDT\text{-}TTF)_3Cl(DFBIB)$ are the first metallic BEDT-TTF salts where the formal charge of a donor is +1/3. Both salts exhibit metallic behavior down to 1.6 K and RRR is fairly large, however, despite of having almost the same crystal structure, the resistivity of Cl(DFBIB) salt is higher than Br(pBIB) salt as shown in Fig. 2-22 [39]. ADMRO is observed for both salts and the area of FS is estimated to be 52.5% and 48.3% of the first Brillouin zone for Br(pBIB) salt and Cl(DFBIB) salt, respectively, and the ratio of the long axis to the short axis of the ellipse is 1.06 for $(BEDT\text{-}TTF)_3Br(pBIB)$ and 1.21 for $(BEDT\text{-}TTF)_3Cl(DFBIB)$ which is slightly smaller than the band calculation [42]. SdH oscillations are also observed for both salts, and two oscillations, minimum and maximum cross-sectional area of the q2D FS, with the frequencies 2296.7 T (50.9% of the Brillouin zone) and 2328.1 T (51.6% of the Brillouin zone) are observed for Br(pBIB) salt, and 2262.7 T (49.8% of the Brillouin zone) and 2318.8 T (51.1% of the Brillouin zone) are observed for Cl(DFBIB) salt [42]. The effective masses of Br(pBIB) and Cl(DFBIB) salts are $2.0m_e$ and $2.1m_e$, respectively.

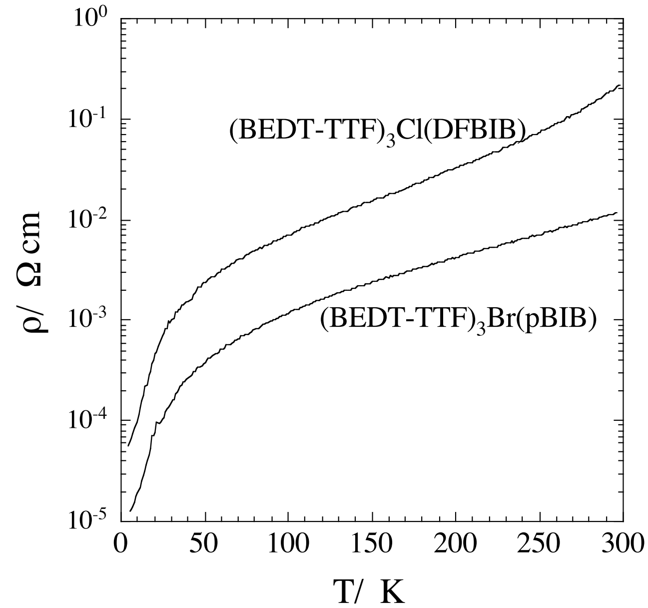

Fig. 2-22 Resistivity of $(BEDT\text{-}TTF)_3Br(pBIB)$ and $(BEDT\text{-}TTF)_3Cl(DFBIB)$. Data are taken from Ref. [39].

-(DMET)$_2$I$_3$-

(DMET)$_2$I$_3$ is a q1D organic conductor which shows metallic behavior below 300 K and undergoes a superconducting transition at 0.47 K at ambient pressure [43]. DMET molecules, where DMET stands for dimethyl(ethylenedithio)diselenadithia-fulvalene, is a non-centrosymmetric molecule which is formed by conjugating half of a TMTSF and half of a BEDT-TTF molecule (*see* Fig. 2-1). Besides, (DMET)$_2$I$_3$ is a conducting salt whose crystal structure is characterized by a DMET molecules stack along the *b*-axis (Fig. 2-23) and the band structure is considered to have a pair of FS spread along the $k_a k_{c*}$-plane [44].

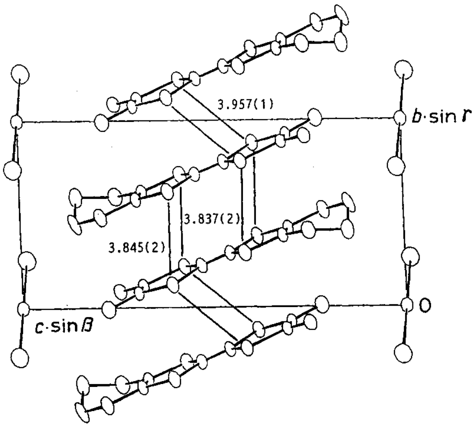

Fig. 2-23 Crystal structure of (DMET)$_2$I$_3$ viewed along the *a*-axis. [45]

The conducting axis is the *b*-axis and the conductivity ratio is $\sigma_b:\sigma_a:\sigma_{c*}$=6000:600:1 at the room temperature [45]. The corresponding ratio for other q1D organic conductor, (TMTSF)$_2$PF$_6$, is 30000:100:1 which suggests that (DMET)$_2$I$_3$ is less anisotropic than TMTSF salts. The magnetoresistance of (DMET)$_2$I$_3$ is shown in Fig. 2-24(a) where the magnetic field is applied perpendicular to the conducting plane (i.e. *B*//c*) and the kink behavior is observed above 10 T (see inset of Fig. 2-24(a)). On the analogy of the results for the TMTSF salts, these kinks can be assigned to the field induced spin density wave (FISDW) transitions. The phase diagram for *B*//c* is shown in Fig. 2-24(b) and superconducting phase transition is observed around 0.5 K as well as FISDW transitions above 10 T in the low temperature region. The phase boundary of (TMTSF)$_2$AsF$_6$ at 9 kbar is shown by a dotted line for comparison and the FISDW phase region seems to be very limited for (DMET)$_2$I$_3$. However, the quantized Hall resistance, which should be associated with FISDW transitions, was not obtained clearly down to 50 mK [46].

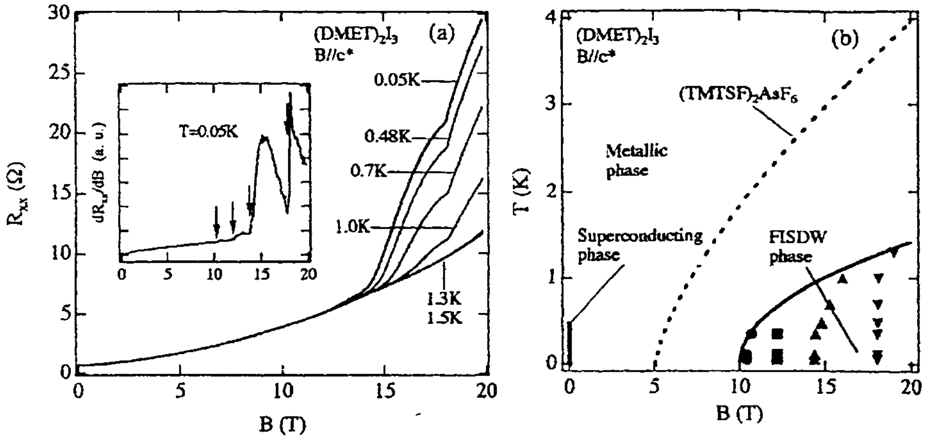

Fig. 2-24 (a) Magnetoresistance of $(DMET)_2I_3$ for *B*//*c** at various temperature. The inset shows the derivative curve and the arrows indicate the kink positions. (b) Temperature-field phase diagram for *B*//*c**. [46]

Angular dependence of the magnetoresistance measurements have been performed by Uji *et al.* for the *ac** and *bc**-plane [46,47], and by Yoshino *et al.* for the *ab*-plane [45,48]. Fig. 2-25(left) shows the interlayer resistance as a function of magnetic field θ for the field in the *ac**-plane. The angle θ is the angle between *c**-axis and the magnetic field. The periodic dip structure is visible only for q/p=-1, 0 and 1 and can be attributed to the Lebed resonance. Lebed resonance condition is given by $\tan\theta = pa'/qc^* - \cot\alpha^*$ where $a' = a\sin\gamma$, $c^* = c\sin\beta\sin\alpha^*$, and α^* is the angle between the *a*' and *c**-axes. Using the lattice parameters *a*=7.769 Å, *b*=6.710 Å, *c*=15.797 Å, α=98.15°, β=90.06°, γ=78.14° [44], the value $a'/c^*=0.42$, $\cot\alpha^*=0.15$ is obtained which seem to be consistent with the experimental results, $a'/c^*=0.44$, $\cot\alpha^*=0.19$. Fig. 2-25(right) shows the interlayer resistance and the second derivative curve as a function of θ for the field in the *bc**-plane. For the field in the *bc**-plane, characteristic structure appears only for the field around *b*-axis. Danner-Chaikin oscillations predict sharp structure for the field around the conducting axis and the peak structure is clearly seen only in the range up to 6° from the conducting axis for $(TMTSF)_2ClO_4$ [49]. However, the peak structures in Fig. 2-25(right) are seen up to 25° which seem very different from those for $(TMTSF)_2ClO_4$. If the peak structure can be attributed to the Danner-Chaikin oscillations, the critical angle θ_c can be taken to 25° from the *b*-axis. Since, the critical angle is given by $\tan\theta_c \sim t_a c/2t_b b$ [49]. The transfer integral ratio $t_a/t_b \sim 0.5$ is obtained and this value is five time larger than that for $(TMTSF)_2ClO_4$ which suggests that the electronic state for $(DMET)_2I_3$ is more 2D than that for $(TMTSF)_2ClO_4$.

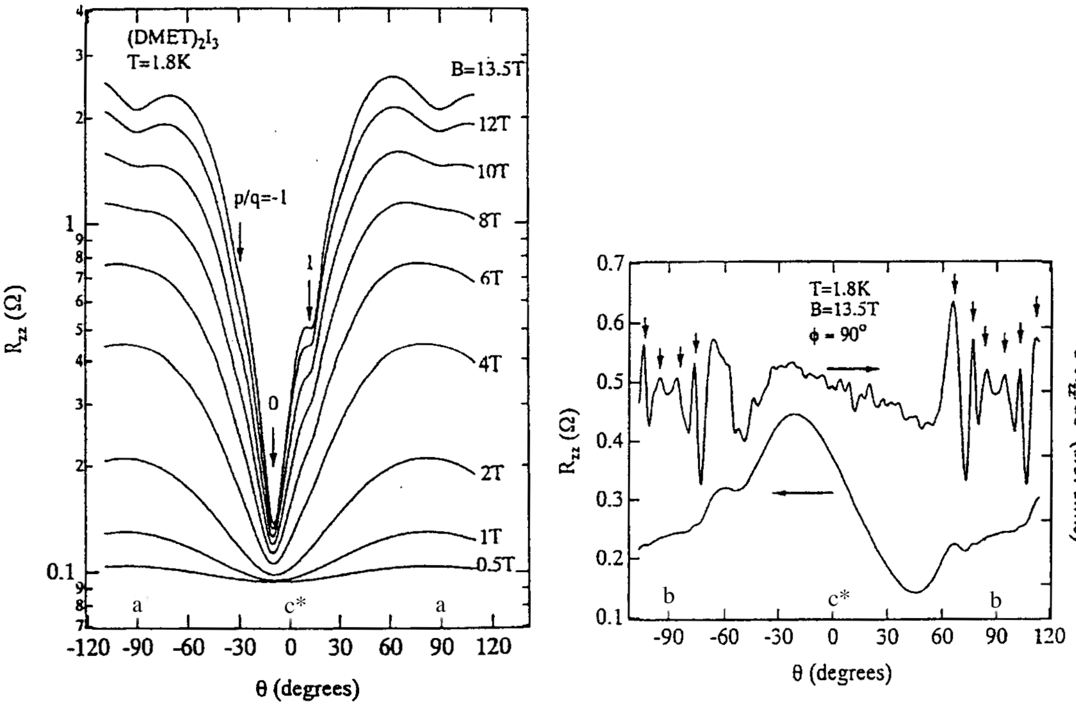

Fig. 2-25 (left) Resistance as a function of θ at 1.8 K for the magnetic field in the *ac**-plane. The arrows indicate the dips of Lebed resonance. [46,47]
(right) Resistance and the second derivative curve as a function of θ for the field in the *bc**-plane. [46,47]

The magnetoresistivity for the *ab*-plane is shown in Fig. 2-26. Peak structures around *b*-axis are observed and these peaks become sharper as the magnetic field increases. This phenomenon observed in (DMET)$_2$I$_3$ is known as the first observation of the third angular effect in ADMRO [45,48]. The third angular effect originates from the appearance or vanishing of closed orbits on the sheet-like FS when the magnetic field is rotated in the most conducting plane. The closed orbits enhance the magnetoresistance because the carrier velocity along the k_z-axis is averaged to zero. Therefore, a peak in magnetoresistance should be observed around the *b*-axis. However, three peaks are observed for (DMET)$_2$I$_3$ as seen in Fig. 2-26. Consequently, all the ADMRO measurements support the scenario that (DMET)$_2$I$_3$ have q1D FS.

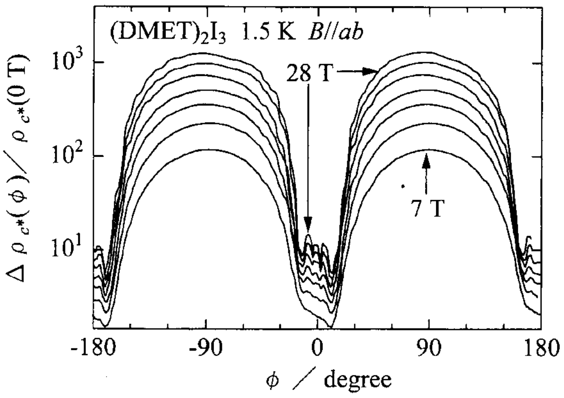

Fig. 2-26 The resistivity as a function ϕ at 1.5 K for the magnetic field in the *ab*-plane. [48] The third angular effect is clearly observed at around ϕ=0° (i.e. *B*//*b*).

3. Band structure-measuring techniques using high magnetic fields

3.1. Quantum oscillation measurements

We have seen in section 2.3 that the energy of electron under magnetic field is degenerated into Landau levels. We will see in this section that this Landau levels can be used for the band structure measuring techniques.

The energy between Landau levels can be written from eq.(2.20) as

$$\Delta E = \hbar\omega_c = \frac{\hbar eB}{m^*}. \qquad (3.1)$$

which means that the energy between Landau levels will be larger as magnetic field B increases. We show in Fig. 3-1, the schematic diagram of Landau levels as the magnetic field B is increased. As seen in Fig. 3-1, the Landau level (n+1) is below the Fermi energy E_F at first, and as the field B increases, the Landau level will reach the Fermi level. However, if we continue to increase the field, Landau level (n+1) will pass through the Fermi energy and there will be a reconfiguration of electrons from n+1 state to the n state. This suggests that the total free energy U will reduce, but will increase again as the magnetic field increases. Therefore, the total free energy will oscillate as a function of magnetic field B. The oscillation of total free energy U will lead to the oscillation of, for example, magnetism or specific heat.

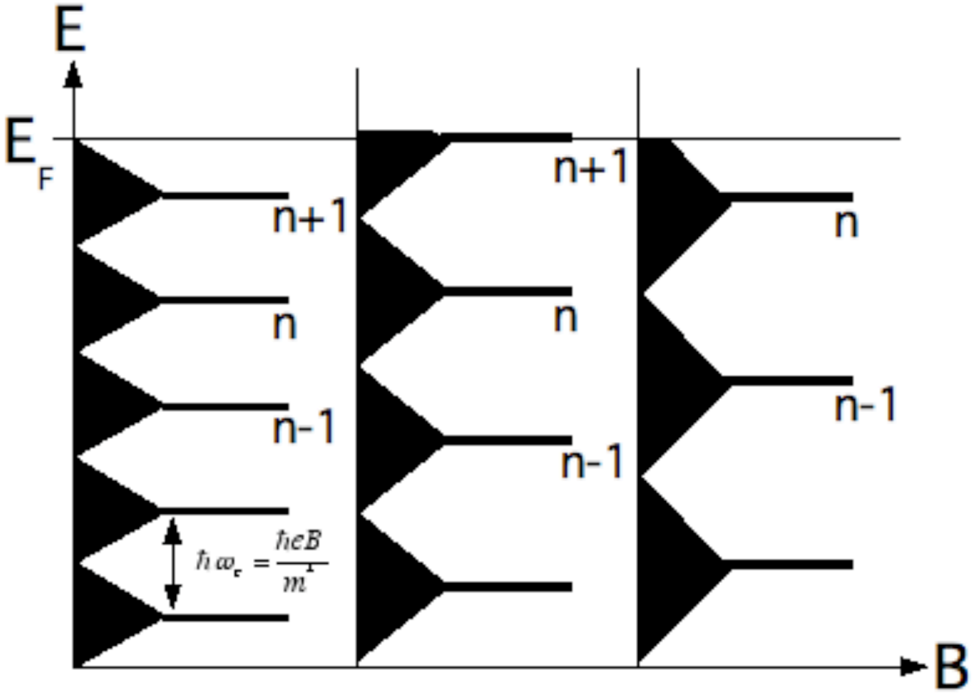

Fig. 3-1 Schematic figure of the Landau levels as magnetic field B increases.

However, this is only true at T=0 where E_F~$\mu(T$=0) and chemical potential μ is the important energy as far as the electrons are concerned. Thus, it is when the sharp peaks in electronic density of states moves through the chemical potential μ, that there will be a modulation of the density states. This modulation of the density states will exhibit oscillations of the magnetization (dHvA oscillation), magnetoresistance, (SdH oscillation), thermal conductivity and so on. Anyway, let us go back to the previous picture, if there is n Landau levels below the Fermi energy E_F, n can be written as

$$n = \frac{E_F}{\hbar\omega_c} = \frac{\hbar}{2\pi e} A_F \left(\frac{1}{B_n}\right), \qquad (3.2)$$

where $E_F = \frac{\hbar^2 k_F^2}{2m}, A_F = \pi k_F^2$. The oscillation will occur when the number of Landau levels n changes. Therefore, the frequency of oscillations can be written as follows,

$$f = \frac{\Delta n}{\Delta(1/B)} = \frac{(n+1)-n}{\frac{1}{B_{n+1}} - \frac{1}{B_n}} = \frac{\hbar}{2\pi e} A_F . \qquad (3.3)$$

This suggests that, consequently, the oscillations will occur with the frequency f and we can obtain the cross-sectional area of the FS, A_F, from the frequency of the oscillations. The dHvA effect has been well studied theoretically and the explicit form of the oscillatory part M including the phase smearing effects due to the finite temperature, electron scattering, and electron spin is given as

$$M \propto \left(\frac{B}{\left|\partial^2 A_F / \partial\kappa^2\right|}\right)^{1/2} \sum_{r=1}^{\infty} \frac{(-1)^r}{r^{3/2}} R_D R_T R_S \sin\left[2\pi r\left(\frac{f}{B} - \gamma\right) \pm \frac{\pi}{4}\right]. \qquad (3.4)$$

This formula is known as the Lifshitz-Kosevich (L-K) formula. The curvature factor $\left|\partial^2 A_F / \partial\kappa^2\right|^{-1/2}$ describes the curvature of the FS, i.e., the change of A_F parallel to B. The reduction factors R_D and R_T describe the superposition of oscillations with different phases due to the scattering of electrons and oscillations of slightly varying f due to the finite temperature T, respectively. R_S takes into account the Zeeman splitting of the Landau levels in the magnetic field. If we describe the reduction factors in more detail, R_T, R_D, and R_S is

$$R_T = \frac{\alpha r \mu T / B}{\sinh(\alpha r \mu T / B)}, \qquad (3.5)$$

$$R_D = \exp\left(-\alpha r \mu T_D / B\right), \qquad (3.6)$$

$$R_S = \cos\left(\frac{1}{2} r\pi g \mu_B\right), \qquad (3.7)$$

where $\alpha = 2\pi^2 k_B m_e / e\hbar = 14.69$ T/K and μ is the effective mass in relative unit of the free electron mass (i.e. $\mu = m^*/m_e$) and $T_D = \hbar / 2\pi k_B \tau$ is the so-called Dingle temperature. Therefore, the effective mass can be extracted by fitting eq.(3.5) to the temperature dependence of the oscillations' amplitude and Dingle temperature (i.e. scattering time) can be extracted from the field dependence of the oscillations' amplitude by using eq.(3.6). This suggests that the cross-sectional area of the FS, A_F, and effective mass, m^*, and Dingle temperature, T_D, can be obtained from the frequency f and amplitude of dHvA oscillations. And, in principle, the same equations can be used for SdH experiments. We note that the frequency f of quantum oscillations is determined solely by the FS extremal area and several different frequencies may be simultaneously present for a given orientation of B. Moreover, a measurement of the observed frequencies as a function of magnetic field orientation allows the FS shape to be mapped out.

In summary, we have briefly explained the quantum oscillations measurement techniques where information about the FS shape, effective mass and scattering time can be extracted. For readers who are more interested in this technique, we refer excellent book on the quantum oscillations [50].

3.2. Angle dependent magnetoresistance oscillation measurements

-q2D ADMRO-

In the course of investigating the electronic properties of organic conductors in magnetic field, new oscillatory phenomena, which are connected to the low dimensional FS topology, have been observed. Kajita *et al.* have observed magnetoresistance oscillations which are angle dependent for the first time in q2D organic conductor θ-(BEDT-TTF)$_2$I$_3$ and have shown that these oscillations have a tanθ dependence (see section 2.4 and Fig. 2-14) [35]. At almost the same time, Kartsovnik *et al.* have also observed similar phenomenon in q2D organic conductor β-(BEDT-TTF)$_2$IBr$_2$ [51]. These oscillations, called the angular dependent magnetoresistance oscillations (ADMRO), do not depend on the strength of the magnetic field, but depend only on the orientation of the magnetic field which suggest that it is not related to the SdH oscillations. The first theoretical explanation of this phenomenon is done by Yamaji and have explained it from a simple band structure [52]. Yamaji have considered a simple q2D band structure,

$$E(k) = \frac{\hbar^2}{2m}\left(k_x^2 + k_y^2\right) - 2t_c \cos(ck_z), \qquad (3.8)$$

where k_x and k_y are the conducting plane component of the crystal wave vector k, and c and k_z are the spacing between adjacent conducting planes and the component of the wave vector perpendicular to the plane, respectively. When the magnetic field B is inclined by the angle θ from the k_z direction to the k_x-direction, the trajectories of semiclassical closed orbits are given by the intersection of the FS and planes perpendicular to the field defined by the following equation,

$$k_x \sin\theta + k_z \cos\theta = p \equiv k_z^{(0)} \cos\theta, \qquad (3.9)$$

where $k_z^{(0)}$ denotes the point of intersection of the k_z-axis with the orbital plane (see Fig. 3-2). The area of the orbital plane S_k in the k-space can be obtained by employing the polar coordinates $k_{//}$ and ϕ in the $k_x k_y$-plane,

$$\begin{aligned} S_k &= \frac{1}{\cos\theta}\int_0^{\pi} d\phi \left\{k_F^2 + 4mt_c \cos\left[c\left(k_z^{(0)} - k_F \tan\theta \cos\phi\right)\right]\right\} \\ &= \frac{1}{\cos\theta}\left[S_0 + 4\pi m t_c \cos\left(ck_z^{(0)}\right) \cdot J_0\left(ck_F \tan\theta\right)\right], \qquad (3.10) \end{aligned}$$

where $S_0 = \pi k_F^2$, and J_0 is the Bessel function.

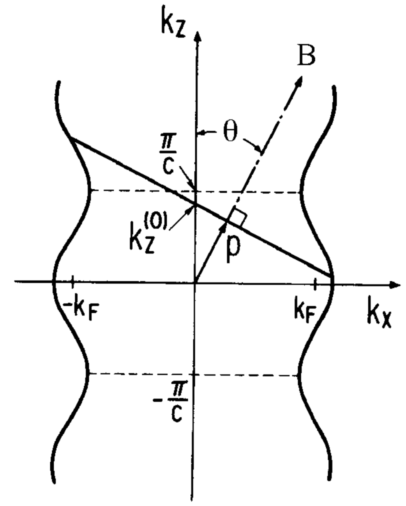

Fig. 3-2 q2D FS viewed along the k_y-axis. Vertical thick curves denote the intersection of the FS with the $k_x k_z$-plane. The oblique thick line perpendicular to the magnetic field is the projection of the electron orbit onto $k_x k_z$-plane.

The area S_k will become minimum when $J_0(ck_F \tan\theta) = 0$ and this minimum is not related with $k_z^{(0)}$ which suggest the electronic system becomes highly 2D at this minimum. Since $J_0(z) = (2/\pi z)^{1/2}\cos(z - \pi/4)$ for z>1, the minimum occurs when

$$\tan\theta = \frac{\pi}{ck_F}\left(n - \frac{1}{4}\right) \qquad (3.11)$$

with integer *n*. In other words, when the field is applied to an arbitrary direction, most electrons move along the spiral orbits parallel to the field as seen in Fig. 3-3(a). However, if the field is applied to the angle which satisfies eq.(3.11), all orbits are two dimensionally localized and average the electron velocity for all states in the *z* direction to zero (i.e. the resistivity is maximized) as seen in Fig. 3-3(b). This causes oscillation of interlayer conduction as the magnetic field is tilted (i.e. ADMRO).

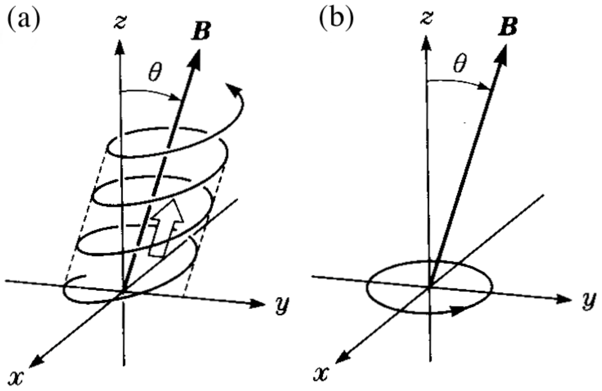

Fig. 3-3(a) The trajectories of electrons when the field is applied to an arbitrary orientation, (b) when the field orientation satisfies eq.(3.11). [2]

Moreover, Yagi *et al.* have carried out a semiclassical calculation of the conductivity tensor $\sigma_{\alpha\beta}$ according to the same model [53] and have showed that the phenomenon can be also explained semiclassically. From eq.(3.11), we can extract the Fermi wave vector component k_F of its rotating direction. This means that from the ADMRO measurements for different rotating planes, we can obtain the in-plane FS shape. And it is now widely used to map out cross-section of the FS.

-q1D ADMRO-

A different situation in ADMRO occurs for the q1D organic conductors. If the field is rotated in the *bc*-plane, that is, perpendicular to the highly conducting *a* direction, weak structures in the resistance appear at special angles, tanθ=*mb*/*nc*, where *m*,*n* are integers and *b*,*c* are the lattice parameters of the orthorhombic crystal structure. These dips of the interlayer resistivity are called the magic angles or the Lebed resonance. If now a magnetic field is applied in a general direction in the *bc*-plane the electron trajectory in the reduced first Brillouin zone fills the whole corrugated FS area as shown schematically in Fig. 3-4(a). The velocity components v_y and v_z take all possible values and thus averaged to zero (i.e. increase of the resistivity). However, for special orientation, $\tan\theta_c = mb/nc$, the electrons moves along the reciprocal lattice vector $K = mk_y + nk_z$. Hence, the trajectory in the first Brillouin zone consists of only finite sets of lines as seen in Fig. 3-4(b). Therefore, the average velocity becomes non zero in this case and consequently dips of resistance (i.e. minimum resistivity) are expected.

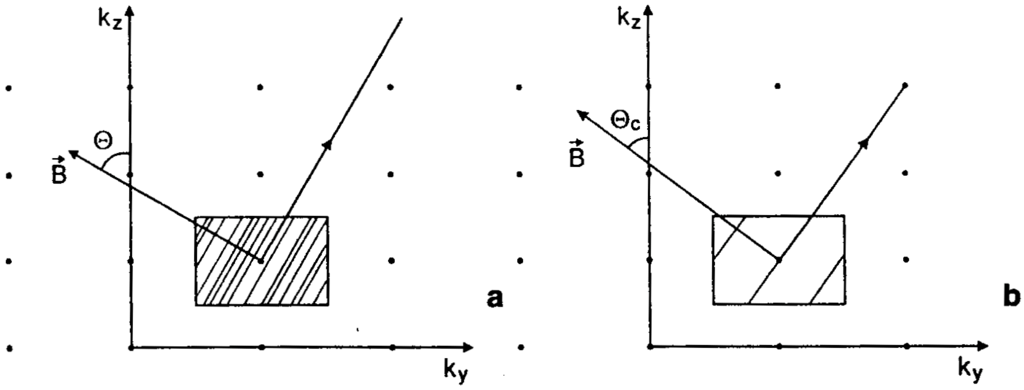

Fig. 3-4 Schematic view of an electron trajectory on the 1D FS sheet when the field *B* is applied (a) in an arbitrary direction in the *bc* plane and (b) in a commensurate direction (*m*/*n*=1/2).

An explanation for this magic angle has been given by Osada *et al.* [54]. They have considered the following band model around the Fermi level for q1D system:

$$E(k) = \hbar v_F\left(|k_x| - k_F\right) - \sum_{m,n} t_{mn}\cos(mbk_y + nck_z), \qquad (3.12)$$

where b and c are interchain distances along the y and z directions and t_{mn} represents the effective transfer integral associated with the lattice vector $R_{mn} = (0, mb, nc)$. Only t_{mn} with small m and n have finite values. From eqs.(2.8),(2.9) and (3.12), The electron velocity $v(k,t)$ is given by

$$v_x(k,t) = \mathrm{sgn}(k_x)v_F,$$

$$\begin{pmatrix} v_y(k,t) \\ v_z(k,t) \end{pmatrix} = \sum_{m,n} \frac{t_{mn}}{\hbar} \begin{pmatrix} mb \\ nc \end{pmatrix} \sin\left\{G_{mn}x(t) + mbk_y + nck_z\right\}. \qquad (3.13)$$

Here,

$$G_{mn} = eB(mb\cos\theta - nc\sin\theta)/\hbar, \qquad (3.14)$$

$x(t) = \mathrm{sgn}(k_x)v_F t$.

Semiclassically, the complex conductivity is calculated by the kinetic form of the Boltzmann equation assuming that scattering time τ is constant,

$$\sigma_{ij}(\omega) = \frac{2e^2}{V}\sum_k\left(-\frac{df(k)}{dE(k)}\right)v_i(k,0) \times \int_{-\infty}^{0} v_j(k,t)e^{[(1/\tau)-i\omega]t}dt. \qquad (3.15)$$

Hence, from eqs.(3.13) and (3.15), the real part of the complex conductivity elements at low temperatures are obtained as follows,

$$\sigma_{xx} = N(E_F)(ev_F)^2\frac{\tau}{1+(\omega\tau)^2},$$

$$\sigma_{xy} = \sigma_{yx} = \sigma_{xz} = \sigma_{zx} = 0$$

$$\begin{pmatrix}\sigma_{yy} & \sigma_{yz}\\ \sigma_{zy} & \sigma_{zz}\end{pmatrix} = N(E_F)\sum_{m,n}\left(\frac{et_{mn}}{\hbar}\right)^2\begin{pmatrix}m^2b^2 & mnbc\\ mnbc & n^2c^2\end{pmatrix}\times\frac{\tau}{1+\left\{(\omega - v_F G_{mn})\tau\right\}^2}, \qquad (3.16)$$

where $N(E_F) = 4/2\pi\hbar v_F bc$ is the density of states per unit volume at the Fermi level. Therefore, eq.(3.16) suggests that the dc interlayer conductivity (i.e. σ_{zz} with ω=0) will have a maximum in conductivity (i.e. Lebed resonance) when G_{mn}=0 or tanθ=*mb*/*nc* from eq.(3.14). The orthorhombic crystal lattice was considered in the above case, however, if the conductivity in the oblique crystal lattice system is considered [55], the lattice vector is now R_{mn}=(0, *mb*+*nd*, *nc*) and the energy band is

$$E(k) = \hbar v_F\left(|k_x| - k_F\right) - \sum_{m,n} t_{mn}\cos((mb+nd)k_y + nck_z). \qquad (3.17)$$

Then, the eqs.(3.14) and (3.16) can be rewritten as

$$\begin{pmatrix}\sigma_{yy} & \sigma_{yz}\\ \sigma_{zy} & \sigma_{zz}\end{pmatrix} = N(E_F)\frac{e^2\tau}{\hbar^2}\sum\begin{pmatrix}(mb+nd)^2 & (mb+nd)nc\\ (mb+nd)nc & (nc)^2\end{pmatrix}\frac{t_{mn}^2}{1+\left\{(\omega - v_F G_{mn})\tau\right\}^2}, \qquad (3.18)$$

$$G_{mn} = eB\left[(mb+nd)\cos\theta - nc\sin\theta\right]/\hbar. \qquad (3.19)$$

Maxima in the interlayer dc conductivity are observed whenever G_{mn}=0, i.e.,

$$\tan\theta = \frac{mb}{nc} + \frac{d}{c} = \frac{mb}{nc} - \cot\alpha, \qquad (3.20)$$

where α is the angle between *b** and *c**-axis. This eq.(3.20) gives a good agreement with the experimental results (Fig. 3-5) and Lebed resonance is now known as a characteristic behavior of the q1D electronic system [2,3,56].

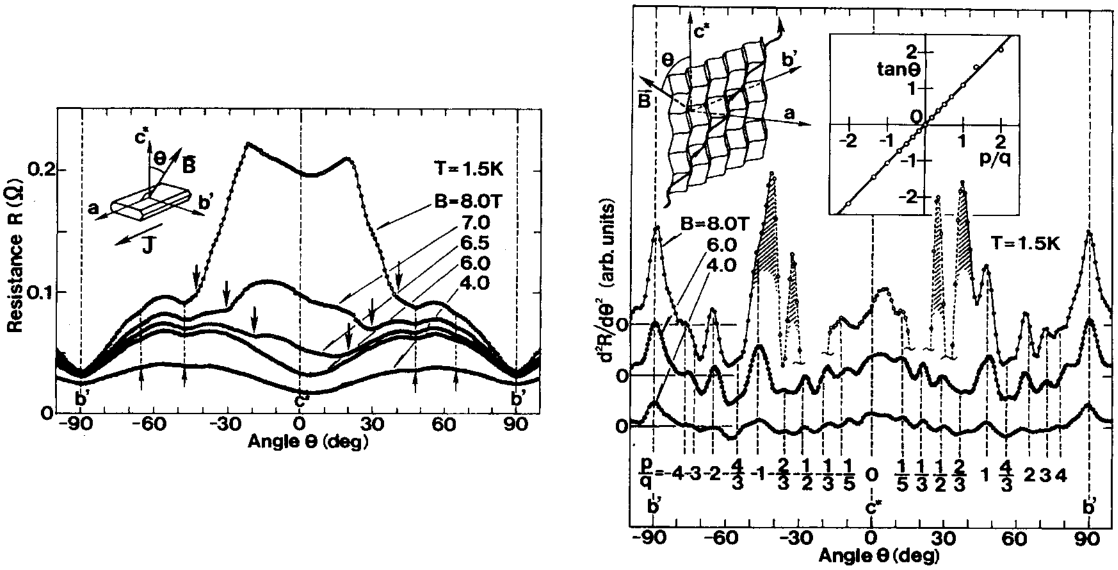

Fig. 3-5 (left) Magnetoresistance anisotropy of (TMTSF)$_2$ClO$_4$ at several field values in the bc^*-plane. (right) The second derivative of the magnetoresistance. The angles which satisfies tanθ=1.0 x p/q + 0.09 are shown. The inset shows the plot of the tangent of peak position vs the fraction p/q are shown. [56]

Another ADMRO effect was found in (TMTSF)$_2$ClO$_4$ when the field was tilted in the *ac*-plane [49], in contrast to the *bc*-plane discussed above. The experimental observations for the fields closed to the conducting *a*-axis is shown in Fig. 3-6 and clear peaks in the magnetoresistance are observed above a certain field [49]. This behavior is known as the second angular effect or Danner-Chaikin oscillations. The schematic figure of electron orbits on the q1D FS for different field orientations is also shown in Fig. 3-6. When $B//a$, there are a few orbits that close around the maxima and minima of k_x (orbit 1'), but most orbits are extended to infinity in k_z (orbit 1). As the field is tilted away from a, the orbits have large amplitude oscillation in k_z and are extended to infinity k_y. For an arbitrary angle, the average of v_z over the path needs not to be zero. However, if the oscillations in k_z just extend over an integer number of Brillouin zones (orbits 2 and 3) v_z averages to zero (i.e. maximum resistivity). For angle larger than the orbit 3, v_z can no longer average to zero. Therefore, the resistance decreases rapidly with increasing the angle as shown in Fig. 3-6.

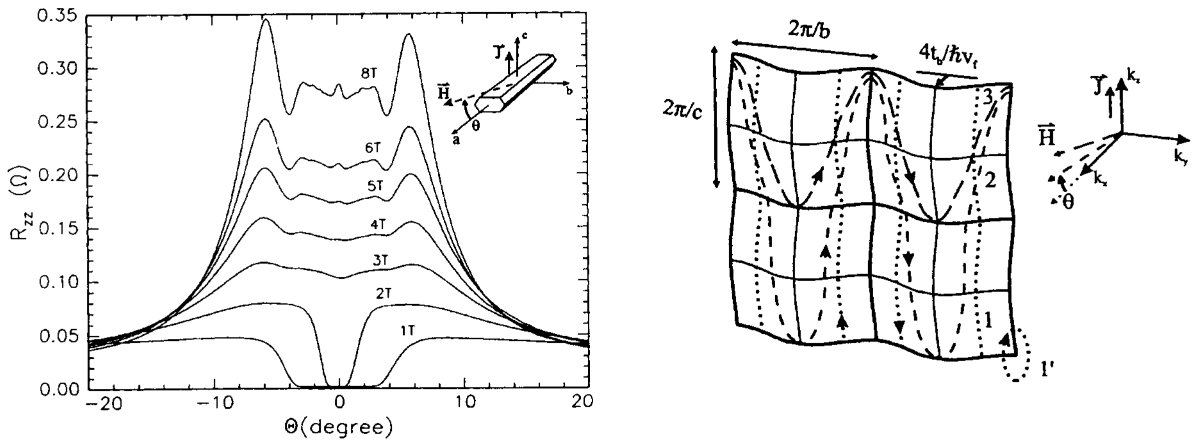

Fig. 3-6 Angular dependence of magnetoresistance for rotations in the *ac*-plane at different fields for $(TMTSF)_2ClO_4$ and schematic figure of electron orbits on the q1D FS for different field orientation. [49]

The angle where maxima in magnetoresistance occur are connected with the amplitude of the FS corrugation, that is $4t_b/\hbar v_F$, and the length of the Brillouin zone $2\pi/c$. With the semiclassic eqs.(2.8) and (2.9), and for $v_F B_z >> v_z B_x$ the average velocity in the z direction is given by [49]

$$\langle v_z \rangle \propto \int_0^{2\pi} \sin[\gamma \cos\Theta] d\Theta \text{, with}$$

$$\gamma = \frac{2t_b c}{\hbar v_F} \frac{B_x}{B_z}. \qquad (3.21)$$

The zeros of this integral are the same for the Bessel function $J_0(\gamma)$. Therefore, from the positions of the resistivity maxima, t_b can be extracted and this ADMRO effect becomes a new method which gives a quantitative information on the transfer integral in the second most conducting direction for q1D materials.

Moreover, when the field direction is closed to the most conducting axis, closed orbits appear on the FS and cause the third angular effect [57]. When closed orbits on the q1D FS appear, the carrier velocity along the k_z-axis is averaged to zero and a peak in magnetoresistance should be observed. The critical angle ϕ_c, where the closed orbits disappear, can be obtained from the FS topology and is given by

$$\tan\phi_c = \frac{2t_b b}{\hbar v_F}, \qquad (3.22)$$

where ϕ is the angle between the most conducting axis and the magnetic field rotated to the second most conducting axis. If a quarter of the band is occupied, eq.(3.22) becomes

$$\tan\phi_c = \sqrt{2}\frac{t_b b}{t_a a}, \qquad (3.23)$$

since $v_F = \sqrt{2} t_a a / \hbar$. Therefore, information about the transfer integral ratio t_b/t_a can be obtained from the angle range where third angular effect is observed.

In summary, we have shown that three angular effects can be observed in q1D ADMRO (Fig. 3-7). One is the Lebed resonance which is a series of resonance-like dip structures on the angular dependence pattern of magnetoresistance when the magnetic field is rotated in the plane perpendicular to the most conducting axis. The resonance angles satisfy the commensurability condition, i.e. eq.(3.20). The second angular effect, called Danner-Chaikin oscillations, is the oscillation of magnetoresistance when the magnetic field is rotated in the plane defined by the conducting axis and the axis normal to the conducting plane. The third angular effect occurs around the conducting axis when the field is rotated in the conducting plane.

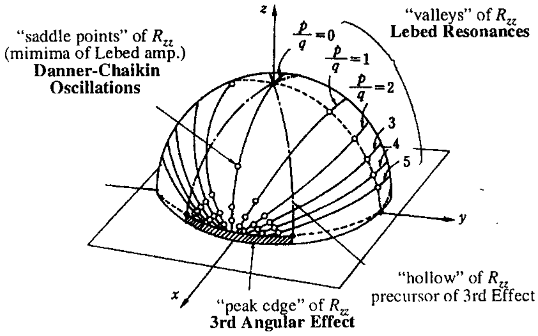

Fig. 3-7 Magnetoresistance angular effects in q1D conductors. [58]

3.3. Magnetooptical measurements

3.3.1 Cyclotron resonance

We have seen in section 2.3 and 3.1 that the energy of electron under magnetic field is degenerated into Landau levels and the energy between Landau levels is $\Delta E = \hbar\omega_c$. Hence, it is possible to make a direct measurement of ω_c using the millimeter-waves or far-infrared radiation (e.g. from 30 GHz to 300 GHz region) to excite transition between Landau levels. Such an experiment is known as cyclotron resonance (CR). The CR is usually recorded by measuring the sample transmission. Experiments are carried out either by fixing the magnetic field and varying the energy of the radiation, or by using a fixed frequency source and sweeping the magnetic field. When the frequency (i.e. energy) of the radiation matches with the energy between Landau levels, a resonant absorption of the transmission will occur. Thus, the resonance condition is

$$\omega = \omega_c = \frac{eB}{m^*}, \qquad (3.24)$$

where ω is the angular frequency of the radiation, and we can obtain the cyclotron effective mass m^* directly from eq.(3.24). However, the conditions for observing CR in metals and semiconductors are rather different, and the two cases are described below.

-Cyclotron resonance in metals-

In the case of metals, the microwave radiation decays with distance z into a conducting material as $\exp(-z/\delta)$, where

$$\delta = \left(\frac{2}{\mu_0\omega\sigma}\right)^{1/2} \qquad (3.25)$$

is the skin depth, μ_0 and σ are the permeability and the conductivity of the material, respectively, and ω is the angular frequency of the radiation. Fig. 3-8 shows the frequency dependence of the skindepth for copper, iron and titanium. For example, copper which have a good conductivity σ~5.88x10^7 Sm^{-1}, has typical values of δ~70 μm at 1 MHz and δ~0.7 μm at 10 GHz. Therefore, from eq.(3.25), the more the material has good conductivity and the frequency is high, the more the skindepth will be smaller. When the magnetic field is applied to the electrons, the electrons will perform cyclotron motion with the cyclotron radius

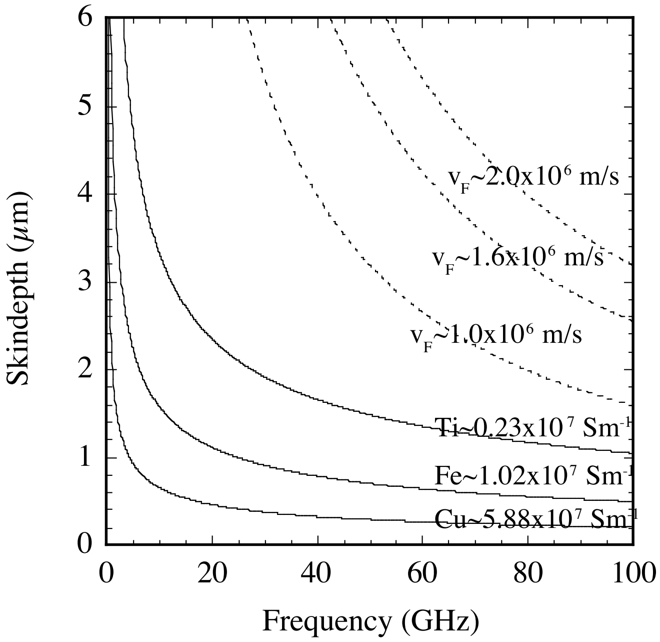

Fig. 3-8 The frequency dependence of the skindepth (solid line) and cyclotron radius (broken line).

$$R = \frac{v_F}{\omega_c}. \qquad (3.26)$$

Considering that most of metals' Fermi velocity are v_F~1.5x10^6 m/s, we can see in Fig. 3-8 that the skindepth is smaller than the cyclotron radius in the frequency range used for CR measurements. In such a case, the radiation can not penetrate enough to interact with the cyclotron motion. However, If the magnetic field is applied parallel to a surface of the crystal and oscillatory E field is arranged to be perpendicular to the magnetic field and parallel to the surface as shown in Fig. 3-9, the electrons will perform a helical motion and will periodically penetrate into the skin layer to pick up the energy from the alternating electric field. This results in absorption of energy whenever

$$\omega = n\omega_c \qquad (3.27)$$

where n is an integer. Usually ω is kept constant and the magnetic field B is swept, so that the absorption lines are uniformly spaced in $1/B$. This type of CR in metals is also called Azbel'-Kaner CR and as in the case of quantum oscillations, low temperatures and high magnetic field are required.

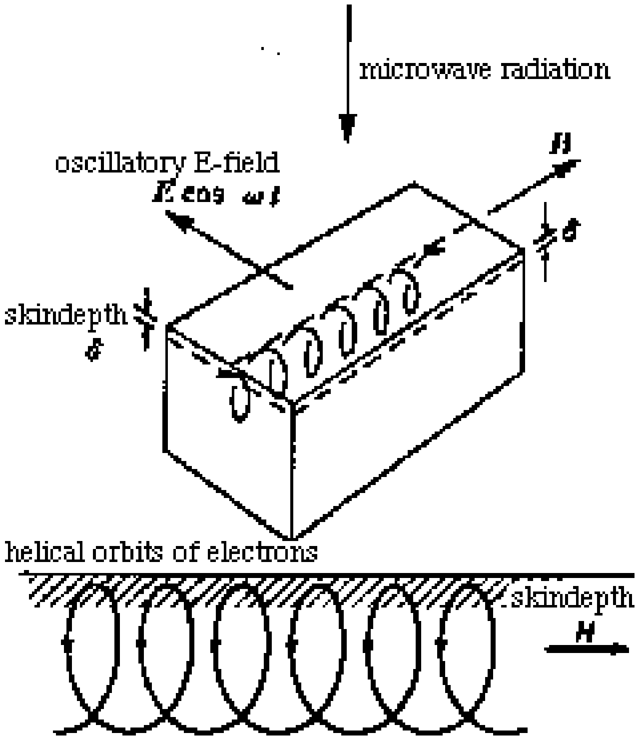

Fig. 3-9 Geometry of a cyclotron resonance in metals.

-Cyclotron resonance in semiconductors-

The densities of carriers in semiconductor samples are much lower than those in metals, therefore, the radiation can completely penetrate through the entire sample. In this case, the whole cyclotron orbits experiences the oscillatory *E*-field of the radiation. If we consider the carrier's equation of motion when magnetic field *B* and oscillatory *E*-field are applied, the equation will be

$$m\frac{dv}{dt}+\frac{mv}{\tau}=e(E+(v\times B)). \qquad (3.28)$$

If *B*=(0,0,*B*) and *E* is defined as *E*exp(*iωt*), we obtain the conductivity tensor by using eq.(3.28) and $nev_i=\sigma_{ij}E_j$,

$$\sigma_{xx}=\sigma_{yy}=\sigma_0\tau^{-1}\frac{\tau^{-1}+i\omega}{\left(\tau^{-1}+i\omega\right)^2+\omega_c^2}, \qquad (3.29)$$

$$\sigma_{xy}=-\sigma_{yx}=\sigma_0\tau^{-1}\frac{\omega_c}{\left(\tau^{-1}+i\omega\right)^2+\omega_c^2}, \qquad (3.30)$$

$$\sigma_{zz} = \frac{\sigma_0 \tau^{-1}}{\left(\tau^{-1} + i\omega\right)},$$

where $\sigma_0 = ne^2\tau / m$. If a right-handed circularly polarized light (i.e. $E_y=-iE_x$) is considered, the conductivity will be from eqs.(3.29) and (3.30),

$$\sigma_+ = \frac{j_x}{E_x} = \sigma_{xx} + \sigma_{xy}\frac{E_y}{E_x} = \frac{\sigma_0 \tau^{-1}}{\tau^{-1} + i\left(\omega + \omega_c\right)}, \quad (3.31)$$

and we have, in the same way, the conductivity for left-handed circularly polarized light,

$$\sigma_- = \frac{\sigma_0 \tau^{-1}}{\tau^{-1} + i\left(\omega - \omega_c\right)}. \quad (3.32)$$

The power absorbed by carriers can be obtain from the following equation,

$$P(\omega) = \frac{1}{2}\mathrm{Re}\{jE\}. \quad (3.33)$$

Hence, the power dissipation of each circularly polarized light absorbed by carriers will be

$$P_\pm(\omega) = \frac{1}{2}|E|^2 \mathrm{Re}\left\{\frac{\sigma_0 \tau^{-1}}{\tau^{-1} + i\left(\omega \pm \omega_c\right)}\right\} = \frac{1}{2}|E|^2 \frac{\sigma_0 \tau^{-2}}{\tau^{-2} + \left(\omega \pm \omega_c\right)^2}, \quad (3.34)$$

and for a linearly polarized light which is a mixture of right and left-handed circularly polarized light,

$$P(\omega) = P_+(\omega) + P_-(\omega) = \sigma_0 |E|^2 \frac{1 + \left(\omega^2 + \omega_c^2\right)\tau^2}{\left[1 + \left(\omega^2 - \omega_c^2\right)\tau^2\right]^2 + 4\omega_c^2\tau^2}. \quad (3.35)$$

Eq.(3.35) suggests that there will be resonant absorption at $\omega=\omega_c$ (i.e. CR). We show in Fig. 3-10, the simulation of the CR's power dissipation with different $\omega\tau$. We assumed that the cyclotron effective mass is $m^*=m_e$ and the frequency is set to 60 GHz. We can clearly see that the absorption becomes visible when $\omega\tau$ is larger than 1. Therefore, the condition $\omega\tau \sim \omega_c\tau > 1$ is needed to observe CR which suggests that high-frequency, high field, good sample quality and low temperature are required to satisfy the condition. The linewidth of the resonance can give the information about the scattering time τ. The FWHM (full width half maximum) of the absorption of eq.(3.34) is

$$\Delta\omega = \frac{2}{\tau}. \quad (3.36)$$

However, in general, we perform measurements by fixing the frequency and sweeping the magnetic field. Therefore, if we translate eq.(3.36) by magnetic field, we have

$$\Delta B = \frac{2m^*}{e\tau} = \frac{2B_{res}}{\omega\tau} \qquad (3.37)$$

where B_{res} is the resonance field and ΔB is the linewidth. Then, we can obtain the scattering time directly from the resonance field and resonance linewidth by using eq.(3.37).

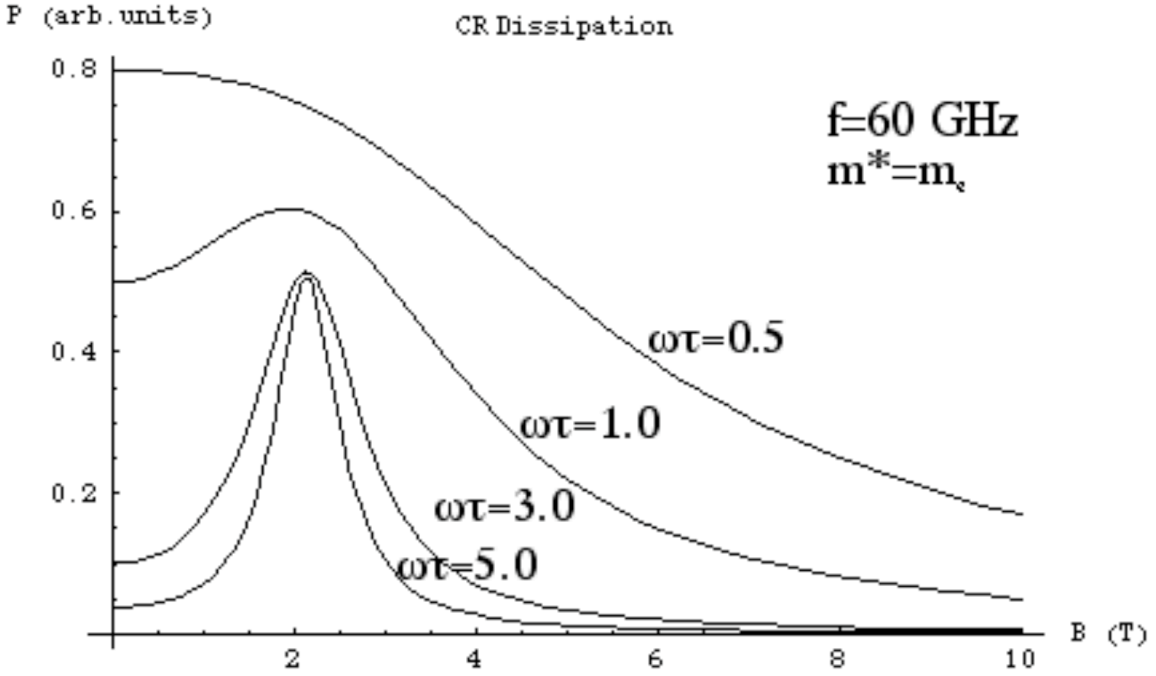

Fig. 3-10 Simulation of the cyclotron resonance power dissipation with different ωτ. The observed frequency is set to 60 GHz.

3.3.2 Kohn's theorem

We have seen in the above sections that the effective mass *m** can be obtained from the quantum oscillation measurements (e.g. dHvA, SdH oscillations) and CR measurements. However, the cyclotron mass measured in a CR experiment should not, in theory, contain any contribution from the interaction between the carriers. This was first pointed out by Kohn and it is now known as the Kohn's theorem [11]. Kohn's argument is very simple. If an electron gas with short-range interactions *U* in a uniform magnetic field *B* is considered, the Hamiltonian can be written as follows

$$H = \frac{1}{2m^*}\sum_{i=1}^{N} P_i^2 + U, \quad (3.38)$$

where

$$P_i = \left[p_{i,x}, p_{i,y} + (eB)x_i, p_{i,z}\right],\ U = \sum_{i,j} u(r_i - r_j).$$

The equation of motion for *i*-th electron is, then,

$$\frac{dp_i}{dt} = -\frac{e}{m^*} p_i \times B - \sum_j grad_i\left[u(r_i - r_j)\right]. \qquad (3.39)$$

However, if we define eq.(3.39) as a whole system, we can cancel the second term of eq.(3.39) and can be rewritten as follows,

$$\frac{dP}{dt} = -\frac{e}{m^*} P \times B, \qquad (3.40)$$

where $P \equiv \sum_i P_i$. We can see from eq.(3.40) that the time dependence of the total momentum is not affected by the electron-electron interactions and is only depending to the applied magnetic field. Therefore, CR measurement, where the microwave is coupled to the whole electron system, could not be affected by the electron-electron interaction. Next, by using the Heisenberg's equation of motion, eq.(3.40) becomes

$$\frac{i}{\hbar}\left[H, P\right] = -\frac{e}{m^*} P \times B. \qquad (3.41)$$

If we assume the magnetic field is applied to the *z*-axis and define $P_\pm \equiv P_x \pm iP_y$. Then by eqs.(3.24) and (3.41), we have

$$\left[H, P_\pm\right] = \pm\hbar\omega_c P_\pm. \qquad (3.42)$$

Now let Ψ_0 be the true ground state of the system (or any other eigen state), and operate on Ψ_0 with eq.(3.42). Denoting $H\Psi_0 = E\Psi_0$, we have

$$HP_+\Psi_0 - E_0 P_+\Psi_0 = \hbar\omega_c P_+\Psi_0. \qquad (3.43)$$

Hence, if $\Psi_1 \equiv P_+\Psi_0$ is defined, we can see that Ψ_1 is an exact excited eigen state of *H* with the energy

$$E_1 = E_0 + \hbar\omega_c. \qquad (3.44)$$

Therefore, if the microwave is applied homogeneously on the sample, we can have excitations when $\omega=\omega_c$ (i.e. CR) and the cyclotron frequency ω_c (i.e. the effective mass) is not affected by the interaction *U*.

The Kohn's theorem is based on a electron gas in a Galilean invariant system. Thus, the theorem needed to be considered in more realistic situations. Kanki and

Yamada have calculated the effects of the electron-electron interaction to the cyclotron resonance frequency on the basis of the Fermi liquid theory and they have proved that the Kohn's theorem is valid in Galilean invariant system [59]. Therefore, the CR measures the dynamical mass

$$m^*_{CR} \approx (1 + \lambda_{e-p})m_b, \qquad (3.45)$$

where m_b is the cyclotron mass calculated in the bandstructure calculation and λ_{e-p} is the electron-phonon interactions, whereas thermodynamic measurement such as dHvA oscillations reveals the effective mass m^*_{QO} which also contains contributions from the electron-electron interactions λ_{e-e} (i.e. $m^*_{QO} = (1 + \lambda_{e-e})(1 + \lambda_{e-p})m_b$). This implies that, if the Kohn's theorem is valid, the contribution of the electron-electron interactions λ_{e-e} can be estimated by comparing the effective mass obtained from CR and quantum oscillations measurements. However, Kanki and Yamada have also mentioned from the calculations that in the real situation, i.e., Bloch electrons in metals, Galilean invariance is broken and the cyclotron frequency ω_c tends to be reduced from the cyclotron frequency of non-interacting electrons which means that the effective mass m_{CR}* might be enhanced. However, the CR's effective mass is still not comparable with the effective mass obtained from the quantum oscillations and can be comparable in only some extreme situations such as near half-filling on square lattice [59]. Experimentally, the difference between the two masses are not seen in pure metals, such as Alkali metals, Cu, etc., which is considered that the effects of electron-electron interactions is rather small. However, the difference of masses are seen in some semiconductors, layered perovskite superconductors and organic conductors [2,3,10,60]. Therefore, it is interesting to examine if the Kohn's theorem is also valid in the organic conductors which have simple FS.

The above consideration have motivated a number of attempts to observe CR in charge transfer salts. However, by attempting magnetooptical measurements on organic conductors, new phenomena in resonant absorption started to be observed. We will describe these new phenomena in the following sections.

3.3.3 Periodic orbit resonance

We have seen above that CR is a powerful technique where we can measure directly the cyclotron frequency ω_c, i.e., the effective mass. However, recent magnetooptical measurements studies have shown that the mechanisms responsible for the resonant absorption lines are quite different from the well-known CR and these new resonant absorption lines can be explained semiclassically. Hill has demonstrated that, in q2D conductors, there exists resonant absorption in the interlayer conductivity which arises from the periodic modulation of carrier's velocity [12] and this resonance is named as "periodic orbit resonance (POR)". In this section, we will follow the POR theoretically and see its properties.

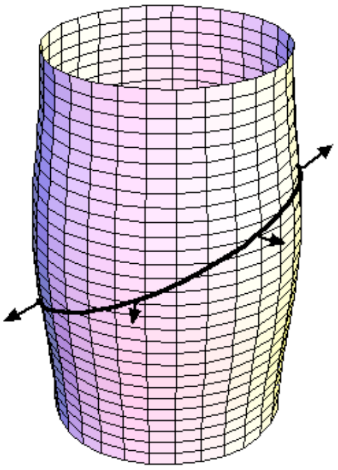

Fig. 3-11 Schematic figure of q2D Fermi surface. The thick line and the arrows represent the quasiparticles' trajectories around the FS caused by the application of a tilted magnetic field and its carriers' velocities, respectively.

First, let us consider a q2D FS as shown in Fig. 3-11 where the energy dispersion is given by

$$E(k) = \left(\frac{\hbar^2 k_x^2}{2m_{xx}} + \frac{\hbar^2 k_y^2}{2m_{yy}} \right) - 2t_c \cos(k_z c). \qquad (3.46)$$

When the magnetic field is tilted away from the cylinder axis by an arbitrary angle, the carriers trajectories which are the plane perpendicular to the applied magnetic field, will follow the path as described in the thick line of Fig. 3-11. Then, the path, in terms of the cylindrical coordinates k_z and Φ, can be written as follows

$$\begin{aligned} k_x &= k_{fx}\left[1 + \delta_x \cos\left\{\left(k_z - \kappa \cos\Phi\right)c\right\}\right]\cos\Phi \\ k_y &= k_{fy}\left[1 + \delta_y \cos\left\{\left(k_z - \kappa \cos\Phi\right)c\right\}\right]\sin\Phi \end{aligned} , \qquad (3.47)$$

where k_{fx} and k_{fy} are the Fermi wave vectors along the k_x and k_y axes, δ_x and δ_y are the amplitude of the warping in the k_x and k_y directions, and κ is related to the tilting angle θ such that $\kappa = k_{fx}\tan\theta$. To obtain the interlayer conductivity, we need to know the z components of the carrier velocities v_z at the FS. And we can obtain v_z by using eq.(3.47) and the following equations,

$$v_z = \frac{1}{\hbar}\frac{\partial E_z}{\partial k_z}, E_z = \varepsilon_F - \left(\frac{\hbar^2 k_x^2}{2m_{xx}} + \frac{\hbar^2 k_y^2}{2m_{yy}}\right). \qquad (3.48)$$

Assuming that $\kappa c << 1$, where $\sin\theta \sim \theta - \theta^3/6$, $\cos\theta \sim 1 - \theta^2/2$, and neglecting δ_x^2 and δ_y^2, we have

$$v_z = \frac{\varepsilon_F \delta_x c}{\hbar}\left[\sin(k_z c)\{(1+\Delta)+(1-\Delta)\cos 2\Phi\} - \left(\frac{\kappa c}{2}\right)\cos(k_z c)\{(3+\Delta)\cos\Phi + (1-\Delta)\cos 3\Phi\}\right], (3.49)$$

where $\Delta = \delta_y/\delta_x$. Now considering that the magnetic field is applied along z axis, the carriers will circulate the plane perpendicular to the magnetic field with the cyclotron frequency $\omega_c = eB/m_{//}$ where $m_{//}$ is the in-plane average effective mass (i.e. if the magnetic field is tilted $m_{//}$ becomes $m_{//}/\cos\theta$) and the Φ can be rewritten as $\Phi = (\omega_c t + \phi)$ where ϕ is the azimuthal coordinate for a particular carrier at the time $t=0$. Considering this, we can see, in eq.(3.49), that the v_z contains oscillatory components of ω_c, $2\omega_c$ and $3\omega_c$. Furthermore, if the magnetic field is applied parallel to the warping axis (i.e. $\kappa = 0°$), the oscillatory component is only $2\omega_c$.

As it was for q1D ADMRO's case (see section 3.2), we can obtain the frequency dependent conductivity from the Boltzmann transport equation (eq.(3.15)). Therefore, by using eqs.(3.15) and (3.49), we obtain the interlayer conductivity [61]

$$\sigma_{zz}(\omega) = const \times [A_0\Omega_0 + A_1\Omega_1 + A_2\Omega_2 + A_3\Omega_3], \qquad (3.50)$$

$$A_0 = \frac{1}{16}\{2(1+\Delta^2)(3+\Lambda^2) + (1-\Delta^2)(1-\Lambda^2)\},$$

$$A_1 = \left(\frac{\kappa c}{8}\right)^2\{(3+\Lambda^2)(3+\Delta)^2 + 2(1-\Lambda^2)(3+\Delta)\},$$

$$A_2 = \frac{1}{16}(1-\Delta)^2\{(3+\Lambda^2) + (1-\Lambda^2)\},$$

$$A_3 = \frac{1}{2}\left(\frac{\kappa c}{8}\right)^2(1-\Delta)\{2(3+\Lambda^2)(1-\Delta) + (1-\Lambda^2)(3+\Delta)\}.$$

where Λ is the ellipticity of the FS, given by the ratio k_{fy}/k_{fx}, and

$$\Omega_n = \left[\frac{1+i(\omega - n\omega_c)\tau}{1+(\omega - n\omega_c)^2\tau^2}\right] + \left[\frac{1+i(\omega + n\omega_c)\tau}{1+(\omega + n\omega_c)^2\tau^2}\right]. \qquad (3.51)$$

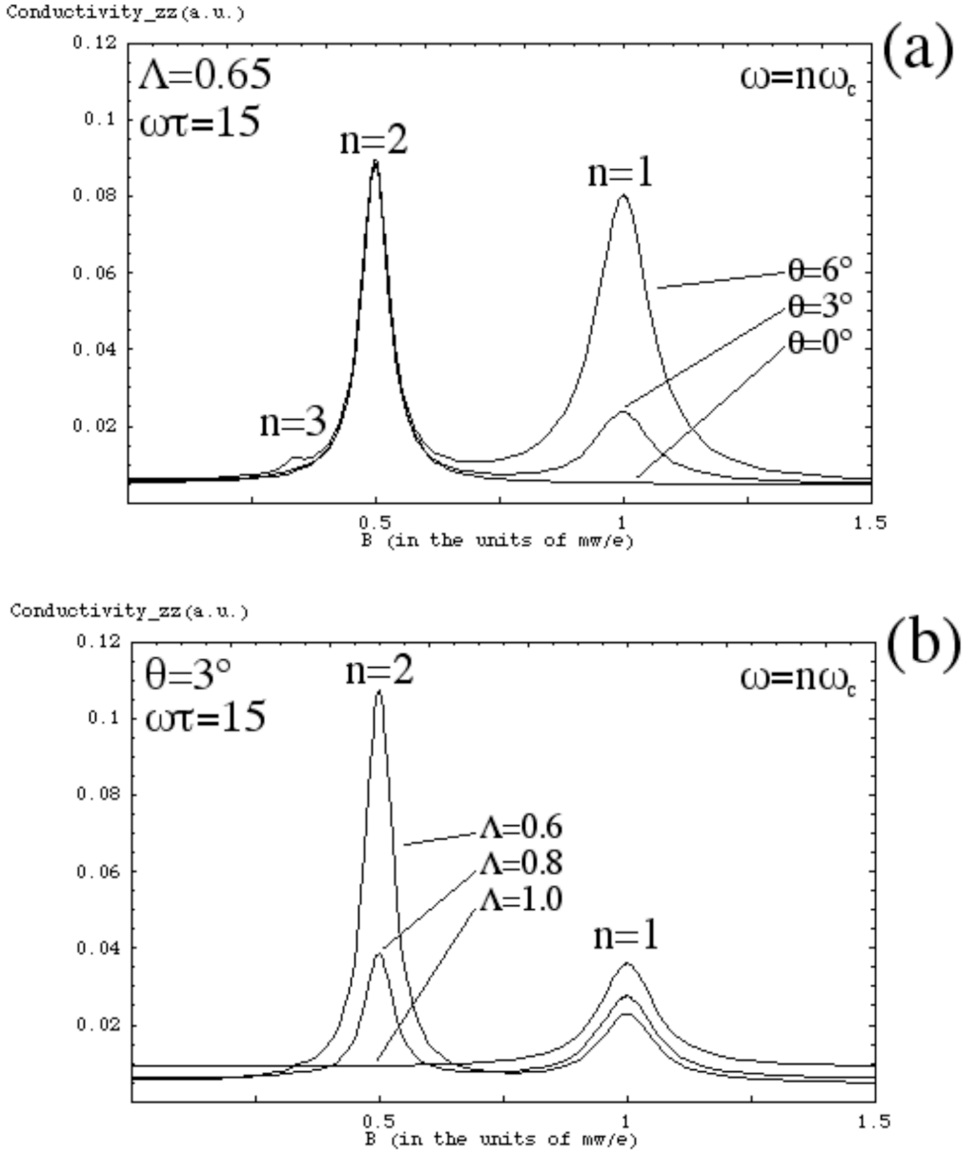

Fig. 3-12 Simulation of the real part of the interlayer conductivity σ_{zz} plotted against the magnetic field (normalized to $m_{//}\omega/e$), as a function of (a) the angle θ assuming Λ=0.65, and (b) the ellipticity, Λ, assuming θ=3°. $\omega\tau$ is set both to 15.

Figure 3-12(a) shows simulations of the real part of the interlayer conductivity $\sigma_{zz}(\omega)$ as a function of magnetic field which is normalized to $m_{//}\omega/e$, for several angles. For the purposes of the simulations, the value Λ=0.65 and ωτ=15 and $\Delta=\Lambda^2$, is assumed in eqs.(3.50) and (3.51). As predicted, three resonances in $\sigma_{zz}(\omega)$ can be seen in Fig. 3-12(a), one at the fundamental position (i.e. n=1) and the second (n=2) and the third (n=3) harmonics at the 1/2 and 1/3 position of the fundamental resonance, respectively. It is interesting to see that the second harmonic is dominant up to θ=6° and the fundamental resonance is not seen when the field is applied correctly to the warping axis (i.e. θ=0°). This is the characteristic feature of POR. Figure 3-12(b) shows further simulations of the interlayer conductivity $\sigma_{zz}(\omega)$ for different ellipticity Λ when θ=3°. It is clear that an elliptic FS is needed to observe the second harmonic of POR. Consequently, fundamental resonance of POR is very sensitive to the orientation of the magnetic field, whereas the second harmonic of POR is relatively insensitive to rotation. When the field is applied correctly to the warping axis (i.e. θ=0°), the intensity of fundamental resonance is zero which means there is no $\omega=\omega_c$ modulation in the z-axis (i.e. the electronic system is highly 2D). Therefore, the fundamental POR is similar to the origin of q2D ADMRO effect and it is expected that the intensity of fundamental POR shows oscillations similar to the q2D ADMRO. Moreover, if we renormalize the interlayer ac conductivity $\sigma_{zz}(\omega)$ with the dc conductivity $\sigma_{zz}(0)$, eq.(3.50) can be described as,

$$\sigma_{zz}(\omega) = \frac{\sigma_{zz}(0)}{2A_{total}}\left[A_0\Omega_0 + A_1\Omega_1 + A_2\Omega_2 + A_3\Omega_3\right], \qquad (3.52)$$

where $A_{total}=A_0+A_1+A_2+A_3$. In the magnetooptical measurements, the power dissipation of the resonance is proportional to the square root of the resistivity. Therefore, the intensity of POR is also related with the interlayer dc resistivity.

As it was for the CR's case, the linewidth of POR is related with the scattering time τ. The FWHM (full width half maximum) of the absorption can be obtained from the real part of eq.(3.51) where it is the same linewidth with CR's case.

$$\Delta\omega = \frac{2}{\tau}. \qquad (3.53)$$

However, we perform the measurements by fixing the frequency and sweeping the magnetic field. Therefore, if we translate eq.(3.53) by magnetic field, we have

$$\Delta B_n = \frac{2m^*}{ne\tau} = \frac{2B_{res,n}}{n\omega_c\tau}, \quad (3.54)$$

where ΔB_n and $B_{res,n}$ is the linewidth and the resonance field for n-th (harmonic) POR, respectively. Then, we can obtain the scattering time directly from the resonance field and the resonance linewidth of POR by using eq.(3.54). Figure 3-13 shows the simulation of eq.(3.50) for different $\omega\tau$. As for the previous case, the value Λ=0.65 and θ=3° is assumed. It is obvious that the POR can be observed when $\omega\tau$ is larger than the unity. Therefore, the condition $\omega\tau\sim\omega_c\tau>1$ is required to observe POR which suggests that the high field, good sample quality and low temperature are required to satisfy the condition. However, if the fundamental POR is not strong enough, only the 2nd harmonic of POR is observable at $\omega\tau\sim1$.

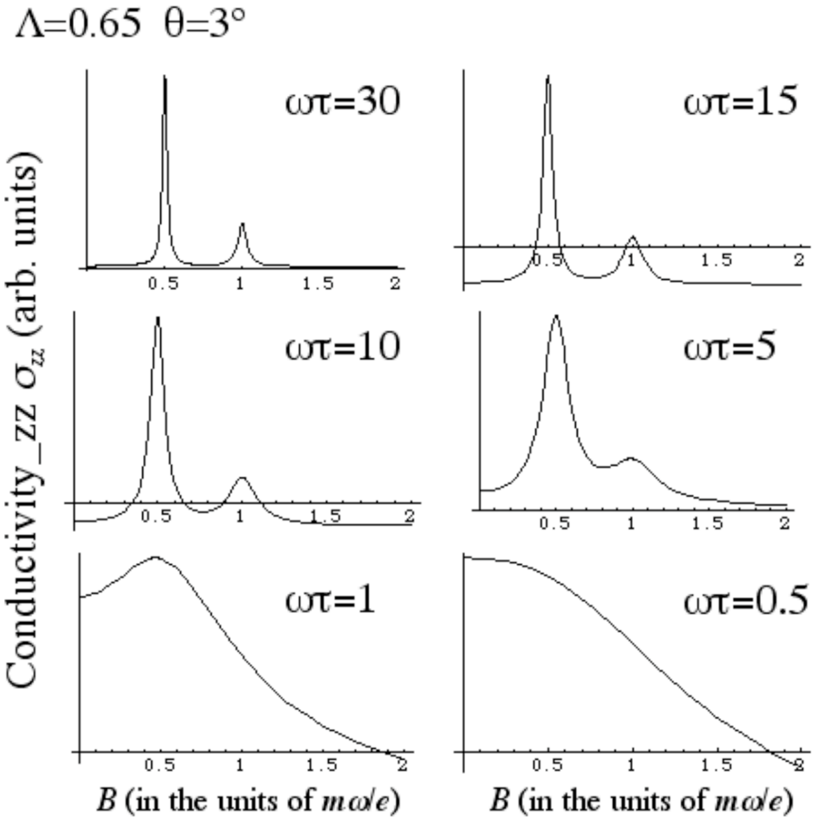

Fig. 3-13 Simulation of the real part of the interlayer conductivity σ_{zz} plotted against the magnetic field (normalized to $m_{//}\omega/e$), as a function of $\omega\tau$, assuming Λ=0.65 and θ=3°.

3.3.4 Fermi traversal resonance, q1D-periodic orbit resonance

We have seen in the previous section that the q2D FS will bring a periodic modulation of the carrier's velocity under the magnetic field and this leads to a POR. In this section, we will see that not only the q2D FS but also the q1D FS will modulate the carrier velocity when the magnetic field is applied parallel to the q1D FS where this modulation will lead to the resonant absorption of interlayer ac conductivity. This kind of resonance was first pointed out by Ardavan *et al.* where they named it as the "Fermi traversal resonance (FTR)" [13]. However, more precise work has been done by Kovalev *et al.* where they call the resonance "q1D-periodic orbit resonance (q1D POR)" [16]. Then, we will see below that the resonance is closely related with the q1D ADMRO (i.e. Lebed resonance). Therefore, this is also called as "high-frequency ADMRO". Hereafter, we will use "q1D POR" in contrast to (q2D) POR which was presented in the previous section.

The origin of q1D POR is simple. Only we have to do is considering the interlayer ac conductivity of the carrier on the q1D FS where the magnetic field is applied parallel to the q1D FS (Fig. 3-14) and this is already obtained, in section 3.2, for the explanation of the q1D ADMRO (Lebed resonance) origin. We remind that we have started from the q1D FS model in the oblique crystal lattice system where the lattice vector is R_{mn}=(0, *mb*+*nd*, *nc*) (see Fig. 3-14) and the q1D energy band is

$$E(k) = \hbar v_F\left(|k_x| - k_F\right) - \sum_{m,n} t_{mn}\cos((mb+nd)k_y + nck_z). \qquad (3.55)$$

From eqs.(2.8), (2.9) and the Boltzmann transport equation (i.e. eq.(3.15)), the frequency dependent conductivity matrix is obtained,

$$\begin{pmatrix} \sigma_{yy}(\omega) & \sigma_{yz}(\omega) \\ \sigma_{zy}(\omega) & \sigma_{zz}(\omega) \end{pmatrix} = N(E_F)\frac{e^2\tau}{\hbar^2}\sum_{m,n}\begin{pmatrix} (mb+nd)^2 & (mb+nd)nc \\ (mb+nd)nc & (nc)^2 \end{pmatrix}\frac{t_{mn}^2}{1+\left\{(\omega - v_F G_{mn})\tau\right\}^2}, \qquad (3.56)$$

$$G_{mn} = eB\left[(mb+nd)\cos\theta - nc\sin\theta\right]/\hbar. \qquad (3.57)$$

where *m,n* are integers and *c* is the interlayer spacing, *b* is the in-plane lattice spacing (parallel to q1D FS), and *d* is the obliquity parameter defined at the right of Fig. 3-14.

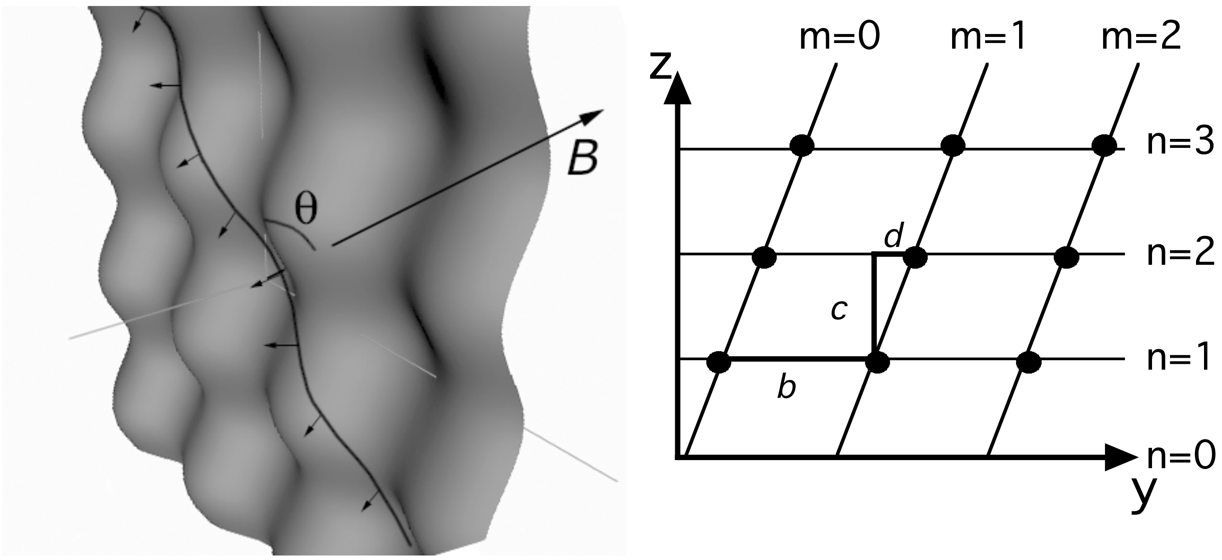

Fig. 3-14 Schematic figure of the quasiparticle trajectory for a magnetic field applied at an arbitrary angle θ away from the k_z-axis at the left. The periodic modulation of the carrier's velocities are represented by the arrows. And the definition of oblique crystal lattice at the right.

In the case of q1D ADMRO, the resonance condition of eq.(3.56) was G_{mn}=0 because we have taken ω=0. Now we consider a finite ω, therefore, the resonance condition will be $\omega = v_F G_{mn}$ and we note that $v_F G_{mn}$ is the frequency oscillation of the velocity due to the Fourier component of the FS corrugation corresponding to integers *m* and *n*. This suggests that when the measurement frequency matches the velocity modulation frequency, it will cause a resonant absorption. By using eq.(3.57), the resonance condition $\omega=v_F G_{mn}$ can be written as follows,

$$\frac{\nu}{B_{res}} = \frac{ev_F}{h}\left[(nc)^2 + (mb+nd)^2\right]^{1/2}\left|\sin(\theta-\theta_{mn})\right|, \qquad (3.58)$$

$$\tan\theta_{mn} = \frac{m}{n}\frac{b}{c} + \frac{d}{c}, \qquad (3.59)$$

$$n=0,1,2,..., \quad m=0,\pm1,\pm2,...$$

where ν is the measurement frequency, B_{res} is the resonance field for q1D POR and θ is the angle of the magnetic field rotated from the *z*-axis to the *y*-axis. Figure 3-15 shows the simulation of q1D POR plot as a function of the rotated angle by using eqs.(3.58) and (3.59). The values *b*=5 Å, *c*=15 Å, *d*=0 Å and v_F=1.0x10^5 m/s were used for the simulation. We note that only (*m,n*)=(1,0),(2,0),(-1,1),(1,1),(-2,1),(2,1) resonance of q1D POR are considered where the thick sinusoidal curves represent (1,0) and (2,0) resonances and the fine sinusoidal curves represent (-1,1) and (1,1) resonances and the broken curves are (-2,1),(2,1). The intersection of the sinusoidal curves and ν/B_{res}=0 correspond to the angle θ_{mn} where Lebed resonance is observed.

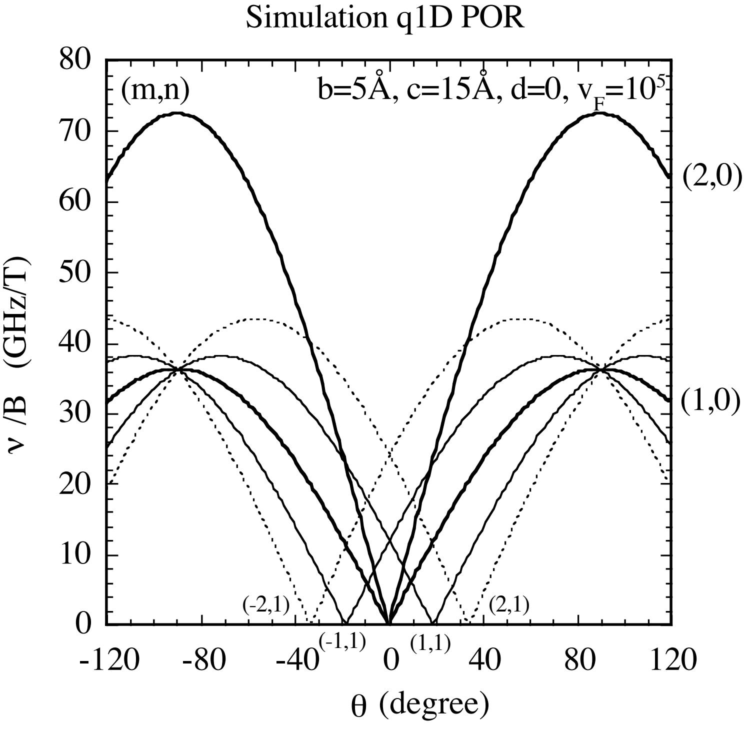

Fig. 3-15 Simulation of the q1D POR plot as a function of the field orientation θ. The values *b*=5Å, *c*=15Å, *d*=0Å and v_F=1.0x10^5 m/s are assumed.

In general, we perform measurements by fixing the frequency and the angle, and sweeping the magnetic field. Therefore, it is possible to observe several absorption lines (harmonics) by sweeping the magnetic field. However, there are some angles where the resonance points are degenerated. Moreover, as we will see below, the amplitude of the resonance is related to its effective transfer integral which means that the more the integer value of *m* and *n* are large, the more the intensity of the (*m,n*) resonance will decrease. Therefore, in principle, it is difficult to observe the high-order harmonics such as (2,-1),(2,0),(2,1) in the above case. By fitting the POR plot with eq.(3.58), we can obtain directly the Fermi velocity v_F from the amplitude of the sinusoidal curve.

We have seen in eq.(3.56) that q1D POR is resonant absorption lines of interlayer ac conductivity. And if we look at eq.(3.56) attentively, the interlayer ac conductivity $\sigma_{zz}(\omega)$ is proportional to $(nc)^2 t_{mn}{}^2$. This has two meanings, first, the amplitude of q1D POR is related to the effective transfer integrals

$$t_{mn} = \frac{1}{\dfrac{m^2}{t_b} + \dfrac{n^2}{t_c}}, \qquad (3.60)$$

which means that the amplitude of high-order harmonics with large *m,n* is weak, and secondly, there is no contribution of $(m,n)=(m,0)$ resonance in q1D POR because the amplitude will be zero when $n=0$. Furthermore, If we renormalize eq.(3.56) with the dc conductivity, eq.(3.56) becomes

$$\sigma_{zz}(\omega) = \sigma_{zz}(0) \sum_{m,n} \frac{(nt_{mn})^2 / t_c^2}{1 + \left\{(\omega - v_F G_{mn})\tau\right\}^2}. \qquad (3.61)$$

Therefore, the intensity of q1D POR is also related to the interlayer dc resistivity.

As it was for CR and q2D POR, the resonance linewidths of q1D POR is also related to the scattering time τ. The FWHM (full width half maximum) of the absorption can be obtained from the eq.(3.56) where it is the same linewidth with CR's case,

$$\Delta\omega = \frac{2}{\tau}. \qquad (3.62)$$

If eq.(3.62) is translated to the magnetic field by using $\omega = v_F G_{mn}$ and eq.(3.57), we have

$$\Delta B_{(m,n)} = \frac{2\hbar}{ev_F \tau\left[(mb + nd)\cos\theta - nc\sin\theta\right]} = \frac{2B_{res,(m,n)}}{\omega\tau}, \qquad (3.63)$$

where $\Delta B_{(m,n)}$ and $B_{res,(m,n)}$ is the linewidth and the resonance field for (*m,n*) resonance of q1D POR, respectively. Then, we can obtain the scattering time directly from the resonance field and resonance linewidth of POR by using eq.(3.63).

Finally, we note that the q1D POR observation is the most straightforward way to obtain the Fermi velocity and the scattering time in q1D conductors, and (*m,n*) can be obtained separately in contrast with the ADMRO measurements where only the value *m*/*n* is obtained.

3.4. Magnetooptical measurement techniques

We have seen in section 3.3, several kinds of resonant absorption lines, in magnetooptical measurements, which are coming from the closed FS (i.e. CR) or the corrugated q1D/q2D FS (i.e. POR). We have seen also that all these resonances need low temperature, high field, high frequency. In this section, we will present the experimental techniques for probing these resonances.

3.4.1 Transmission technique

First, we will present our experiment instruments used in Kobe University where a simple transmission arrangement is adopted. The outline of the experiment setting is as follows (see also Fig. 3-16). Coherent microwave emitted from the light source will propagate the cylindrical wave guide and transmit through the sample which is set in the center of the magnet and , finally, reach the light detector. Then, we use a pulsed magnetic field which is obtained by releasing the pulsed electric current from the capacitor bank to the magnet and the magnetic field is monitored by the pickup coil which is set around the sample. Both transmission and magnetic field data is stored in the digital memory system and will be taken into the computer to convert the transmission-time and field-time data to the transmission-field data [62].

We are using two types of light source, the Gunn oscillators and backward wave oscillators (BWO). The Gunn oscillators cover the frequency range from 30 GHz to 315 GHz and the BWO covers from 118 GHz to 1.2 THz. InSb detectors are used to detect the light emitted from these light sources. We have two types of combination for capacitor bank and magnet for pulsed magnetic field where the maximum energy of the capacitor bank is 23.4 kJ and 100 kJ, and the magnetic field is up to 16 T and 40 T, respectively, and the former one were used in this study. The cryostat used for this study can cover the temperature range of 4.2 K down to 1.8 K and we have performed the magnetooptical measurements at the lowest temperature.

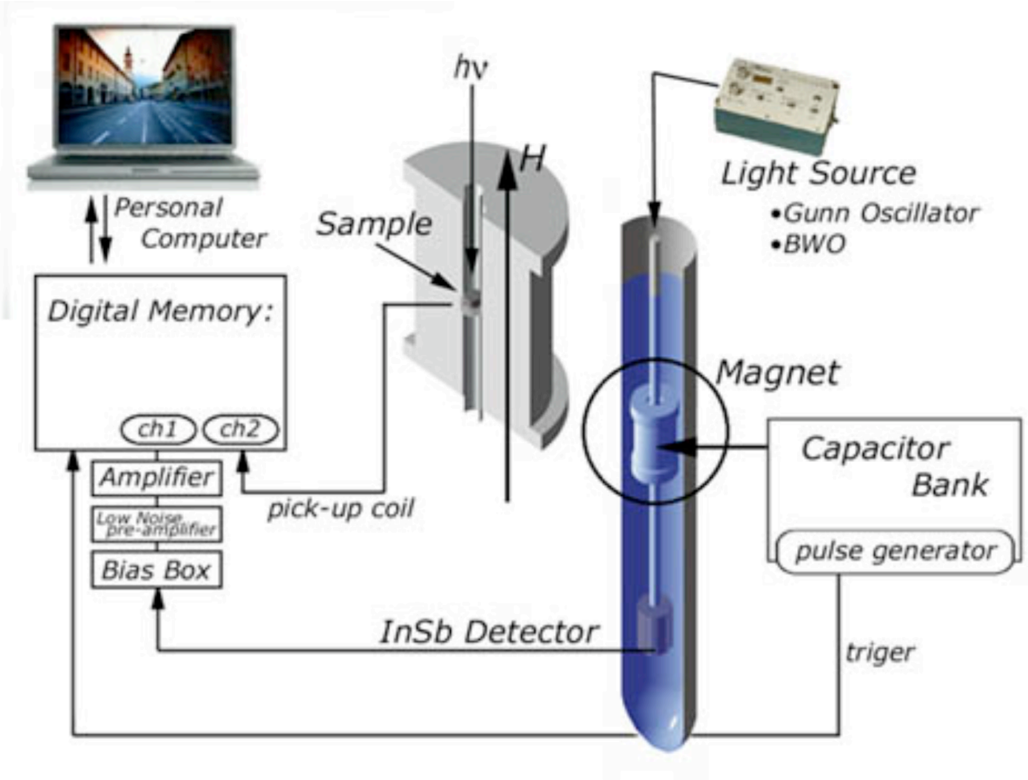

Fig. 3-16 Schematic figure of our experimental instruments for magnetooptical measurements.

The organic conductors usually have conductivities which are one order of magnitude less than copper. This means that the microwave can not transmit through the sample and two types of transmission techniques are used to solve this problem. One is the mosaique technique and the other is the strip-line technique (Fig. 3-17). In mosaique technique, we set some samples spaced each other about a few millimeters, and the propagated light will pass between the samples which interact at the side of the sample. On the other hand, in the strip-line technique, the light is reflected by the mirrors and passes through the polyethylene sheet to interact with the surface of the samples [63]. In principle, we use the mosaique technique when we have enough sample, and strip-line technique when we do not have enough sample. Therefore, for the measurements of θ-(BEDT-TTF)$_2$I$_3$ which is relatively difficult to obtain, we have performed the later transmission technique for the magnetooptical measurements. However, compared to the measurements which use resonant cavities, the control of the electromagnetic environment in the vicinity of the sample is impossible in the strip-line transmission techniques. Therefore, the observation of POR which is related to the ac interlayer conductivity is ambiguous.

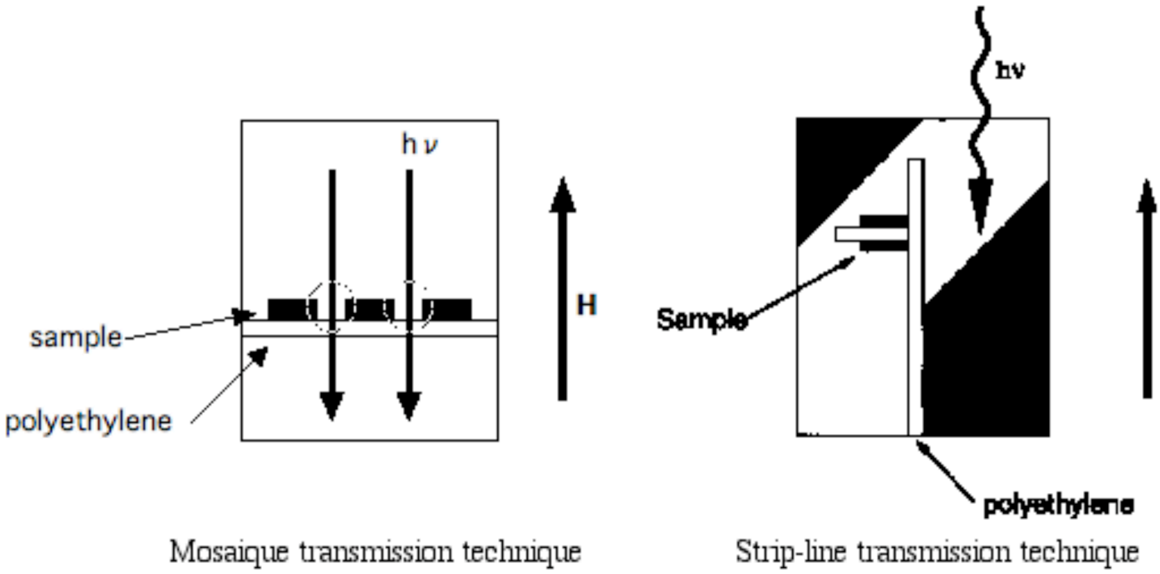

Fig. 3-17 Schematic figure of the two transmission techniques for organic conductors.

3.4.2 Cavity perturbation technique

Most of these studies have been done by using the cavity perturbation technique. In this section, we will explain briefly about the experimental instruments used and about the cavity perturbation technique.

We show in Fig. 3-18, the experimental set up of the cavity perturbation technique and the equipment used in HFLSM, IMR, Tohoku University [64]. As seen in Fig. 3-18, the measurement system consists of a cryostat, a cylindrical resonant cavity and wave guides, a 15 T superconducting magnet and, finally, a millimetre-wave vector network analyzer (MVNA) which acts as a tunable source and detector of GHz radiation. Therefore, the experimental arrangement is almost the same as the transmission techniques seen above, except the sample is set inside a resonant cavity. The measurements can be performed at the temperature between 0.5~4.2 K and the magnetic field up to 14 T and the frequency range is V- and W-bands.

-MVNA-

First, MVNA is a system including a source, a detector, a frequency drive, and a data acquisition and processing system (see Fig. 3-19). The MVNA is based on two yttrium-iron-garnet (YIG) oscillators (master and slave) which are continuously tunable between 8-18 GHz. The YIG oscillators are phase locked and the slave YIG follows the frequency of the master.

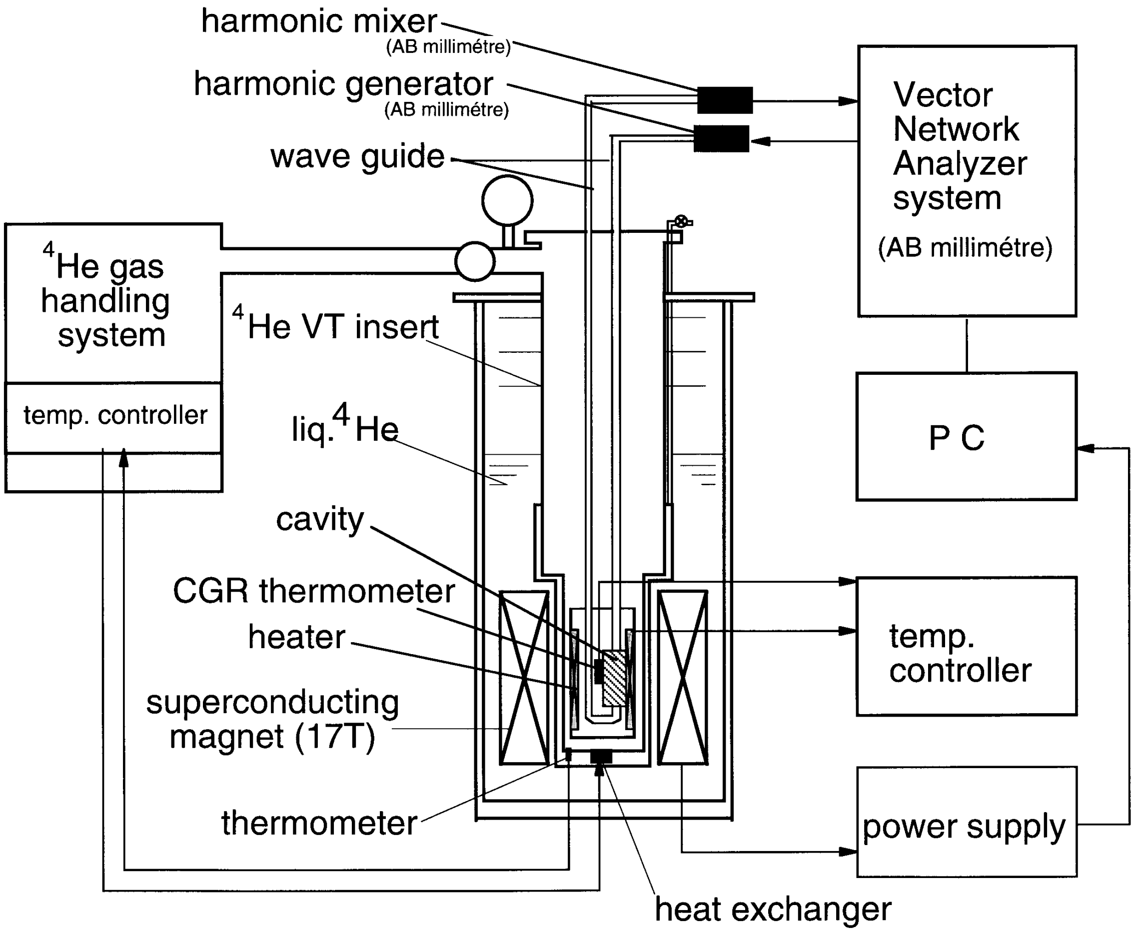

Fig. 3-18 A schematic figure of the magnetooptical measurement system using MVNA and superconducting magnet.

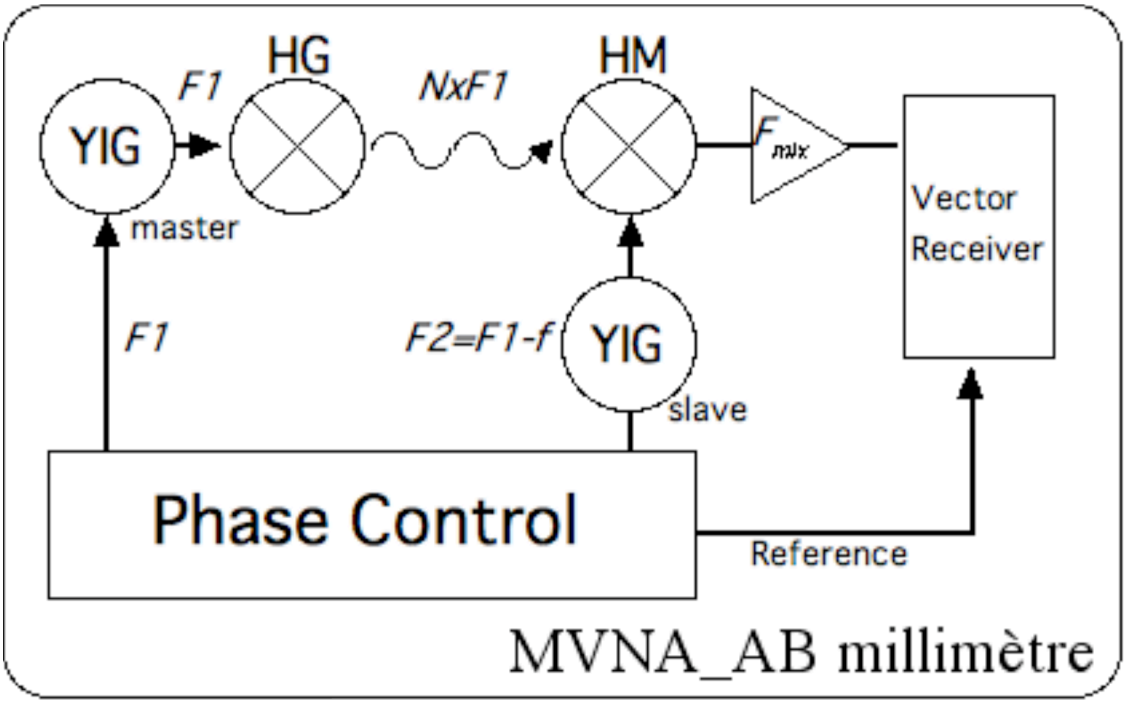

Fig. 3-19 Schematic diagram of Millimetre-wave Vector Network Analyzer (MVNA).

The master YIG is set at a frequency (*F1*) between 8 to 18 GHz and its oscillating current is sent to a Schottky diode (the harmonic generator (HG)) which acts as a transducer, emitting electromagnetic waves which are sent to the experiment. This HG Schottky diode can generate multiplied frequency of *F1*, $F_{mm}=N\text{x}F1$ with N=1,2,3... . On the other hand, the slave YIG oscillates at $F2=F1\text{-}f$, where f is a fixed frequency controlled by the computer. The signal from the slave is sent to a second Schottky diode, the harmonic mixer (HM). The HM mixes the signal received from the experiment F_{mm} with the signal from the slave ($N'\text{x}F2$) to give frequencies

$$F_{mix} = |NF1 \pm N'(F1 - f)| = Nf\,. \qquad (3.64)$$

where the same harmonic $N'=N$ is chosen and the amplitude of the detected signal F_{mm} is proportional to the amplitude of the signal from the experiment. Both YIG are phase locked to each other so that the phase noise of both YIG is canceled and the phase of the signal from the experiment is preserved;

$$\phi_{mix} = |N\phi_1 - N\phi_2 + \delta\phi|, \qquad (3.65)$$

where ϕ_1 and ϕ_2 are phases of both YIG and $\delta\phi$ is the phase shift due to the experiment. In the vector receiver, F_{mm} is downconverted by mixing with signals derived from the reference source in order to keep the phase information.

Therefore, the advantage of using MVNA is that the information of both phase and amplitude from the experiment can be obtained with the wide frequency range of 8-350 GHz.

-Cavity perturbation technique-

The resonant cavity is an indispensable item for high sensitive measurements. The merit of using resonant cavity is not only we can get high sensitive signals but also we can control the electromagnetic environment (i.e. E-field and H-field) inside the cavity. Resonant cavities can support two resonant modes due to the boundary conditions inside the cavity which are TE mode when E_z=0 and TM mode when H_z=0. The resonant TE mode, for cylindrical cavities which were used in this study, can be described in a cylindrical coordinate as follows,

<TE$_{mnp}$ mode>

$$E_r = -\frac{(\mu/\varepsilon)^{1/2} H_0 k_z}{\left(k_c^2 + k_z^2\right)^{1/2}} J_m'(k_c r)\cos m\phi \sin k_z z, \quad (3.66)$$

$$E_\phi = \frac{(\mu/\varepsilon)^{1/2} H_0 m k_z}{\left(k_c^2 + k_z^2\right)^{1/2}} \frac{J_m(k_c r)}{k_c r} \sin m\phi \sin k_z z, \quad (3.67)$$

$$E_z = \frac{(\mu/\varepsilon)^{1/2} H_0 k_c}{\left(k_c^2 + k_z^2\right)^{1/2}} J_m(k_c r)\cos m\phi \cos k_z z, \quad (3.68)$$

$$H_r = -mH_0\left[\frac{J_m(k_c r)}{k_c r}\right]\sin m\phi \cos k_z z, \quad (3.69)$$

$$H_\phi = -H_0 J_m(k_c r)\cos m\phi \cos k_z z \quad (3.70)$$

$$H_z = 0$$

where $J_m(k_c r)$ is the m-th order Bessel function and $J_m'(k_c r)$ is its derivative and

$$k = \left(k_c + k_z\right)^{1/2} = \left[\frac{\left(k_c a\right)_{mn}^2}{a^2} + \left(\frac{p\pi}{d}\right)^2\right]^{1/2} \quad (3.71)$$

where a and d are the radius and the length of the cylindrical cavity, respectively. Fig. 3-20 shows the schematic figures of typical TE$_{011}$, TE$_{012}$, TE$_{112}$ mode and Fig. 3-21 shows the frequency-cavity dimension diagram of its resonant mode. For enthusiast who are more interested in cavity resonant mode, we refer [65].

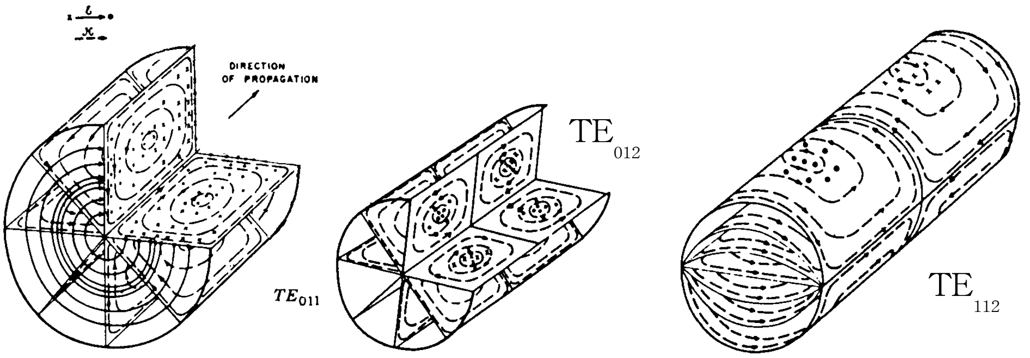

Fig. 3-20 Schematic figures of typical resonant mode TE_{011}, TE_{012}, TE_{112}. [65]

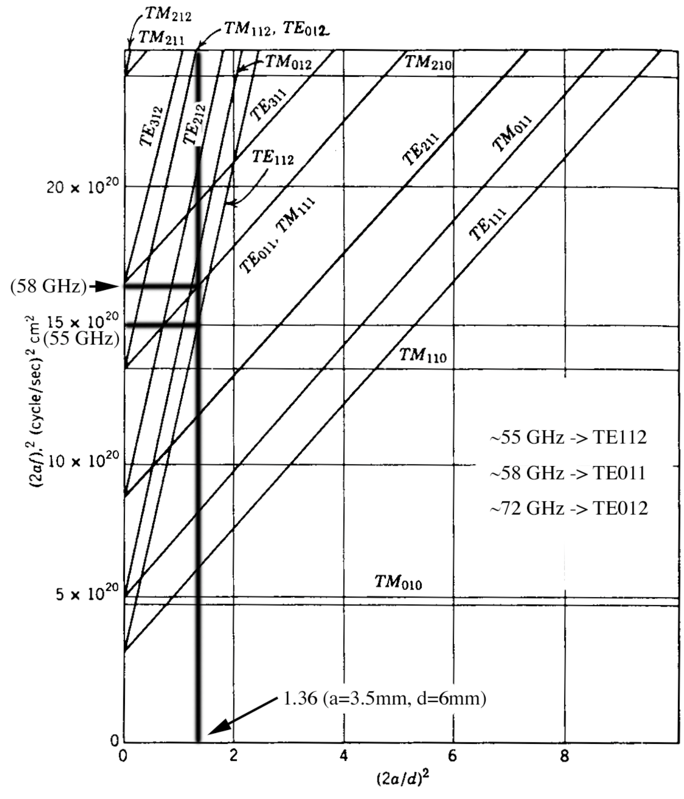

Fig. 3-21 Mode chart for cylindrical cavity of radius *a*, length *d*, and resonant frequency *f*. [65]

We have used resonant cavity size of a=3.5 mm, d=6 mm (i.e. $(2a/d)^2$~1.36) in this study. Thus, from Fig. 3-21, the resonant cavity mode for 58 GHz is TE_{011}, and the cavity modes for other frequency are shown in the inset. Therefore, we can control the electromagnetic environment inside the cavity by changing the frequency and choose which oscillatory field (i.e. *E* or *H* -field) to couple by changing the sample position inside the cavity. In general, *H*-field and *E*-field couplings are used to observe ESR and CR, respectively.

The basic principle of the cavity perturbation technique can be described as follows (also we refer the reader to a series of excellent articles [15,66,67]).

Provided that a sample placed inside a resonant cavity acts as a small perturbation of the electromagnetic field distribution within the cavity, we can determine the complex electrodynamic response of the sample from the changes of the quality factor of the resonance (Q) and the resonance frequency (ω_0). For a conducting sample, changes in quality factor and resonance frequency are directly related to changes in the surface impedance $Z_s=R_s+iX_s$, where R_s is a surface resistance and X_s is a surface reactance. The dissipation, which occurs at the surface of the sample due to R_s, generally causes changes in quality factor Q, while the dispersion, governed by X_s, results in changes in resonance frequency ω_0. The amplitude "A" and phase "ϕ" of the electric and magnetic fields of the electromagnetic waves in the cavity can be written as follows.

$$|A(\omega)|^2 = \frac{A_0^2}{(\omega_0/2Q)^2 + (\omega - \omega_0)^2} \qquad (3.72)$$

and

$$\phi = -\arctan\left(\frac{2(\omega - \omega_0)}{\omega_0/2Q}\right) \quad , \qquad (3.73)$$

where A_0 is the notional amplitude of the field supplying energy to the cavity and ω is the frequency used. Therefore, we use MVNA to monitor the phase and amplitude of millimeter-wave radiation transmitted through a resonant cavity containing the sample under investigation.

In this study, two sample positions, pillar and end-plate configurations for the cavity perturbation techniques have been adopted. In the end-plate configuration, the sample was set on the end-plate (Fig. 3-22(a)) and notice that the mode coupling is always H-field coupling. In the pillar configuration, the sample was set in the middle of the cavity using a polyethylene pillar which had been set in the opposite side of the coupling hole (Fig. 3-22(a)). This configuration has a different coupling mode by using different frequency. We have an E-field and H-field couplings when using 58 GHz (TE_{011}) and 72 GHz (TE_{012}), respectively. For the H-field coupling, an induced current rounds the sample (Fig. 3-22(b)). For the E-field coupling, the currents will flow within the plane surface from the sample edges and faces (Fig. 3-22(c)) (See discussion in ref. [68]).

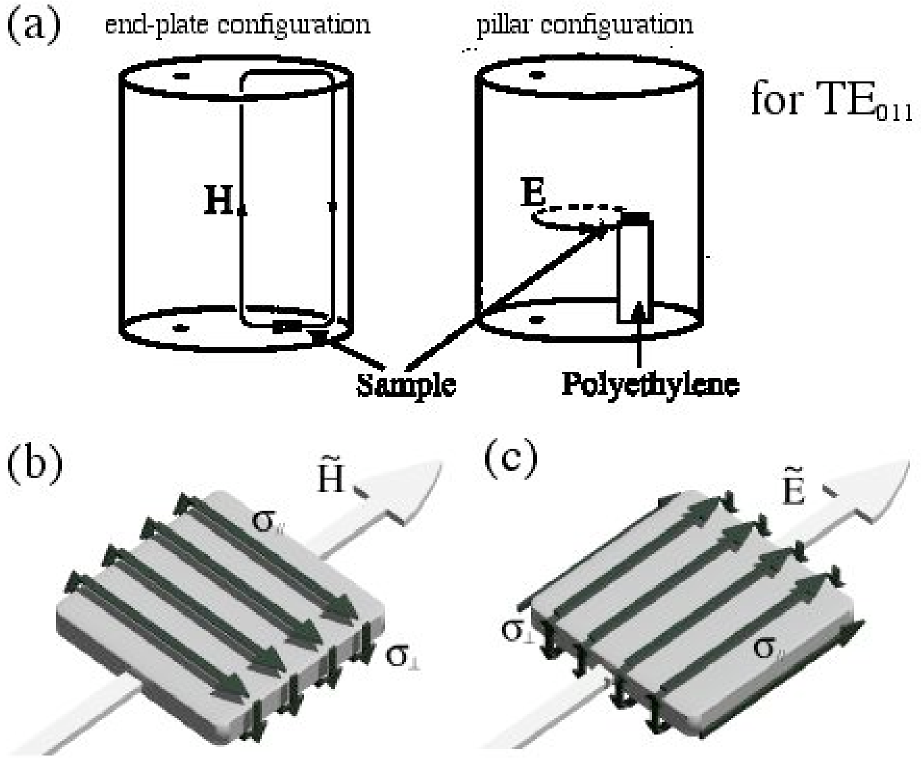

Fig. 3-22 (a) Sample configurations and coupling modes in the cavity (in the case of TE_{011}). (b) Induced current in the case of *H*-field coupling. (c) Induced current in the case of *E*-field coupling.

There are always skin effects in high-frequency measurements for conducting materials. However, the in-plane and interlayer conductivities differ considerably (the interplane conductivity is 3 to 4 orders of magnitude smaller) for organic conductors. Thus, the interplane skin depth ($\delta_{\perp}$) will be larger than the skin depth for in-plane ac currents ($\delta_{//}$). This is why so many papers suggest that the interplane ac magnetoconductivity is mainly probed for this type of measurement [12,15,67,68]. And this suggests that POR which is related to the interlayer conductivity is possible to be observed in cavity perturbation technique. However, in some situations such as a small sample coupled with the oscillatory *E*-field, it is also possible to observe CR which is related to the in-plane conductivity.

4. Quasi-two-dimensional organic conductors

In this chapter, we will present the magnetooptical measurements results of four q2D organic conductors which have simple FS. The first one is θ-(BEDT-TTF)$_2$I$_3$ which has a closed orbit and a magnetic breakdown orbit. The second one is (BEDT-TTF)$_2$Br(DIA) which has only an anisotropic closed orbit. The third and the last one are (BEDT-TTF)$_3$Br(pBIB) and (BEDT-TTF)$_3$Cl(DFBIB), respectively, which have also a closed orbit, but we notice that these are 3:1 compounds and the carrier density is different from other 2:1 salts. Thus, we can examine how carrier density affects the effective mass. These results will be presented in section 4.1, 4.2 and 4.3, and we will show below that the magnetooptical resonance results show a dramatic difference for each sample despite of its simple FS structure. In the latter part, we will discuss about the relation between the skindepth and the observed resonance, and about the scattering time deduced from each resonance linewidth. Finally, the effective mass for each resonance will be discussed.

4.1. θ-(BEDT-TTF)$_2$I$_3$

θ-(BEDT-TTF)$_2$I$_3$ is a q2D organic conductor without any phase transition at low temperatures [29]. We have chosen this sample because the FS shape of θ-(BEDT-TTF)$_2$I$_3$ is well understood by several measurements and it has a simple FS. We have chosen it also for its good residual resistivity ratio (RRR) and the RRR for θ-(BEDT-TTF)$_2$I$_3$ is nearly 1000 [29]. RRR is the resistivity ratio of room temperature and liquid helium temperature; ρ(R.T.)/ρ(4.2K), and it represents the quality of the sample, and a good RRR value signifies that it will satisfy the resonance condition for CR (i.e. $\omega_c\tau>1$). The *ab*-plane is the conducting plane and there are two closed orbits where α and β orbits are attributed to the closed orbit around the zone boundary and the magnetic breakdown orbit, respectively (Fig. 4-1). SdH measurements are already performed by Terashima *et al.* and the obtained effective masses for α and β orbits are 1.8m_e and 3.5m_e, respectively [29]. Moreover, the effective masses obtained from dHvA results are 2.0m_e and 3.6m_e , for each orbit, which are in good agreement with SdH results [34]. The crystals were provided by Dr. Masafumi Tamura (RIKEN) and were prepared by electrochemical crystallization of BEDT-TTF in a tetrahydrofuran solution containing (n-$C_4H_9)_4NI_3$ as a supporting electrolyte [25]. We note that some crystals are twinned and this may yield some ambiguity in the experimental results [25, 27]. We have performed magnetooptical measurements of θ-(BEDT-TTF$)_2I_3$ by using two techniques. One is the transmission technique which has been used for the measurements of α-(BEDT-TTF$)_2$KHg(SCN$)_4$ [9], and the other is the cavity perturbation technique. We will verify if we will have the exact result by using two different techniques and discuss later about the obtained effective masses.

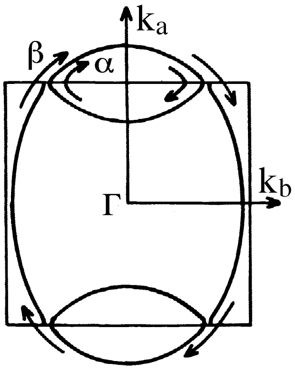

Fig. 4-1 Fermi surface of θ-(BEDT-TTF$)_2I_3$ [29]

-Transmission technique-

We have performed magnetooptical measurements of θ-(BEDT-TTF$)_2I_3$ at 1.8 K using our usual transmission technique (see section 3.4.1) and the pulsed magnetic field up to 15 T. The frequency region used in this measurements were from 40 to 315 GHz.

Figure 4-2 shows the typical spectra of θ-(BEDT-TTF$)_2I_3$ observed at 1.8 K for which the magnetic field is applied perpendicular to the *ab*-plane. CR is expected in this configuration. Only the spectra observed at 120 GHz show the cases where magnetic field is applied perpendicular and parallel to the *ab*-plane. We can clearly see that the resonance diminishes when the field is applied parallel to the *ab*-plane, which indicates the lack of CR in this orientation. We think that the very weak resonance seen in the parallel configuration comes from the resonance of conducting electrons (CER). Therefore, the resonance observed at 120 GHz for perpendicular configuration can be attributed to CR. We have observed two clear absorption lines at 150 and also at 160 GHz. θ-(BEDT-TTF$)_2I_3$ has two closed orbits, α and β, which imply the possibility of observing two CRs. Thus, we can attribute the resonance seen at around 5 T as CR of α-orbit and 13 T as CR of β-orbit. CR from the β-orbit is possibly present for 50 and 105 GHz, but the experimental features are small. However, we have succeeded to observe CR from α-orbit in all performed frequency region.

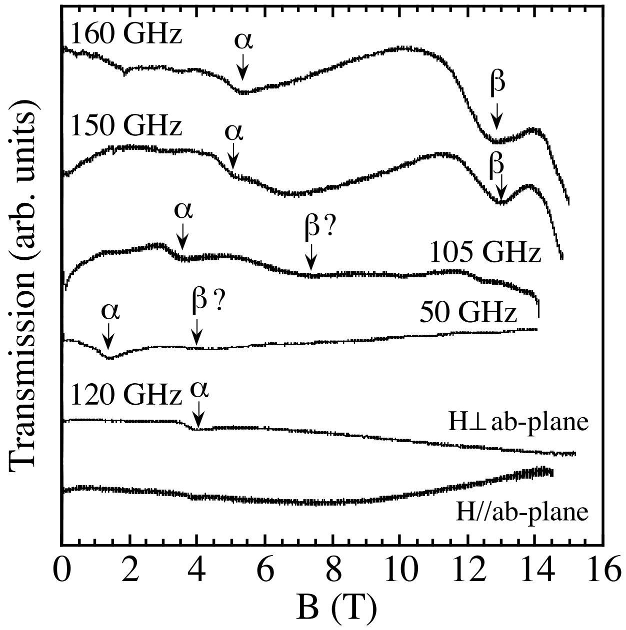

Fig. 4-2 Typical transmission spectra of θ-(BEDT-TTF)$_2$I$_3$ observed at 1.8 K, where the magnetic field is applied perpendicular to the *ab*-plane. Only the 120 GHz results show the comparison between H⊥*ab*-plane and H//*ab*-plane.

-Cavity perturbation technique-

The measurements have been performed in the V- and W-band frequency region using the 14 T superconducting magnet in IMR, Tohoku University [64]. Figure 4-3 shows typical cavity transmission spectra for pillar and end-plate configuration at around 57 GHz (see section 3.4.2 for configuration detail). The magnetic field is applied perpendicular to the *ab*-plane. We have observed one resonance at around 2.2 T for pillar configuration. This resonance was observed at the same resonance position with the transmission technique. However, no resonance was observed in the end-plate configuration. The mode coupling for around 57 GHz in the pillar configuration is the *E*-field coupling which means that the observed resonance is CR. The reason why we did not observe even ESR signal in the end-plate configuration (i.e. *H*-field) is because the ESR linewidth is narrower than the instrumental resolution (=5 mT) [69].

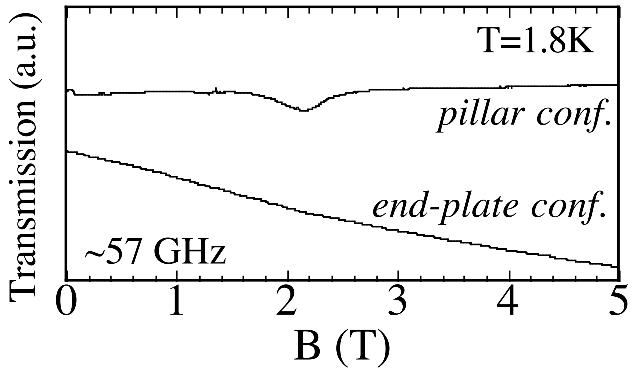

Fig. 4-3 Typical cavity transmission spectra for pillar and end-plate configurations at around 57 GHz and 1.8 K.

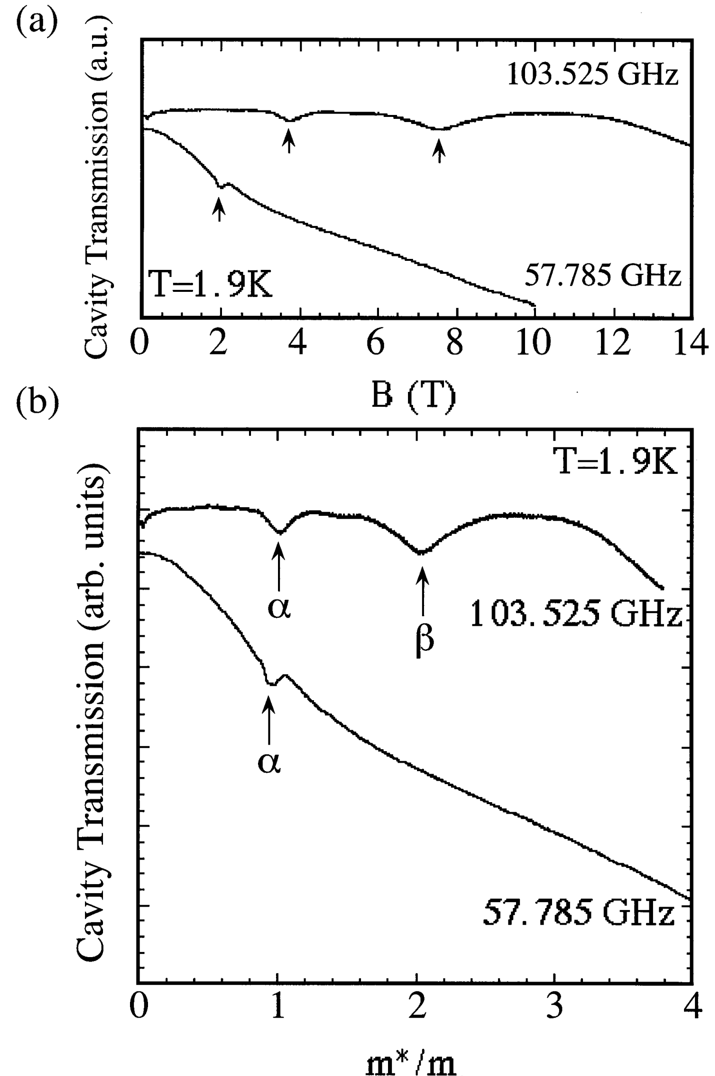

Fig. 4-4 (a) Typical spectra for pillar configuration with different frequencies at 1.9 K. (b) The same spectra with the renormalized x-axis by the effective mass in relative units of free electron mass.

Figure 4-4(a) shows spectra for the same pillar configuration but in higher fields up to 14 T at 1.9 K. We have observed only one CR for 57.8 GHz, however, two CR's absorption lines are observed for 103.5 GHz. Figure 4-4(b) is the same spectra as Fig. 4-4(a), but the x-axis is renormalized by the effective cyclotron mass in relative units of the free electron mass m_e and the effective cyclotron mass is obtained from the well-known equation,

$$m^* = \frac{eB}{2\pi\nu} \quad , \qquad (4.1)$$

where B is the resonance field and ν is the observed frequency. We can see the relation of the absorption lines for each frequency by renormalizing to its effective mass. The CR at $1.0m_e$ is observed for both 57.8 and 103.5 GHz. Despite that no other additional resonance was observed for 57.8 GHz, we have observed an additional absorption line at $2.0m_e$ for 103.5 GHz which suggests that this absorption needs a certain higher magnetic field to appear (i.e. magnetic breakdown orbit). Therefore, the observed CR at around $1.0m_e$ and $2.0m_e$ can be attributed to α and β orbits, respectively. This result is consistent with the measurement using the transmission technique mentioned above. If these resonances are really coming from α and β orbits, which are q2D FS, the resonances' effective mass must have a $1/\cos\theta$ dependence, where θ is the angle between the magnetic field and the c^*-axis. Figure 4-5 shows each effective mass plotted by a function of $1/\cos\theta$ and the inset shows the spectra for $\theta=0°$, $30°$, $60°$.

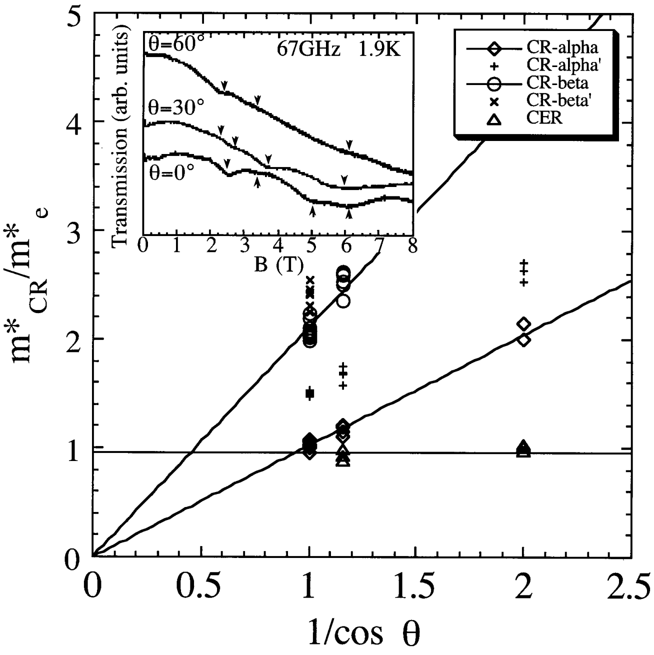

Fig. 4-5 Angular dependence of each resonances' effective mass at 1.9 K. The inset shows the typical transmission for θ=0°, 30°, 60° at 67 GHz.

We note that the sample used for the angular dependence measurements was a twinned crystal. Thus, we can see the splitted resonance in the inset of Fig. 4-5 at θ=0°. The secondary crystal is inclined about 44° from the main crystal from the analysis and the resonance from the secondary crystal is represented by + and x symbols in Fig. 4-5. If we neglect these secondary contributions, CR from the main crystal is fitted linearly and both CRs have a 1/cosθ dependence except for the resonance of the conducting electrons (CER) which is independent of the magnetic field direction. These results suggest that both CRs are coming from the q2D FS (i.e. α and β orbits). We show in Fig. 4-6 the frequency-field diagram of all observed CRs including the measurements using transmission technique [70,71].

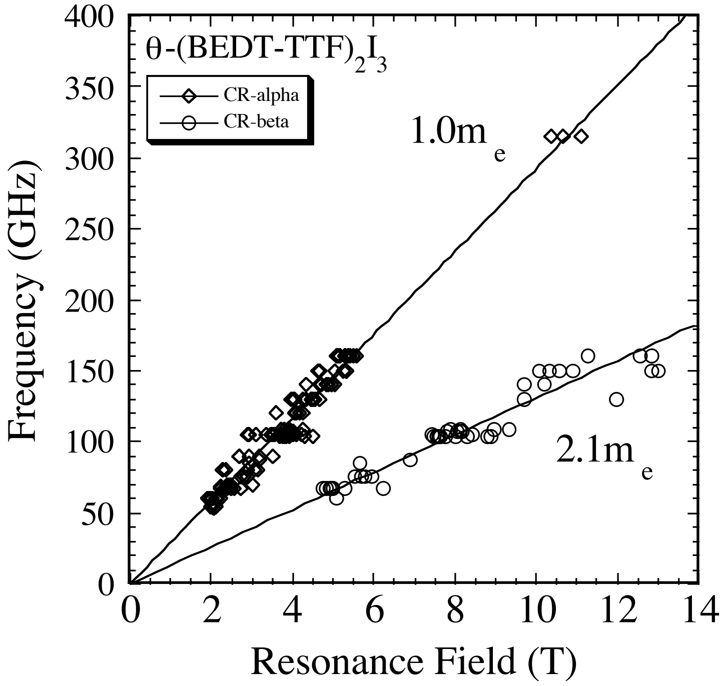

Fig. 4-6 The frequency-field diagram of all observed CRs, where the magnetic field is applied perpendicular to the *ab*-plane.

The solid lines are fitted by eq.(4.1) and the obtained effective masses for α and β orbits correspond to $1.0m_e$ and $2.1m_e$, respectively. The effective masses obtained by dHvA and SdH measurements suggest consistently that β-orbit is about twice the mass of α-orbit [29,34]. Our results suggest also this ratio, but the value is about a half smaller than those obtained by SdH and dHvA measurements. Hence, this difference may be due to the Kohn's theorem, which suggest that the CR's effective mass is independent of the strength of the electron-electron interaction, and this implies that there exists not negligible electron-electron interaction in the system. More precise discussion about the effective mass will be presented in the latter part.

Next, let us direct our attention to the gap related to the magnetic breakdown effect. The breakdown field B_{MB} is related to the energy gap near the junction, E_g, by the equation,

$$B_{MB} = \frac{2\pi m^* E_g^2}{he\varepsilon_F} \quad , \qquad (4.2)$$

where ε_F is the Fermi energy [50]. The breakdown field seems to be around 5 T from our results in Fig. 4-6. If we assume the Fermi energy $\varepsilon_F \sim 0.1$ eV [31,32] and the effective mass $m^* \sim 2m_e$, the energy gap corresponds to $E_g \sim 5.4$ meV which is consistent with the topology of the FS deduced from the tight-binding band model and the dHvA results [34,72]. However, the breakdown field in magnetooptical measurements is much lower than that in SdH measurements, which is around 10 T [29]. The intensity of CR is depending on the scattering time and the carrier density. And it seems that such a high field of 10 T is not required to observe the β orbit in CR measurements due to the high carrier density and longer scattering time in CR for β orbit (see section 4.4).

In summary, we have performed the magnetooptical measurements by using the transmission technique and the cavity perturbation technique. Both results show that the observed absorption lines are CRs which come from the two closed orbits of the q2D FS. CR of α-orbit is observed in all performed frequency region, but CR of β-orbit (magnetic breakdown orbit) requires a certain higher field to observe, which seems to be a very reasonable result. However, the breakdown field in the magnetooptical measurements is much lower than that in quantum oscillation measurements. Obtained effective masses for α and β orbits correspond to $1.0m_e$ and $2.1m_e$, respectively, which are about a half smaller than those obtained by SdH and dHvA measurements. The non-contribution of electron-electron interaction in CR's effective mass (Kohn's theorem) may be the origin of these differences which imply also that there exists not negligible electron-electron interaction in the system.

4.2. (BEDT-TTF)$_2$Br(DIA)

(BEDT-TTF)$_2$Br(DIA) (DIA = diiodoacetylene) is a novel q2D conductor with a very simple FS (Fig. 4-7). It remains metallic down to 0.3 K and RRR is fairly large (about 1500) [38,40]. One of the interesting features of the structure is that the supramolecular ...Br...DIA... chains are formed and the donor molecules (i.e. BEDT-TTF) fit into the channels formed by one dimensional (1D) chains along the *a-c* direction [38]. SdH and ADMRO measurements have already been performed and the results indicate the presence of a q2D FS with an elliptic cross-sectional area and the obtained effective mass is 4.3m_e [40]. The crystals were synthesized and provided by Dr. H. M. Yamamoto (RIKEN) and the typical sample size used for this study was 1x1x0.1 mm^3. The static magnetic field was always applied perpendicular to the conducting plane ($B//b^*$).

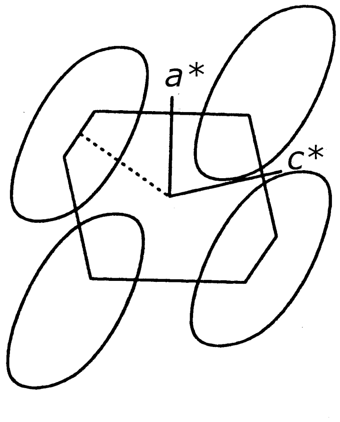

Fig. 4-7 Fermi surface of (BEDT-TTF)$_2$Br(DIA) [38]

Figure 4-8(a) shows typical spectra of (BEDT-TTF)$_2$Br(DIA) observed at 0.5 K in the pillar configuration using several frequencies. This is the same sample configuration when we successfully observed conventional CR in θ-(BEDT-TTF)$_2$I$_3$. At each frequency, we can observe several harmonic absorption lines which become larger as the field increases.

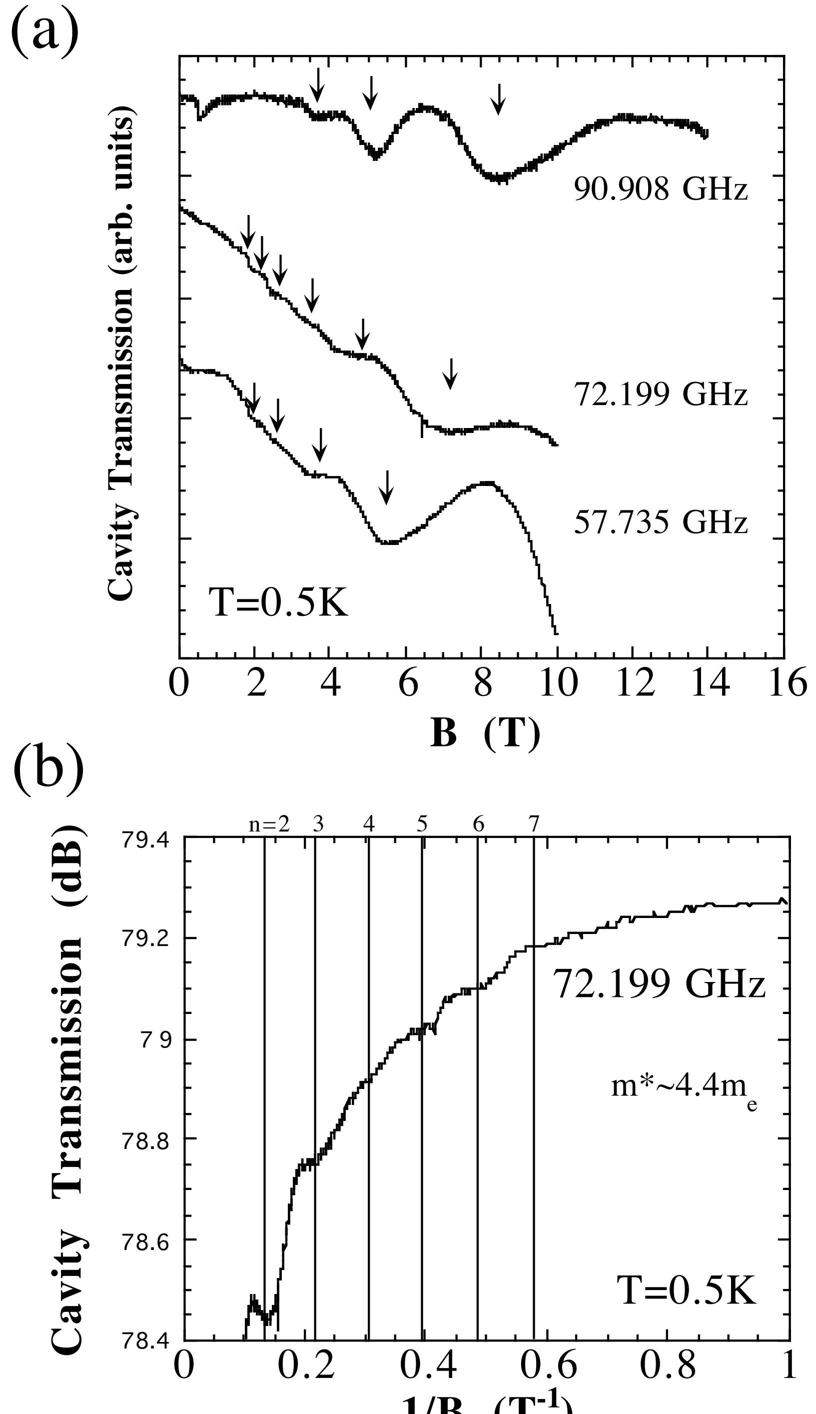

Fig 4-8 (a) Typical cavity transmission spectra of $(BEDT\text{-}TTF)_2Br(DIA)$ observed at 0.5 K in the pillar configuration. (b) The inverse field plot of the spectrum observed at 72 GHz. The lines show the harmonic number.

We show in Fig. 4-8(b), the inverse-field plot of the spectrum observed at 72 GHz. It is clear that the harmonic absorption lines appear periodically as a function of the inverse field. If the resonances are POR, the resonance condition will be $\omega = n\omega_c$, where $\omega_c (= eB/m^*)$ and $\omega (= 2\pi\nu)$ are the cyclotron and microwave frequencies, respectively, which cause nth-order higher harmonics [12]. We point out that these resonances are different from Azbel'-Kaner CR or Gor'kov-Lebed' CR [73,74], because the skin depth of organic conductors (*e.g.* ~65 μm for 60 GHz with σ_{zz}~10^3 S/m) is much larger than the cyclotron radius (*e.g.,* ~1 μm for 60 GHz). From the condition mentioned above, the resonance periodicity against the inverse field should be described as follows.

$$\Delta\left(\frac{1}{B}\right) = \left(\frac{1}{B_{n+1}} - \frac{1}{B_n}\right) = \frac{e}{2\pi\nu m^*} \quad , \qquad (4.3)$$

where B_n is the resonance field of nth-order harmonics and m^* is the cyclotron effective mass. Therefore, from the periodicity of the resonances, which is 0.088 T^{-1} in Fig. 4-8(b), the estimated effective mass would be around $4.4m_e$ by using eq.(4.3). Then, the order of higher harmonics would be given by

$$n = \frac{\omega}{\omega_c} = \frac{2\pi\nu m^*}{eB} \quad . \qquad (4.4)$$

Therefore, Fig. 4-8(b) shows that the strongest absorption corresponds to the second harmonic and we have observed harmonics up to the 7th order (n=1 resonance was not observed in this configuration). We note that this is the first observation of higher order harmonics in the field of organic conductors. We consider that the sample condition (i.e., skin depth, sample size) was appropriate for the observation of higher harmonics. Figure 4-9 shows the temperature dependence (from 0.7 K to 4.2 K) of the spectra observed around 58 GHz in the pillar configuration. The harmonics become more apparent as the temperature decreases. The effective mass estimated from the periodicity at 0.7 K is around $4.6m_e$. We do not think that the broad absorption seen around 13 T at 0.7 K is intrinsic, because the peak disappeared with increasing temperature and n=1 resonance should appear at around 9.5 T. The harmonics up to the 6th order were observed at 58 GHz and the second harmonic still remains as the strongest resonance. Therefore, we conclude that the observed resonances are POR, since the second harmonic is expected to be the strongest for POR [12]. POR is a result of multiple cyclotron-resonance-like features in the conductivity along the least conducting direction [12].

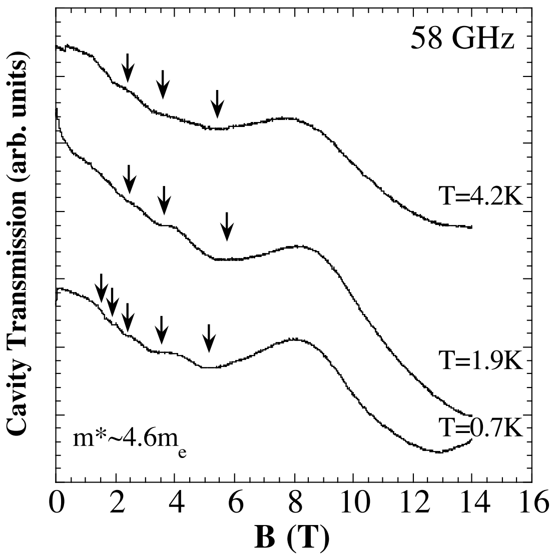

Fig. 4-9 Temperature dependence spectra of $(BEDT\text{-}TTF)_2Br(DIA)$ observed at ~58 GHz.

Thus, the lineshape for POR should be sensitive to the electrodynamics around the sample. However, there is not a significant difference in the lineshapes at 58 GHz and 72 GHz in Fig. 4-8(a), while the induced currents are completely different with different frequencies (i.e., coupling modes for 58 and 72 GHz are E- and H-field, respectively.). This may be due to the ambiguity of the coupling mode when setting the sample in the middle of the cavity. Therefore, to clarify this problem, we performed the measurements in the end-plate configuration whose coupling mode will always be H-field coupling.

Figure 4-10 shows the typical spectra observed at 0.5 K in the end-plate configuration using different frequencies. Each spectrum was normalized so that the horizontal axis corresponds to the cyclotron mass. In general, the H-field coupling mode is the ideal configuration for observing ESR signals. Thus, ESR signals are clearly observed in this configuration, which confirms the ambiguity of the coupling mode in the previous configuration. The strong absorption at $2.7m_e$ corresponds to the second harmonic; the n=1 resonance is observed at around $4.7m_e$, which has not been observed in the pillar configuration. As the linewidth of the second harmonic in the end-plate configuration is larger than that in the pillar configuration, the end-plate configuration shows the characteristic behavior of POR clearer than the pillar configuration, and this can be explain as follows. When the sample is set on the end-plate, the induced current excited from the oscillatory *H*-field rounds the sample surfaces [68]. However, the in-plane conductivity $\sigma_{//}$ and the interlayer conductivity $\sigma_{\perp}$ differ considerably for q2D organic conductor. Thus, the interlayer skin depth will be larger than the in-plane skin depth which means that the interlayer ac magnetoconductivity $\sigma_{\perp}$ is mainly probed for this kind of measurements. This may be the reason why the POR is clearer in the end-plate configuration. Hence, the end-plate configuration is advantageous for POR observation. On the other hand, higher order of harmonics (i.e. 5th, 6th, 7th...) was not observed in the end-plate configuration. The in-plane conductivity in pillar configuration mode might play an important role for observing the higher order of harmonics.

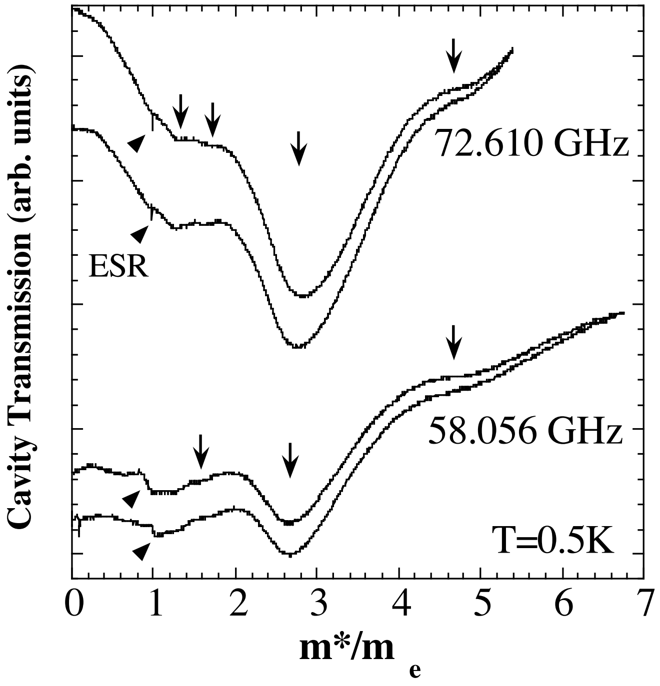

Fig. 4-10 Typical cavity transmission spectra of (BEDT-TTF)$_2$Br(DIA) in the end-plate configuration at 0.5 K (see text for details). The arrows show harmonics and triangles show ESR.

Figure 4-11 is the inverse-field plot of the spectrum shown in Fig. 4-10 (Note that the horizontal axis is normalized by *n*, using the cyclotron mass value estimated by the periodicity of the harmonics, 4.4m_e and 4.8m_e for 58 GHz and 72 GHz, respectively). Due to the difference between the direct cyclotron mass value and the estimated mass from periodicity of the inverse field, there is a slight deviation of the second harmonic in Fig. 4-11.

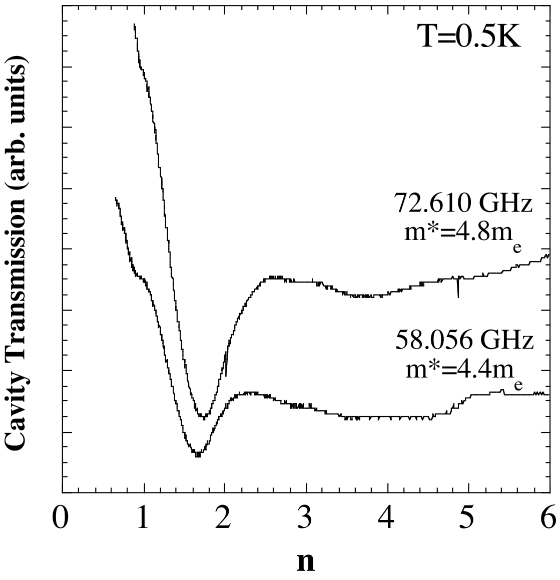

Fig. 4-11 Inverse-field plot of the spectrum shown in Fig. 4-10 (The horizontal axis is normalized by 'n' using the estimated effective mass).

We could not determine whether the *n*=1 resonance is a fundamental POR or a conventional CR. In the pillar configuration (*E*-field coupling), no conventional CR was observed; thus, this may suggest that *n*=1 resonance is a fundamental POR. However, the problem still remains why the fundamental POR was not observed in the pillar configuration. If it is a fundamental POR, the observation of *n*=1 resonance may be due to the slight sample misalignment or a tilting of the FS warping plane away from the conducting plane [12]. The crystal system of this sample is triclinic, thus, it is probable that the FS is tilted slightly. However, the results of both configurations suggest that the second harmonic is dominant, which is the characteristic feature of POR. POR only appears when the FS shape is an anisotropic one, which is in a good agreement with the ADMRO result [40]. On the other hand, the reason why the POR is observed in $(BEDT\text{-}TTF)_2Br(DIA)$ while the conventional CR is observed in $\theta\text{-}(BEDT\text{-}TTF)_2I_3$ is a very interesting problem. The difference in the skin depth and the size of each sample seem likely to be explanations, and we will discuss more precisely about it in section 4.4.

In most organic conductors, smaller effective masses were obtained in the cyclotron resonance experiment than those of SdH and dHvA oscillation measurements. However, for $(BEDT\text{-}TTF)_2Br(DIA)$, the effective mass obtained by

SdH measurement [40], $4.3m_e$, is close to the mass obtained from POR (i.e., ~$4.7m_e$). However, recent POR results also revealed a similar effective mass value with quantum oscillation measurements[14,15], which may suggest that the effective mass is enhanced for POR and is different from the conventional CR masses. We will also discuss about it later in section 4.5.

In summary, we have performed magnetooptical measurements of $(BEDT-TTF)_2Br(DIA)$, and successfully observed POR up to the 7th order which may arise from an elliptic q2D FS. This is the first observation of such a high-ordered harmonic resonance in an organic conductor. The obtained effective mass $4.7m_e$ is consistent with the SdH measurements which may suggest that the effective mass is enhanced for POR and is different from conventional CR masses.

4.3. (BEDT-TTF)$_3$Br(pBIB) and (BEDT-TTF)$_3$Cl(DFBIB)

$(BEDT-TTF)_3Br(pBIB)$ and $(BEDT-TTF)_3Cl(DFBIB)$ are in the same family of $(BEDT-TTF)_2Br(DIA)$ which contains supramolecular assemblies. These supramolecular assemblies formed an 1D chains and the donor molecules (i.e. BEDT-TTF) fit into the channels formed by 1D chains which may suggest the possibility of "fractional band-filling control" by changing 1D supramolecular assemblies with a different period. $(BEDT-TTF)_3Br(pBIB)$ and $(BEDT-TTF)_3Cl(DFBIB)$ are one of these interesting salts which has the 3:1 donor/anion ratio achieved by a longer 1D supramolecular chain period [39]. These salts are the first metallic BEDT-TTF salts where formal charge of donor is +1/3 and the tight-binding calculation shows that the FS is composed of an anisotropic one (Fig. 4-12) [39].

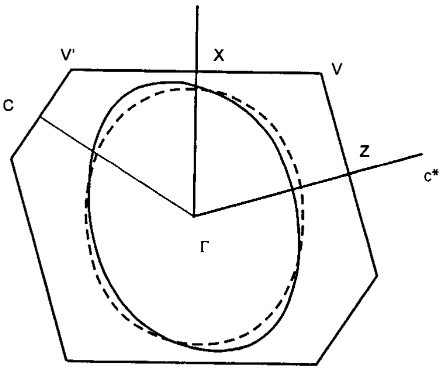

Fig. 4-12 Fermi surface of $(BEDT-TTF)_3Br(pBIB)$ (broken line), $(BEDT-TTF)_3Cl(DFBIB)$ (solid line) [39]

Both salts exhibit metallic behavior down to 1.6 K and RRR is fairly large. However, despite of having almost the same crystal structure, the electrical conductivity of Cl(DFBIB) salt is an order of magnitude lower than Br(pBIB) salt (see section 2.4). The effective masses of Br(pBIB) and Cl(DFBIB) salts are obtained from SdH measurements and correspond to $2.0m_e$ and $2.1m_e$, respectively [42]. However, it is very interesting to perform the magnetooptical measurements in these salts and to investigate how carrier density affects the effective mass compared to 2:1 compounds. The crystals were synthesized and provided by Dr. H. M. Yamamoto (RIKEN) and the typical sample size used for this study was 1x0.2x0.1 mm^3 and 0.5x0.25x0.1 mm^3 for Br(pBIB) and Cl(DFBIB) salt, respectively. The static magnetic field was always applied perpendicular to the conducting plane (*B*//*b**).

Figure 4-13 represents the typical spectra of $(BEDT\text{-}TTF)_3Br(pBIB)$ at 1.4K for 57.2 GHz in the pillar configuration (*E*-field coupling). Only one absorption line is observed at around 2 T and, from the coupling mode of the cavity, this can be assigned to the CR coming from the one and only elliptic q2D FS. However, no signals of POR was observed in the other frequency or sample configuration. The obtained effective mass of $(BEDT\text{-}TTF)_3Br(pBIB)$ is estimated as $1.0m_e$. This value is a half smaller than that obtained from SdH measurements (i.e. $2.0m_e$) [42]. Here again, Kohn's theorem is valid when CR is observed, nevertheless it is a 2:1 compound or 3:1 compound. This may suggest not negligible electron-electron interaction exists in the system.

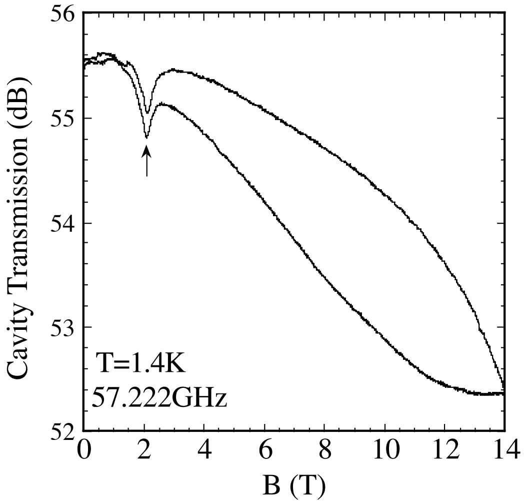

Fig. 4-13 Typical spectra of $(BEDT\text{-}TTF)_3Br(pBIB)$ observed at 1.4 K.

Next, we show the typical spectra of (BEDT-TTF)$_3$Cl(DFBIB) observed at 0.5 and 4.2 K in the pillar configuration (*H*-field coupling for 72 GHz) in Fig. 4-14. The frequency is around 72 GHz and the two spectra at each temperature show upward and downward magnetic field scans. In the spectra of 4.2 K, we see a large gradient due to its magnetoresistivity. However, we see some additional small absorption lines at 0.5 K.

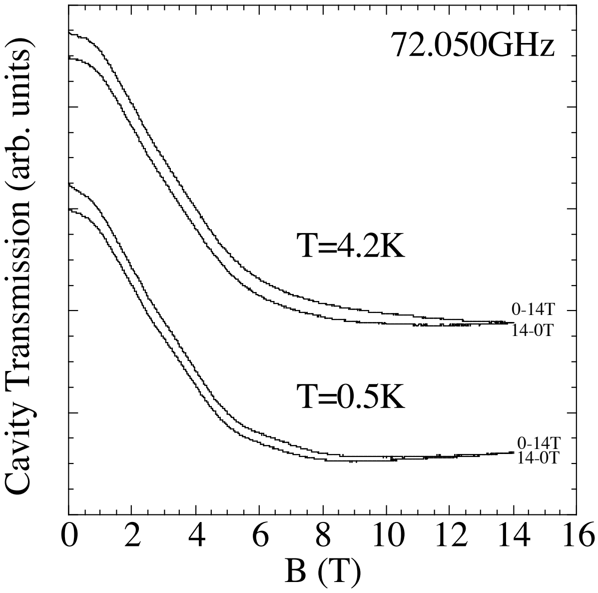

Fig 4-14 Typical spectra of (BEDT-TTF)$_3$Cl(DFBIB) observed at 0.5 and 4.2 K.

To show clearly the additional absorption lines and get rid of the gradient, we have divided several 0.5 K spectra by 4.2 K spectra which are shown in Fig. 4-15. The harmonic absorption lines are clearly seen and the absorption lines are reproduced in each spectrum. The second harmonics are the strongest one which suggests that observed absorption lines are POR [12]. Normally, the fundamental POR (i.e. n=1) cannot be observed when the magnetic field is applied perpendicular to the plane [12]. However, as in the (BEDT-TTF)$_2$Br(DIA) case, we have observed the fundamental POR (n=1 resonance) whose effective mass corresponds to 2.9m_e. The reason why the fundamental POR is observed may be due to the sample misalignment or tilting of FS. The crystal system of (BEDT-TTF)$_3$Cl(DFBIB) is triclinic, thus, it is probable that the FS is tilted.

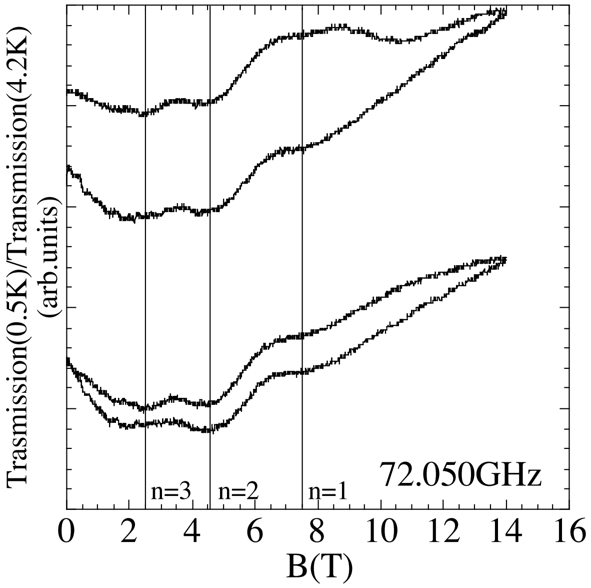

Fig 4-15 The spectra of 0.5 K divided by the 4.2 K spectra.
The vertical solid line shows the number of harmonics.

The observation of POR is in a good agreement with the band calculation and ADMRO results which suggest anisotropic q2D FS [39,42] and obtained effective mass $2.9m_e$ is slightly larger than those of SdH measurements result (i.e. $2.1m_e$). The SdH's effective mass are obtained by fitting the L-K formula to the temperature dependence of the oscillation's amplitude which means that that mass is obtained in a indirectly way and may yield some ambiguity. Therefore, we think that the value of POR's mass $2.9m_e$ and the SdH's mass $2.1m_e$ are more or less consistent as it was for (BEDT-TTF)$_2$Br(DIA). This may suggest, again, that the effective mass is enhanced for POR and is different from the conventional CR's masses. More precise and systematic discussion will be presented later in section 4.5.

In summary, we have performed the magnetooptical measurements of the first metallic 3:1 BEDT-TTF salts, (BEDT-TTF)$_3$Br(pBIB) and (BEDT-TTF)$_3$Cl(DFBIB), and succeeded to observe CR and POR for each salt, respectively. Despite of the fact that both salts have identical crystal structure, it showed a quite interesting difference for each salt. We believe that the reason for observing CR for Br(pBIB) salt and POR for Cl(DFBIB) salt is due to the difference of the dc conductivity (i.e. skindepth). We will discuss about it in the next section. The obtained effective mass is $1.0m_e$ and $2.9m_e$ for Br(pBIB) salt and Cl(DFBIB) salt, respectively, and this results clearly show that Kohn's theorem is valid when CR is observed and the effective mass for POR is enhanced as it was for the (BEDT-TTF)$_2$Br(DIA) case. The discussion of effective mass for CR and POR will be presented in section 4.5.

4.4. CR, POR and resonance linewidths

Table I shows all the presented results with effective masses compared with SdH's effective mass results and the sample's skin depth for interlayer current at 60 GHz. Our presented results show that CRs were observed for θ-(BEDT-TTF)$_2$I$_3$ and (BEDT-TTF)$_3$Br(pBIB) and PORs were observed for (BEDT-TTF)$_2$Br(DIA) and (BEDT-TTF)$_3$Cl(DFBIB). No sample shows the observation of both CR and POR at the same time.

Table I. Our results with effective masses compared with SdH's results and sample's skin depth for interlayer current at 60 GHz, 4.2 K.

	CR	POR	SdH	Skindepth(60GHz)
θ-ET$_2$I$_3$	α:1.0m$_e$ β:2.1m$_e$	No POR	α:1.8m$_e$ β:3.5m$_e$ [29]	40μm
ET$_2$Br(DIA)	No CR	4.7m$_e$	4.3m$_e$ [40]	200μm
ET$_3$Br(pBIB)	1.0m$_e$	No POR	2.0m$_e$ [42]	20μm
ET$_3$Cl(DFBIB)	No CR	2.9m$_e$	2.1m$_e$ [42]	145μm

ET=BEDT-TTF

So the question arises, where these differences are coming from? In principle, POR is based on the q2D FS model [12], so it must be observed in all q2D organic conductor. However, we could not observe POR in some sample and have observed CR instead of POR. This problem is quite interesting and we have to consider the following three situations to explain what is happening, and from that we will show that the anisotropy and the absolute value of the conductivity in q2D organic conductor play an important role for CR/POR observation. We consider the following three situations: (i) *relatively bad q2D conductor* set in the *end-plate configuration*, (ii) *good q2D conductor* set in the *end-plate configuration*, and (iii) *good q2D conductor* set in the *pillar configuration*. In either case, we shall assume that $\omega\tau$>>1 for its good RRR value and we would like to remind that if the sample is set in the end-plate configuration, the mode coupling will be always *H*-field coupling and an induced current rounds the sample (Fig. 4-16). And for the pillar configuration when the coupling mode is *E*-field, the induced current will flow within the plane surface from the sample edges and faces (Fig. 4-17). What we call a *good conductor* is the case of θ-(BEDT-TTF)$_2$I$_3$ and (BEDT-TTF)$_3$Br(pBIB) where the in-plane conductivity is about $\sigma_{//}$~10^5 [S/cm] and a *relatively bad conductor* is the case of (BEDT-TTF)$_2$Br(DIA) and (BEDT-TTF)$_3$Cl(DFBIB) where the in-plane conductivity is about $\sigma_{//}$~10^3 [S/cm].

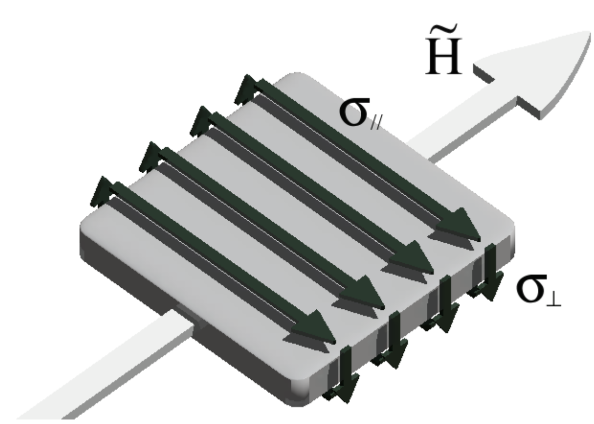

Fig. 4-16 Induced current in the case of *H*-field coupling.

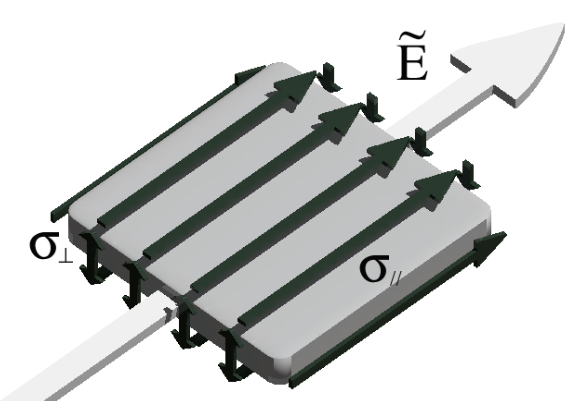

Fig. 4-17 Induced current in the case of *E*-field coupling.

Case (i); Under these conditions, the in-plane skindepth is slightly larger and the interlayer skindepth is much larger than the mean-free path (i.e. $\delta_{//}>\lambda$, $\delta_{\perp}>>\lambda$) where the mean-free path λ is estimated around 1 μm and $\delta_{//}$~5 μm, $\delta_{\perp}>100$ μm [12,68]. This is the condition, which we call "the skindepth regime", where we can adopt the classical skindepth, $\delta = (2/\sigma\omega\mu_0)^{1/2}$. In this case, the amplitude of the cavity transmission is related with the dissipation in the sample which is, in turn, governed by the surface resistance R$_s$, and R$_s$ is proportional to the skindepth [66]. As mentioned above, the in-plane and interlayer conductivities differ considerably for q2D organic conductors (the interlayer conductivity is 3 to 4 orders of magnitude smaller). Thus, the interlayer skindepth $\delta_{\perp}$ will be larger than the in-plane skindepth $\delta_{//}$ and this is why POR, which is related with the interlayer conductivity, will be mainly probed in such a case. Moreover, POR is related to the frequency dependent interlayer conductivity which is proportional to the dc conductivity of the interlayer direction (see eq.(3.52)), therefore, the relatively high resistivity will increase the amplitude of the POR. The elliptic q2D FS will lead to considerable magnetoresistance effect [12] which will also contribute to the POR's amplitude. This suggests that more the FS shape is anisotropic, more you will have the opportunity to observe POR. We have observed POR of (BEDT-TTF)$_2$Br(DIA) and (BEDT-TTF)$_3$Cl(DFBIB), which are in this case.

Case (ii); Under these conditions, the in-plane skindepth is nearly equal or slightly less than the mean-free path λ, and interlayer skindepth is still larger than λ (i.e. $\delta_{//}\sim\lambda$, $\delta_{\perp}>\lambda$). This means that we are on a verge of being in the anomalous skin effect regime in the in-plane direction, but not enough to ignore classical electrodynamic effects where conventional CR observation is still possible. However, the interlayer conductivity is still dominant at this configuration and observation of CR will be difficult unless an extremely thin and large sample is used. On the other hand, POR becomes also difficult to observe, because the interlayer skindepth have decreased an order of magnitude comparing to the *case(i)* (see Table I). This is why POR was not observed for θ-(BEDT-TTF)$_2$I$_3$ and (BEDT-TTF)$_3$Br(pBIB) in the end-plate configuration.

Case (iii); If the coupling mode of the cavity is an *E*-field which is applied correctly parallel to the conducting plane, the induced current will flow within the plane surface from the sample edges and faces (Fig. 4-17). In this case, we don't have to take into account the interlayer conductivity, and in-plane conductivity will mainly probed. Generally speaking, CR is the resonance related with the real part of the in-plane ac conductivity. Therefore, we will have the opportunity of observing conventional CR. This is why CR was observed for θ-(BEDT-TTF)$_2$I$_3$ and (BEDT-TTF)$_3$Br(pBIB).

The three situation mentioned above explain well the reason why we have observed POR for (BEDT-TTF)$_2$Br(DIA) and (BEDT-TTF)$_3$Cl(DFBIB), and CR for θ-(BEDT-TTF)$_2$I$_3$ and (BEDT-TTF)$_3$Br(pBIB). And we conclude that the origin of CR and POR coexist in all q2D conductors, but POR observation is advantageous in q2D conductor due to its anisotropic conductivity. However, we need a q2D conductor which has relatively high resistivity and anisotropic q2D FS to observe clearly the POR. Observation of conventional CR is also possible in some situations. A sample, which has a skindepth between 40-100 μm (e.g. α-(BEDT-TTF)$_2$KHg(SCN)$_4$), might have the opportunity to observe both CR and POR.

Finally, we would like to end this section by discussing the resonance linewidths. The resonance linewidth is governed by the scattering time τ, nevertheless if it is CR or POR. As mentioned in section 3.3., we can use the equation below for the relation between the scattering time τ and the resonance linewidth ΔB,

$$\omega\tau = \frac{2B}{\Delta B} \quad , \qquad (4.5)$$

where ω is the microwave frequency and B is the resonance field. Typical scattering time of θ-(BEDT-TTF)$_2$I$_3$ deduced from the linewidth data indicates the values of $\omega\tau$ between 10-14, i.e. τ~1.5x10^{-11}-3.6x10^{-11} s. This results is an order of magnitude larger than the value obtained by dHvA measurements (i.e. 1.5x10^{-12} and 0.6x10^{-12} s for α and β orbits, respectively) [34]. The scattering time may contain many different contributions, such as impurities, electron-phonon scattering, electron-electron scattering, etc., and the scattering time of CR/POR is not necessarily to be the same with the value of dHvA or SdH. [12, 50] This difference of the scattering time may be the reason why CR/POR is observed at higher temperature and lower magnetic field than the dHvA and SdH measurements. The scattering time shows a considerable sample dependence and frequency dependence (i.e. magnetic field dependence). However, the scattering time τ for θ-(BEDT-TTF)$_2$I$_3$ at 103.5 GHz, 0.5K are 2.0x10^{-11} and 1.7x10^{-11} s for α and β orbits, respectively. (BEDT-TTF)$_3$Br(pBIB), in which CR was observed, had a similar results of 2.7x10^{-11} s at 57.2 GHz, 1.4 K. On the other hand, POR linewidths have the values of $\omega\tau$ between 2-3 which have a shorter scattering time than that of CR; τ~4.6-5.5x10^{-12} s and 5.6x10^{-12} s for (BEDT-TTF)$_2$Br(DIA) and (BEDT-TTF)$_3$Cl(DFBIB), respectively. We note that the linewidths for POR is evaluated from the second harmonics because the n=1 resonance linewidth is not so clear. However, the scattering time for POR is slightly large but similar to SdH results (i.e. τ~1.7x10^{-12} s) [42]. These differences of the scattering time among CR, POR and SdH are very interesting, and these dependence of skindepth and scattering time might be the key for observing CR and POR and even SdH oscillations in magnetooptical measurements.

4.5. CR and POR effective masses

Finally, we will discuss about the effective masses in this section. The effective mass for CRs are around $1.0m_e$ except for the magnetic breakdown orbit (i.e. β orbit) of θ-(BEDT-TTF)$_2$I$_3$ which is $2.1m_e$. However, the CR effective mass is about a half smaller than those of the SdH measurements which suggests the Kohn's theorem is applicable to these salts. Kohn's theorem shows that for an isotropic three dimensional metal the effective mass is independent of electron-electron interaction. However, from our results, it seems that it is also applicable for a two-dimensional system, and from the comparison with SdH results, there exists not negligible electron-electron interaction in the system. If we estimate the contribution of the electron-electron interactions $\lambda_{e\text{-}e}$ by comparing the effective masses obtained from CR and SdH measurements (see section 3.3.2), we have $\lambda_{e\text{-}e} \sim 0.8$ and 0.67 for α and β-orbits of θ-(BEDT-TTF)$_2$I$_3$, respectively, and $\lambda_{e\text{-}e} \sim 1.0$ for (BEDT-TTF)$_3$Br(pBIB). Considering that $\lambda_{e\text{-}e}$ is typically smaller than 0.1 [50], the obtained $\lambda_{e\text{-}e}$ in this study are very large and such a large value of $\lambda_{e\text{-}e}$ is only reported in the layered perovskite superconductors Sr_2RuO_4 where $\lambda_{e\text{-}e}$ is between 0.3~0.5 [60] and in other q2D organic conductors where $\lambda_{e\text{-}e}$ is between 0.6~1.6 [76]. Therefore, the low dimensionality of the system might have increased the electron-electron interactions $\lambda_{e\text{-}e}$ comparing to the conventional metals. However, such a large $\lambda_{e\text{-}e}$ is not observed in semiconductors which have also a 2D electron system and this may be due to the low carrier density. Consequently, the electronic systems for q2D organic conductors are strongly correlated which seem that it is a characteristic behavior of q2D organic conductors.

On the other hand, POR's effective masses are similar with or slightly larger than those of SdH measurements. The Kohn's theorem is based on a three dimensional metal with the ac electric field perpendicular to the magnetic field which can be converted to the in-plane ac conductivity perpendicular to the magnetic field for a two dimensional system (i.e. q2D CR). However, POR is related to the interlayer ac conductivity 'parallel' to the magnetic field as mentioned above. In that case, the Kohn's argument may break down and it is not well understood whether Kohn's theorem is applicable to the interlayer conductivity. Furthermore, Kanki and Yamada have calculated the effects of electron-electron interaction to the cyclotron resonance frequency on the basis of the Fermi liquid theory [59]. They suggest that the cyclotron masses strongly depend on the characteristics of the material (e.g. band-filling, symmetry of the FS) and in some extreme situations such as near half-filling on square lattice, cyclotron effective masses can be comparable to the effective mass obtained by SdH or dHvA measurements. However, they are considering only the CR's case (i.e. in-plane conductivity). Therefore, without further study, it is not clear if it is applicable to the interlayer conductivity. In particular, it is quite possible that the effective mass of POR is enhanced due to the many-body effect in contrary to CR's case. The similarity of the scattering time between POR and SdH suggests also that the POR effective mass may be enhanced. On the other hand, the POR effective mass for (BEDT-TTF)$_2$Br(DIA), which is 4.7m_e, is much larger than the mass for (BEDT-TTF)$_3$Cl(DFBIB) which is 2.9m_e. This difference may be due to the carrier density difference of 2:1 and 3:1 compounds. The carrier density of 3:1 compound is lower than 2:1 compound. Moreover, (BEDT-TTF)$_2$Br(DIA) and (BEDT-TTF)$_3$Cl(DFBIB) are almost in the same family which are BEDT-TTF salts containing supramolecular assemblies. Hence, considering that the electron-phonon interaction is practically the same for both, the difference of the two effective masses may be due to the difference of electron-electron interaction which implies also that the electron-electron interaction contributes to the POR's effective mass. However, we need more detailed discussions and it remains as a subject for the future.

4.6. Conclusion

Magnetooptical measurements of several quasi-two-dimensional (q2D) organic conductors, which have a simple Fermi surface structure, have been performed by using the transmission and cavity perturbation technique. We showed that the mechanisms responsible for the resonant absorption in some q2D organic conductors are quite different from the conventional CR. Observation of CR is advantageous for a parabolic band or isotropic metal. However, POR is favorable for q2D organic conductor due to its anisotropic conductivity. Besides, the selection between POR and CR's observations occur depending on the skindepth of the interlayer current. Therefore, POR was observed for (BEDT-TTF)$_2$Br(DIA) and (BEDT-TTF)$_3$Cl(DFBIB), and CR was observed for θ-(BEDT-TTF)$_2$I$_3$ and (BEDT-TTF)$_3$Br(pBIB). On the other hand, the effective mass and scattering time show also quite interesting results. The effective mass of CR is about a half smaller, and the scattering time is an order of magnitude larger than those obtained from SdH measurements. This difference of the effective mass for CR suggests that Kohn's theorem is valid and not negligible electron-electron interaction exists in the system, and the difference of the scattering time suggests that CR can be observed at higher temperature or lower magnetic field than quantum oscillation measurements. On the other hand, the effective mass and the scattering time of POR are comparable to those obtained from SdH measurements which suggests that POR's effective mass is enhanced due to the many-body effect.

5. Quasi-one-dimensional organic conductors

We have shown in the previous section that the observation of POR and CR are possible in magnetooptical measurements of q2D organic conductors, and the skindepth of the sample plays an important role for probing the resonance. However, most of the organic conductors consist of q2D and q1D FS sheets and soon the question arises whether if the observation of magnetooptical resonance in q1D FS is possible or not. If we look at other measurements, ADMRO is possible for observing both q1D and q2D FS, however, SdH and dHvA oscillations are only possible for q2D FS. Recently, we have several reports of magnetooptical resonance coming from the q1D FS. For example, when a magnetic field is applied in an arbitrary angle parallel to the q1D FS, the carrier trajectories will follow the peaks and troughs of the q1D FS. This results in periodic modulations of the carrier's group velocities and it will contribute resonantly to the ac conductivity at the frequency of its oscillation (see section 3.3.4 for details). Ardavan *et al.* have observed this kind of resonance in α-(BEDT-TTF)$_2$KHg(SCN)$_4$, and have named Fermi traversal resonance (FTR) [13]. Similar interpretation of periodic modulation of carriers is reported elsewhere [12,16,75], including the q1D POR which is the extended version of FTR (see section 3.3.4). Basically, the FTR or q1D POR or high-frequency ADMRO (or whatever you want to call it) is based on the same picture and the name does not matter. Hereafter, we would prefer to call q1D POR in contrast to (q2D) POR which was presented in the previous section. Anyway, the q1D POR was observed in α-(BEDT-TTF)$_2$KHg(SCN)$_4$ which has complex FS and only a few measurements have been done in a simple q1D organic conductor [16]. Therefore, it is worth to conclude this study by performing magnetooptical measurements on an organic conductor which has simple q1D FS and see if q1D POR can be observed in it. In this section, we will present the magnetooptical measurements of (DMET)$_2$I$_3$ and we will show that we have succeeded to observe the q1D POR which are coming from the q1D FS. Fermi velocity and scattering time can be obtained from this novel resonance and these obtained values will be discussed and compared with other measurements results.

5.1. Results of (DMET)$_2$I$_3$

In q1D conductors, the FS consists of a pair of planar sheets. Therefore, the metallic state of q1D conductor can easily become unstable and changes to become insulating due to the good nesting property of the FS. This means that most of the q1D conductors are insulator in the low temperature region which is not usable for studying the FS topologies. Some q1D conductors, such as $(TMTSF)_2ClO_4$, can be in the superconducting state depending on the cooling rate [77] or $(TMTSF)_2PF_6$ which is in the metallic state under pressure [1]. However, we have aimed at $(DMET)_2I_3$ where it shows metallic behavior below 300 K and undergoes a superconducting transition at 0.47 K at ambient pressure [43] without any cooling rate dependence. DMET molecules, where DMET stands for dimethyl(ethylenedithio)diselenadithia-fulvalene, is a non-centrosymmetric molecule which is formed by conjugating half of a TMTSF and half of a BEDT-TTF molecule (*see* Fig. 2-1). As a results, DMET may have intermediate chemical properties between TMTSF and BEDT-TTF. Besides, $(DMET)_2I_3$ is a conducting salt whose crystal structure is characterized by a DMET molecules stack along the *b*-axis and the band structure is considered to have a pair of FS spread along the $k_a k_{c*}$-plane [44]. Hence, $(DMET)_2I_3$ exhibits some behaviors such as Lebed resonance, Danner-Chaikin oscillation and the third angular effect in transport measurements which are related to its q1D electronic band structure [45-48]. We also note that $(DMET)_2I_3$ is known for the first observation of the third angular effect in ADMRO. The sample was synthesized and provided by Dr. Hiroyuki Nishikawa (Tokyo Metropolitan University) and the typical sample size used in this measurements was 2x1x0.1 mm^3. We have performed magnetooptical measurements of $(DMET)_2I_3$ with several magnetic field direction.

First, we have set the sample in the pillar configuration such as the oscillatory *E*-field and the static magnetic field is applied along the *b*-axis and *c**-axis, respectively. This is the best suggested sample position for observing Gor'kov-Lebed' CR [74]. Gor'kov-Lebed CR is what is called as the Azbel'-Kaner CR for q1D conductors and is different with the q1D POR. If we apply the magnetic field parallel to the q1D FS and the oscillatory *E*-field to the conducting axis, the carrier will take a sinusoidal motion along the conducting axis, and when the amplitude of the sinusoidal motion is much larger than the skindepth of the sample, the carrier will periodically penetrate into the skin layer to pick up the energy from the alternating electric field. This will cause a Azbel'-Kaner type CR for q1D FS and the resonance condition will be $\omega = n\omega_c$ where ω and ω_c are the experimental frequency and the periodic orbit frequency of this sinusoidal motion, respectively [74]. Figure

5-1 represents the typical cavity transmission spectra for this configuration.

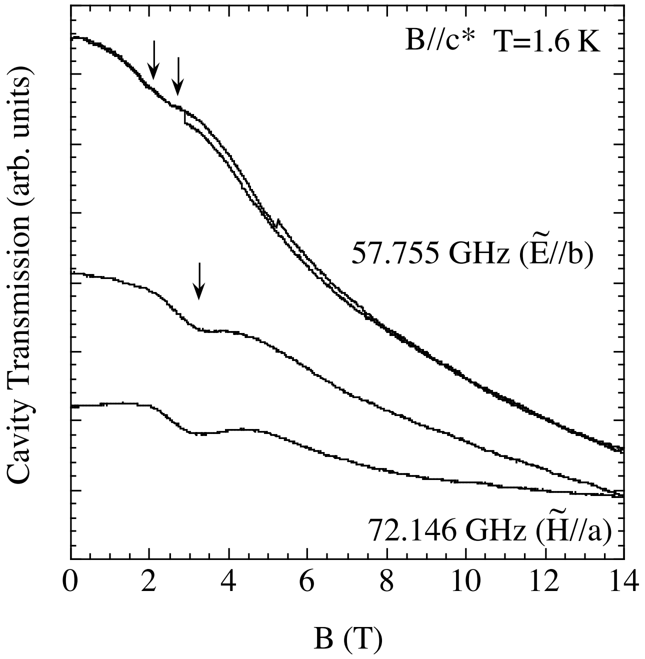

Fig. 5-1 Typical transmission spectra of $(DMET)_2I_3$ observed at 1.6 K for the pillar configuration. The oscillatory *E*-field and *H*-field is applied along the *b*-axis for 58 GHz and *a*-axis for 72 GHz, respectively.

We have observed some absorption lines around 2.5 T for the spectra of 57.8 GHz where the oscillatory *E*-field is applied along the *b*-axis. However, these absorption lines do not show a harmonic behavior and do not satisfy the resonance condition for Gor'kov-Lebed' CR (i.e. $\omega = n\omega_c$). We have also observed a larger absorption line for 72.1 GHz. When the frequency is at around 72 GHz, the oscillatory *H*-field is applied along the *a*-axis and this induces current which rounds the sample. Therefore, the induced current has the possibility of flowing along the *b*-axis which is identical with applying *E*-field along the *b*-axis and it might be possible to observe Gor'kov-Lebed' CR. However, this absorption did not show also any harmonic resonance which means that the absorption seen in both frequencies is not Gor'kov-Lebed' CR. The reason why we did not observed Gor'kov-Lebed' CR is quite simple. The interlayer skindepth of this sample is relatively large and the amplitude of sinusoidal motion could not exceed the skindepth where it does not satisfy the resonance condition for Gor'kov-Lebed' CR [74]. We will discuss about it precisely in the following section. However, what are these absorption lines? It seems that the absorption is larger for *H*-field coupling as shown in Fig. 5-1. Therefore, it is better to perform measurements in the end-plate configuration where the coupling mode is always *H*-field. Moreover, to study the origin of this resonance, we must apply the magnetic field in various direction. So it is more convenient to set the sample in the end-plate configuration, because we have to incline the sample with accuracy. Thus, we have performed magnetooptical measurements of $(DMET)_2I_3$ by applying the magnetic field in various direction in the end-plate configuration. The magnetic field direction is represented by the angle θ and ψ, where θ is the angle from *c**-axis to *ab*-plane and ψ is the angle from *a* to *b*-axis. The conducting axis is the *b*-axis (see Fig. 5-2).

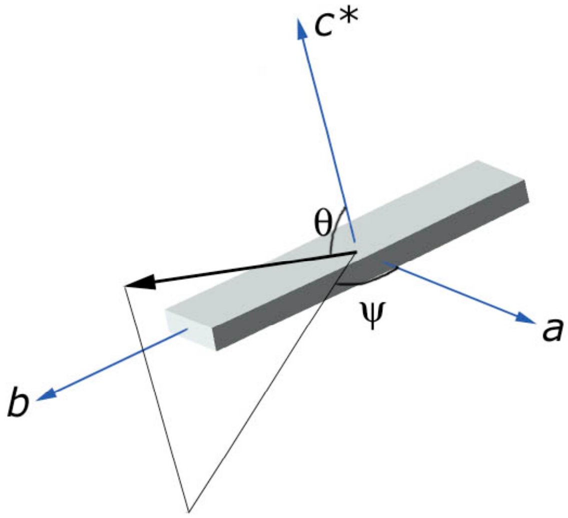

Fig. 5-2 Schematic example of magnetic field direction applied on the sample.

Figure 5-3 shows the typical cavity transmission spectra observed at 1.6 K where the magnetic field is applied along the *c**-axis. We have chosen this configuration first, because it is the easiest position to set. The oscillatory *H*-field is applied along the *b*-axis. In Fig. 5-3, we have observed a broad absorption line for each frequency where the resonance field is proportional to the frequency. These results show the evidence that the broad absorption line is a resonant absorption. Figure 5-4 is the typical cavity transmission spectra observed at 1.5 K where the magnetic field is applied along the *a*-axis. The oscillatory *H*-field is applied along the *b*-axis. A large absorption in the high field region and a small absorption in the lower field region have been observed for each frequency. As it can be seen from Fig. 5-3, the resonance field of the absorption lines in Fig. 5-4 is proportional to the frequency. However, comparing the resonance shape of *B*//*c**-axis in Fig. 5-3, which looks like a shoulder, the resonance shape for *a*-axis in Fig. 5-4 is composed of a Lorentz-type and a shoulder type one. And, for *B*//*a* (Fig. 5-4), it looks like that the small absorption is a harmonic resonance of the large absorption. Therefore, it seems that we have also observed the harmonic resonance in the *B*//*c** case (Fig. 5-3) and the main resonance should exist above 14 T.

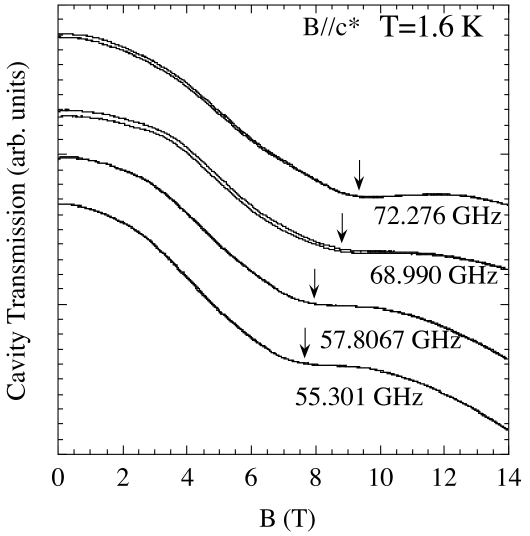

Fig. 5-3 Typical cavity transmission spectra observed at 1.6 K when the magnetic field is applied along the *c**-axis.

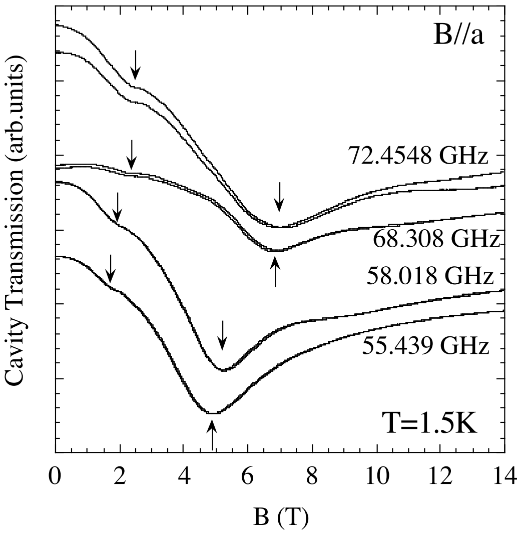

Fig. 5-4 Typical cavity transmission spectra observed at 1.5 K when the magnetic field is applied along the *a*-axis.

We have seen above the frequency dependence of typical spectra for *B*//*a* and *c**-axes. Now, we will look into the angular dependence for a fixed frequency and see how these absorption lines behave.

Figure 5-5 shows the angular dependence of cavity transmission spectra where the magnetic field is rotated from *a*-axis (ψ=0°) to *b*-axis (ψ=90°). Both resonances seen for *B*//*a*-axis shift to higher field as the angle increases, but disappear at ψ=60°, 90°. These resonances have a 1/cosψ dependence as seen in Fig. 5-6 which means that the resonances strongly depend on the magnetic field component parallel to the q1D FS (i.e. k_ak_{c*}-plane). We note that the magnetic field direction, where the resonances disappeared, is almost the same direction where the third angular effect is observed in ADMRO [48]. This suggests that the resonances disappear when the closed cyclotron orbits appear in the q1D FS. Therefore, we believe that these resonances are coming from the warped q1D FS and the quasi-particles trajectories must cross the Brillouin zone to observe these resonances. More detailed discussion is done in the next section.

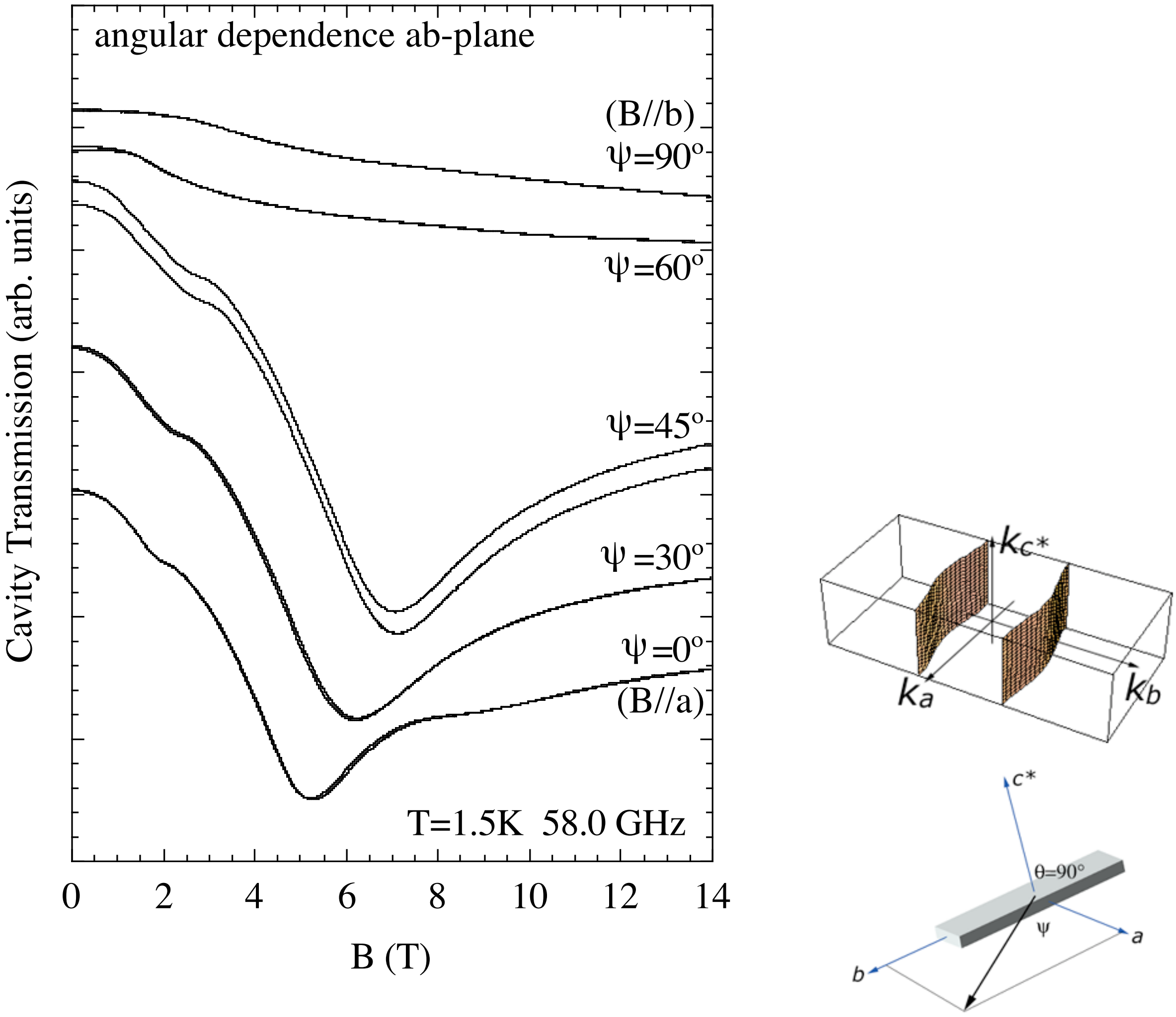

Fig. 5-5 Angular dependence of cavity transmission spectra observed at 1.5 K for 58 GHz where the magnetic field is rotated from *a* to *b*-axis.

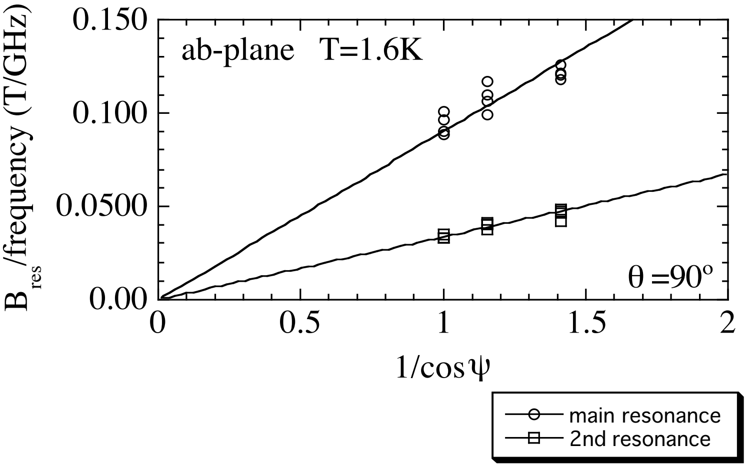

Fig. 5-6 Angular dependence of the resonance field divided by its observed frequency.

Figure 5-7 shows angular dependence of typical cavity transmission spectra observed at 1.6 K for 57 GHz where the magnetic field is now rotated from the *c**-axis (θ=0°) to the *b*-axis (θ=90°). Contrary to the above case, the observed absorption in Fig. 5-7 is not so clear. The reason of this result is explained as follows. Due to the sample configuration restriction, the oscillatory *H*-field is applied along the *a*-axis in this case. If we apply the oscillatory *H*-field along the *a*-axis, the induced current will round the sample in the direction parallel to the *b* and *c**-axes. As it was for the q2D case, the magnetooptical absorption is governed by the electrodynamics of the sample and the amplitude is proportional to the product of the skindepth and the surface area where the current flow. Therefore, when the current flows in the *b*-axis direction which is the most conducting axis, the skindepth is very small. Moreover, for the current which flows parallel to the *c**-axis, the skindepth is large but the sample surface area is too small to gain the amplitude. So the observation of the *bc**-plane is difficult in this sample configuration and we need a rotational cavity system for this kind of study which remains as a subject for the future.

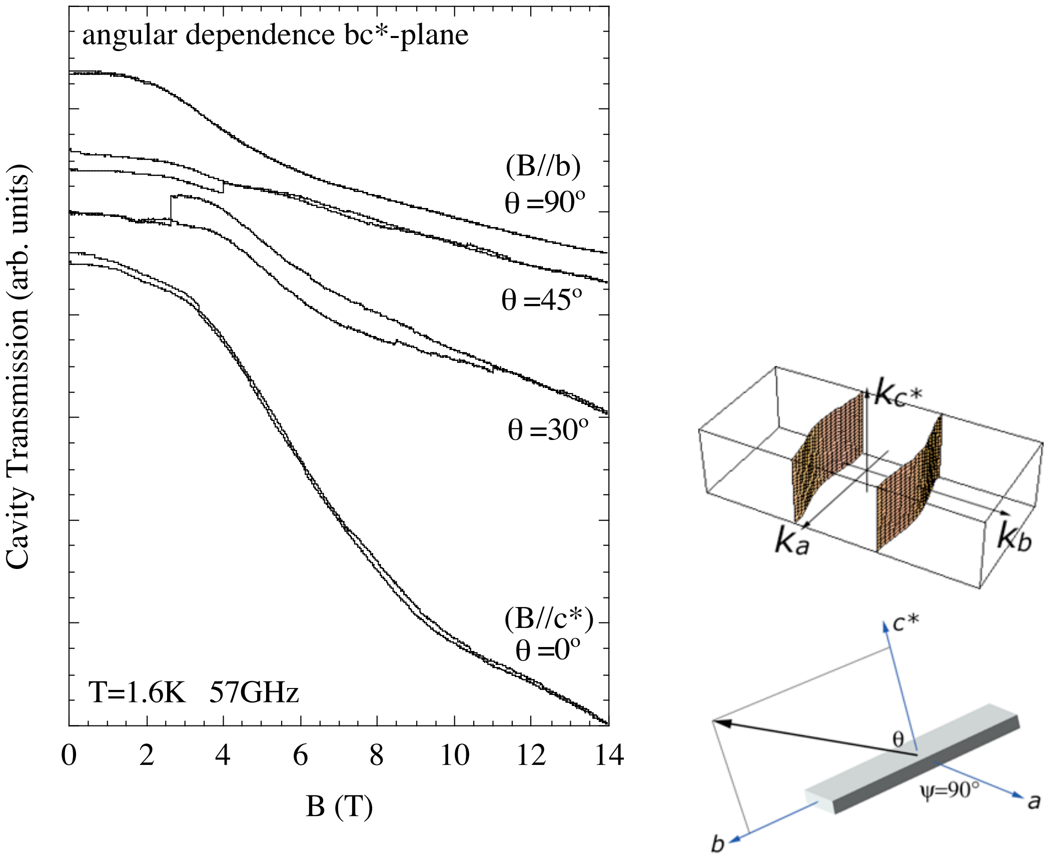

Fig. 5-7 Angular dependence of cavity transmission spectra observed at 1.6 K for 57 GHz when the magnetic field is rotated from *c** to *b*-axis.

Finally, we show the angular dependence of typical cavity transmission spectra observed at 1.6 K for 58 GHz in the *ac**-plane in Fig. 5-8. This measurement is interesting to observe because the magnetic field direction is parallel to the FS. The oscillatory *H*-field was always applied to the *b*-axis in this case. In Fig. 5-8, we see a quite interesting structure of the spectra where the two absorption lines seen in the *a*-axis (θ=90°) shift to higher field as we incline to the *c**-axis (θ=0°) and some additional absorption is observed at θ=60°. The absorption lines seem to come back to the lower field when the angle θ is negative. These absorption lines show a characteristic resonance shift which is completely different from the one seen in q2D FS (i.e. 1/cosθ dependence). Moreover, these absorption lines do not appear periodically as a function of the inverse-field as it was observed in q2D POR (see section 4.2). This confirms that the band structure is not q2D but q1D. We point out also that the resonance position is not symmetrical with the angle (i.e. negative angle has a different spectrum). This is related with the crystal structure of the sample, and we will discuss about this later in the next section.

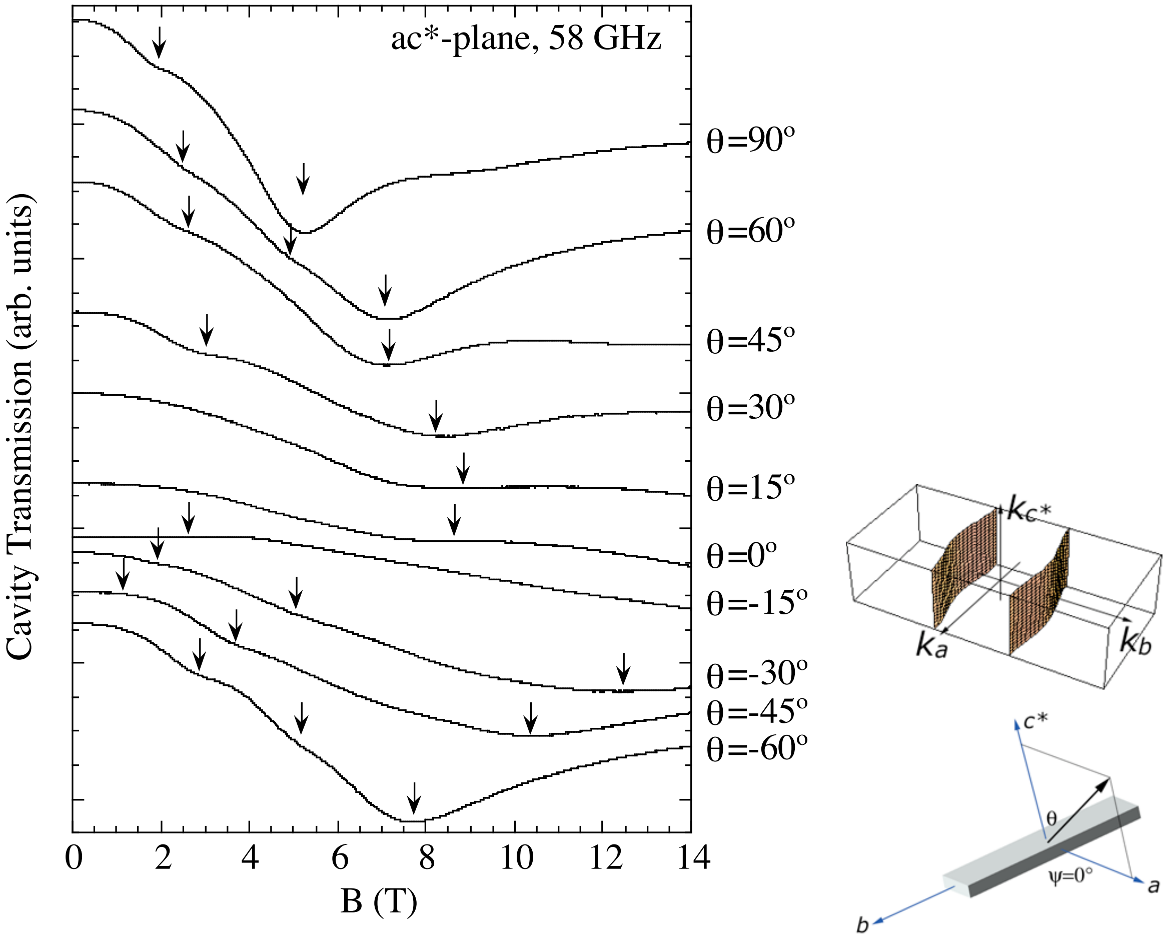

Fig. 5-8 Angular dependence of cavity transmission spectra observed at 1.6 K for 58 GHz when the magnetic field is rotated in the *ac**-plane.

Now, let us plot the resonance position versus its angle in Fig. 5-9. The resonance position is represented by the value of observed frequency divided by the resonance field. The largest Lorentz-type absorption is represented by the circle and the second largest shoulder-type absorption which is thought to be a harmonic resonance is represented by the square. Other additional absorption is represented by other symbols. We note that the error bars for harmonic resonance (2nd and Extra in Fig. 5-9) is larger than the main resonance because the value is represented by ν/B (i.e. inverse field) and resonance below ν/B~4 could not be observed due to the instrument restriction (i.e. frequency above 55 GHz and magnetic field up to 14 T). We have arbitrary fit the plot by the sinusoidal curve and it seems to fit well with it. As it was explain in section 3.3.4, the q1D POR can be fit with sinusoidal curve which means the observed resonance is possibly q1D POR. However, we note that these two fitted curves have different amplitude (about the triple) and this reason will be explain in the next section. Other harmonic contents could not be fit due to the lack of data. However, we will try to consider the origin of these extra resonances in the next section.

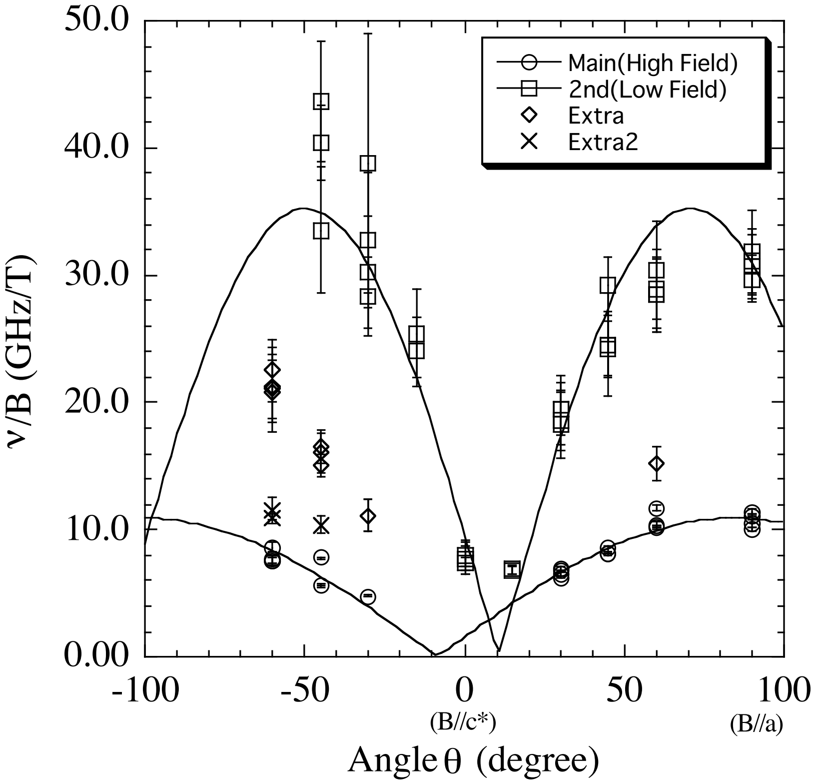

Fig. 5-9 The angle dependence plot of the resonance position. The resonance position is represented by the value of observed frequency divided by the resonance field. The solid line is fitted by an arbitrary sinusoidal curve.

In summary, we have performed the magnetooptical measurements of q1D organic conductor (DMET)$_2$I$_3$, and have succeeded in observing the resonance coming from its q1D FS. The angular dependence of the resonance seems to show a characteristic behavior of q1D POR. However, no other resonances, such as Gor'kov-Lebed' CR, have been observed. More precise discussion of the results will be presented in the next section.

5.2. Discussion

In this section, we will discuss more precisely on the results we have obtained. In the first part, we will discuss about the skindepth and the observed resonance where we will explain why Gor'kov-Lebed' CR could not be observed and why there is a directional dependence of oscillatory *H*-field. Next, we will analyze the observed resonance and conclude that we have observed q1D POR coming from a quite corrugated q1D FS. And finally, we will discuss about the obtained Fermi velocity and scattering time.

-The skindepth and the observed resonance-

First, we will discuss about the skindepth and the observed resonance. (DMET)$_2$I$_3$ is a q1D organic conductor which signify that the conductivity is different for each axis and, of course, the skindepth will be also different for each axis. The dc conductivity ratio for each axis is σ_b:σ_a:σ_{c*}=6000:600:1 [45]. The conductivity of *b*-axis at 4.2 K is around 0.2x10^6 Scm^{-1} [43] and the skindepth for each axis has a estimated value of δ_b=0.46, δ_a=1.45 and δ_{c*}=35.6 μm for 60 GHz. As it was for the q2D case, the skindepth for interlayer current (i.e. δ_{c*}) is absolutely larger than others which suggests that the interlayer ac conductivity will be mainly probed in magnetooptical measurements. As mentioned earlier, if we apply the static magnetic field parallel to the q1D FS and the oscillatory *E*-field to the conducting axis, the carrier will take a sinusoidal motion along the conducting axis where the amplitude of sinusoidal motion can be written as follows,

$$X_a = \frac{2t_a c}{ev_F B}, \quad (5.1)$$

where t_a is the transfer integral along the a-axis, v_F and B is the Fermi velocity and the applied magnetic field, respectively [74]. We note that the eq.(5.1) is written in CGS unit and c represents the speed of light. If we roughly estimate the amplitude of the motion by introducing t_a~0.3 eV, v_F~3.0x10^6 cm/s and B~2 T, we obtain the amplitude X_a~10 μm. This value is obviously smaller than the value of the interlayer skindepth δ_{c*} which means that the carrier can not periodically penetrate into the skin layer and it does not satisfy the condition for observing Gor'kov-Lebed CR (i.e. $X_a >> \delta_{c*}$). That is why we could not observe Gor'kov-Lebed CR in Fig. 5-1. Furthermore, in the measurements of the angular dependence, we could not have good results in the bc*-plane (Fig. 5-7) and this can be also explained by considering the skindepth. We stress that the magnetooptical absorption is governed by the electrodynamics of the sample and the relative contributions of the dissipation is proportional to the product of skindepth and surface area where the current flows. Therefore, we can evaluate the ratio of the dissipation in the case when the oscillatory H-field is applied along the b and a-axes. All we have to consider is the skindepth and the surface area where the induced current will flow according to the applied oscillatory H-field. For example, if the oscillatory H-field is applied along the b-axis, the induced current will flow and round the surface to the direction perpendicular to the b-axis. Therefore, the power dissipation $P_{//b}$ can be written as

$$P_{//b} \propto 2d_a d_b \delta_{//a} + 2d_b d_c \delta_\perp = 2d_b \sqrt{\frac{2}{\omega\mu_0}} \left(\frac{d_a}{\sqrt{\sigma_a}} + \frac{d_c}{\sqrt{\sigma_{c*}}} \right), \qquad (5.2)$$

where d_a, d_b, d_c is the sample dimension for each axis and ω is the angular frequency of oscillatory H-field. The power dissipation $P_{//a}$ when the oscillatory H-field is applied along the a-axis can be written in the same way as

$$P_{//a} \propto 2d_a d_b \delta_{//b} + 2d_a d_c \delta_\perp = 2d_a \sqrt{\frac{2}{\omega\mu_0}} \left(\frac{d_b}{\sqrt{\sigma_b}} + \frac{d_c}{\sqrt{\sigma_{c*}}} \right). \qquad (5.3)$$

Hence, the ratio of the power dissipation in the case when the oscillatory H-field is applied along the b and a-axes will be $P_{//b}/P_{//a}$ ~2.2 by using eqs.(5.2) and (5.3) and the value of sample dimension (2x1x0.1) and the conductivity. This suggests that we will have a better resonant absorption when the oscillatory H-field is applied along the b-axis (conducting axis) and this is the reason why we could not have good results in the angular dependence of the bc*-plane (Fig. 5-7) where oscillatory H-field is applied along the a-axis. However, it is geometrically impossible to measure the angular dependence of the *bc**-plane by fixing the oscillatory *H*-field to the *b*-axis in our actual measurement system. To do this, we need a rotational cavity system and this remains as a subject for the future. Hence, we would like hereafter to focus on the results of *ab*-plane (Fig. 5-5) and *ac**-plane (Fig. 5-8).

-Analysis of the observed resonance-

We have shown in Fig. 5-6 that the observed resonance B_{res} divided by the observed frequency have a $1/\cos\psi$ dependence in the *ab*-plane (Fig. 5-5). This suggests that the resonance is related to the static magnetic field component parallel to the q1D FS, $B_{res}\cos\psi$, and the resonance is coming from the q1D FS. However, the resonance completely disappear when the angle ψ is larger than 60° and this phenomenon is quite interesting. As mentioned in section 3.2, there are three angular effect for ADMRO measurements. One is the Lebed resonance when we rotated the magnetic field parallel to the q1D FS, the second one is the 2nd angular effect known as Danner-Chaikin oscillation when the field is rotated from the least conducting axis to the most conducting axis, and the last one is the third angular effect when the field is rotated from the second most conducting axis to the most conducting axis. Therefore, rotating the magnetic field in the *ab*-plane for $(DMET)_2I_3$ is the identical rotation where the third angular effect must be observed. In fact, the third angular effect, corresponding to the kink and peaks around the *b*-axis (conducting axis) in the magnetoresistance measurement, has been observed as shown in Fig. 5-10 [45,48]. We note that the angle ϕ in Fig. 5-10 is defined to zero when the magnetic field is applied to *b*-axis and the relation with ψ is $\psi=90^\circ-\phi$. The third angular effect originates from the appearance or vanishing of closed orbits on the sheet-like FS when the magnetic field is rotated in the most conducting plane and this leads to a kink structure in the angle dependence of magnetoresistance. The closed orbits enhance the magnetoresistance because the carrier velocity along the k_z-axis (i.e. *c**-axis) is averaged to zero and a peak in the magnetoresistance should be observed around the conducting axis [57]. However, three peaks have been observed above 10 T for $(DMET)_2I_3$ which is a quite particular behavior comparing to other q1D organic conductor.

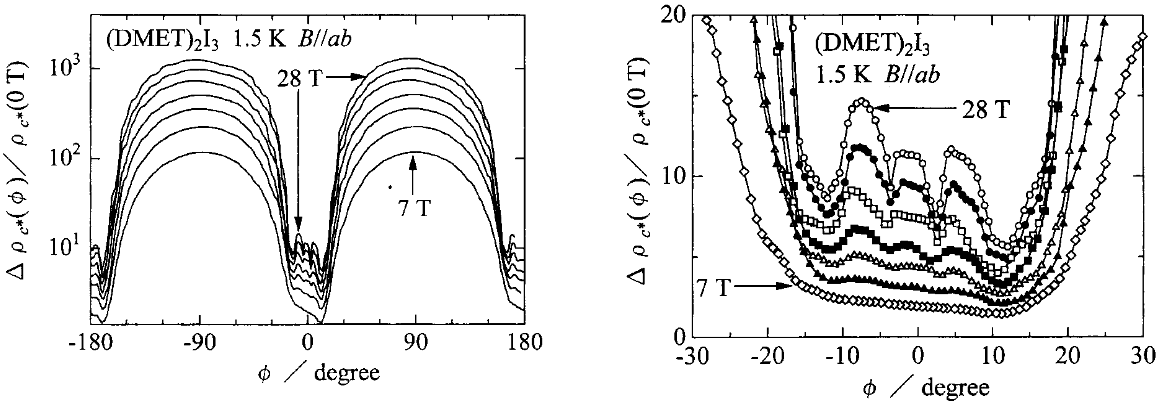

Fig. 5-10 Magnetic field orientation dependence of normalized magnetoresistance of $(DMET)_2I_3$ observed at 1.5 K from 7 to 28T within the *ab*-plane. The angle ϕ is defined to zero when the magnetic field is parallel to the most conducting *b*-axis. [48]

Anyway, the disappearance of the magnetooptical resonance at $\psi=60^\circ$ seems to correspond with the sharp drop of the magnetoresistance around $\phi=30^\circ$ and seems to be related with the appearance of closed orbits on the q1D FS. If the observed magnetooptical resonance is q1D POR, the reason why it disappears above $\psi=60^\circ$ can be explain as follows. The q1D POR is a resonant absorption of interlayer ac conductivity which is related to the periodic modulation of carrier's group velocity when the carrier trajectories follows the peaks and troughs of the q1D FS and the resonant absorption occurs when the frequency of the periodic modulation matches with the observed frequency. When the magnetic field is rotated from the *a*-axis to *b*-axis (ψ increases), the closed orbits appear and open orbits begin to decrease above the critical angle ψ_c. It is clear that the periodic modulation of a closed orbit and an open orbit will not be the same. This means that the amplitude of q1D POR decreases considerably when the closed orbits appear above ψ_c. Moreover, the sharp drop of the magnetoresistance in Fig. 5-10 will also lead to the decrease of the q1D POR's amplitude. Therefore, we think that the sudden disappearance of the resonance is due to the appearance of closed orbits in q1D FS and the sharp drop of the magnetoresistance. The critical angle ψ_c can be obtain from the FS topology and is given by

$$\tan(90^\circ-\psi_c) = \tan\phi_c = \frac{2t_a a}{\hbar v_F}. \qquad (5.4)$$

Here v_F is the Fermi velocity, t_a and a is the transfer integral and the lattice constant of $(DMET)_2I_3$ for *a*-axis (2nd most conducting axis), respectively. If a quarter of the band is occupied, eq.(5.4) becomes

$$\tan(90^\circ - \psi_c) = \tan\phi_c = \sqrt{2}\,\frac{t_a a}{t_b b}, \qquad (5.5)$$

since $v_F = \sqrt{2} t_b b / \hbar$ and t_b and b is the transfer integral and the lattice constant of $(DMET)_2I_3$ for *b*-axis (most conducting axis). We note that the notation *a* and *b* will be inverted for other salts such as $(TMTSF)_2ClO_4$ or $(TMTSF)_2PF_6$ where the *a*- and *b*-axis is the most and 2nd most conducting axis, respectively. Therefore, we can roughly estimate t_a/t_b of $(DMET)_2I_3$ from the critical angle. The magnetooptical resonance disappear at the angle of ϕ=30° (i.e. ψ=60°) and the kink in the magnetoresistance is observed at ϕ=12°. However, it is known theoretically that the critical angle ϕ_c do not correspond to the kink angle but to the angle below which the angular magnetoresistance derives from the monotonous dependence [57] and it is also difficult to define the critical angle from our results because of the sharp drop of the magnetoresistance will cause the decrease of resonance's amplitude. However, if we take the critical angle to ϕ_c=21°, which lies between ϕ=12° and 30°, we have t_a/t_b~0.31 which is in a good agreement with the conductivity results, $\sigma_b:\sigma_a=(t_b)^2:(t_a)^2$=10:1 [45]. Therefore, this explains well the physical background of what is happening when the field is rotated in the *ab*-plane, and the observed resonance is probably the q1D POR where the carriers' trajectories, which is perpendicular to the applied magnetic field and parallel to the q1D FS sheets, need to be opened (it must cross the Brillouin zone).

Now, let us discuss about the results of the *ac**-plane. We have shown above that the observed resonance might be a q1D POR and we would like to remind that the q1D POR's resonance conditions for $(DMET)_2I_3$ can be written as follows,

$$\frac{\nu}{B_{res}} = \frac{e v_F}{h}\left[(nc^*)^2\cos^2\psi + (ma' + na'')^2\right]^{1/2}\left|\sin(\theta - \theta_{mn})\right|, \qquad (5.6)$$

$$\tan\theta_{mn} = \frac{1}{\cos\psi}\left(\frac{ma'}{nc^*} + \frac{a''}{c^*}\right), n = 0,1,2..., m = 0,\pm1,\pm2..., \qquad (5.7)$$

where ν and B_{res} is the observed frequency and resonance field, respectively, and a'-axis is the projection of *a*-axis to the plane perpendicular to the *b*-axis where a' can be obtain from $a' = a\sin\gamma$, and $c^* = c\sin\alpha\sin\beta^*$ is the interlayer distance between the *ab*-plane, and

$$\beta^* = \cos^{-1}\left[\frac{(\cos\alpha\cos\gamma - \cos\beta)}{\sin\alpha\sin\gamma}\right]$$

is the angle between a^* and c^*-axis. a'' can be obtain from $a''/c^* = -\cot\beta^*$. We note that if we assume ν=0, eq.(5.7) will be the only resonance condition for q1D POR which is identical to the q1D ADMRO's resonance condition (i.e. Lebed resonance, see section 3.2). This is why q1D POR is also called the high frequency ADMRO because it has a finite ν in eq.(5.6). In Fig. 5-9, we have arbitrary fit the resonance, which were observed in the *ac**-plane (Fig. 5-8), by a sinusoidal curve. The intersection of the two fitted sinusoidal curves with ν/B_{res}=0 in Fig. 5-9 is at the angle of θ=-8.4° and 10.6°. These angles must correspond to the angle θ_{mn} of eq.(5.7) with different combination of *m* and *n*. Using the lattice parameters a=6.699 Å, b=7.761 Å, c=15.776 Å, α=89.96° β=81.81° γ=78.19° of the observed sample, we obtain a'/c^*=0.42 a''/c^*=0.146 which will lead to the value of θ_{mn}=-15.3°, 8.3°, 29.5° when m/n=-1, 0, 1, respectively. These results do not completely coincide with the obtained angle, however, we think that these values are more or less consistent because of the lack of the data point and the observed angle may have an error of -5°~5°. Other thing to notice about Fig. 5-9 is that there seems to exist several sinusoidal curves with different amplitude. This suggests that several harmonics with different *m* and *n* combination are observed (*see* eq.(5.6)). By using the value obtained above, a'/c^*=0.42 a''/c^*=0.146, and an arbitrary value of Fermi velocity in eqs.(5.6) and (5.7), we can plot q1D POR curves with different combination of (*m,n*). Then, we have analyzed the observed resonance with the calculated q1D POR curves by changing the value of Fermi velocity. Fig. 5-11 shows the angle dependence of the observed resonance with the calculated q1D POR curves when Fermi velocity is fixed to v_F=2.7x10^4 m/s. The calculated q1D POR curves fit the most to the observed resonance when the Fermi velocity is 2.7x10^4 m/s. Here, we would like to stress that this is the most straightforward way to determine the Fermi velocity by the experiment. Now, we can clearly see that the observed resonance has its each origin with different (*m,n*). The largest resonance (circles) belongs to the (-1,1) resonance and the second largest resonance (squares) belongs to the (0,4) resonance. The other additional absorption seem to correspond to the (1,1) and (0,2) resonances.

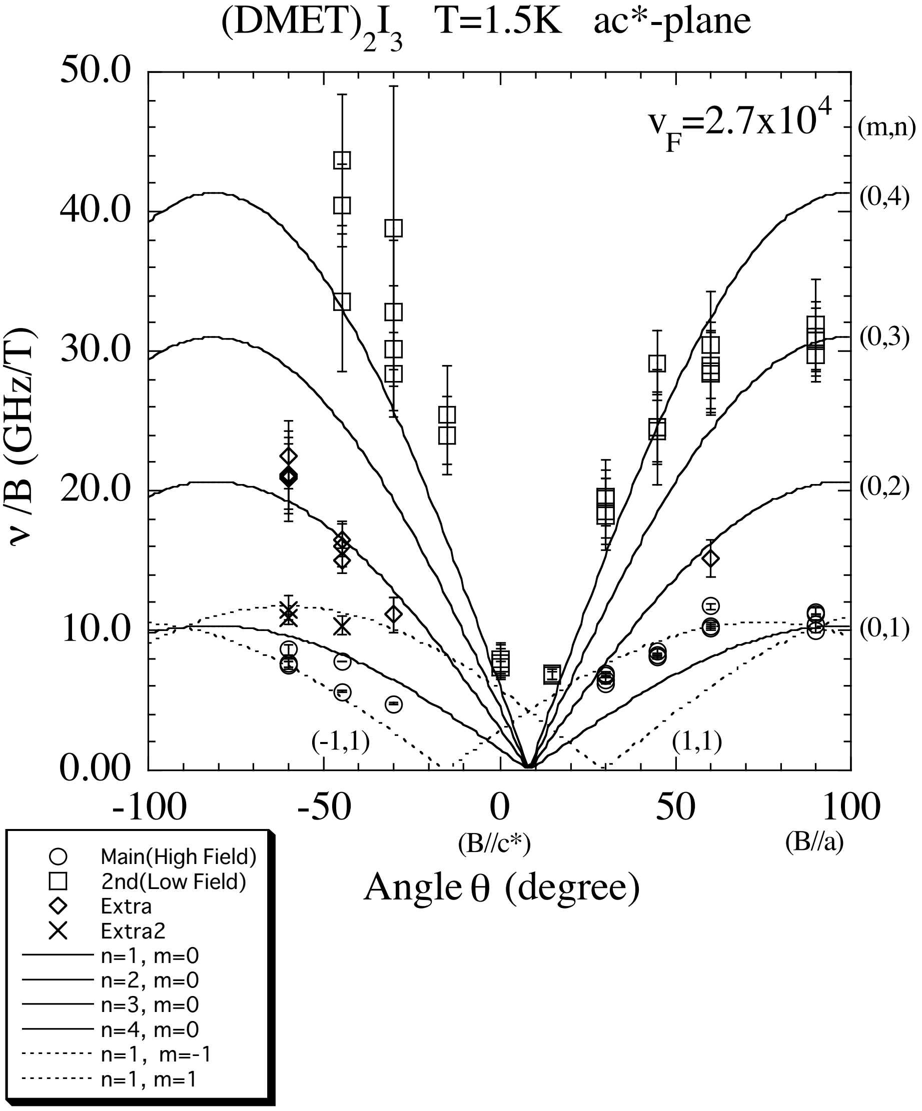

Fig. 5-11 The angle dependence of the observed resonance with the calculated q1D POR curves when Fermi velocity is 2.7×10^4 m/s. The resonance position is represented by the value of observed frequency divided by the resonance field. The solid curves is the calculated q1D POR curves of (*m,n*)=(0,1), (0,2), (0,3) and (0,4). The broken curves are for (*m,n*)=(-1,1) and (1,1).

These results, where (*m,n*)=(-1,1),(0,2),(0,4),(1,1) resonances are observed, are consistent with the ADMRO measurements results where Lebed resonance of *m*/*n*=-1,0,1 are observed [46,47]. It seems that the harmonic resonances are observed clearer when the field is rotated to the negative angle of θ. This may be due to the symmetry of the crystal which is triclinic in this case. However, it is a puzzle why the higher-order even harmonics such as (0,2) and (0,4) have been observed and the fundamental (0,1) resonance has not been observed. The amplitude for each (*m,n*) resonance seems to change considerably for each observed angle, for example, (1,1) resonance is observed only when θ=-45°,-60°. So, it might be the case that we could not observe the (0,1) resonance. However, from the experimental fact, we think that the observation of higher-order even harmonics is due to the FS topology of $(DMET)_2I_3$. The high-ordered harmonics come from the higher order Fourier components in the corrugation of the Fermi surface's sheet. If so, we have to consider how the FS looks like and to do this, we will consider the following generalized band model around the Fermi level for the q1D system:

$$E(k) = \hbar v_F(|k_x| - k_F) - \sum_{m,n} t_{mn}\cos(mbk_y + nck_z + \varphi_{mn}), \qquad (5.8)$$

where x-axis is the conducting axis, b and c are interchain distance along the y and z axis, φ_{mn} are phase factors. t_{mn} represents the effective interchain transfer integral and can be described as follows,

$$t_{mn} = 1/(m^2/t_b + n^2/t_c). \qquad (5.9)$$

By using eqs.(5.8) and (5.9), we can easily obtain the q1D FS. For example, if only the corrugations of (m,n)=(1,0),(0,1) are considered, we have the familiar q1D FS shape from $t_{10}=t_b$ and $t_{01}=t_c$ (Fig.5-12). We have taken the phase factors φ_{mn} to zero for the sake of clarity and the transfer integral ratio is taken as $t_a:t_b:t_c$=80:25:1 which is in good agreement with the conductivity results of $(DMET)_2I_3$.

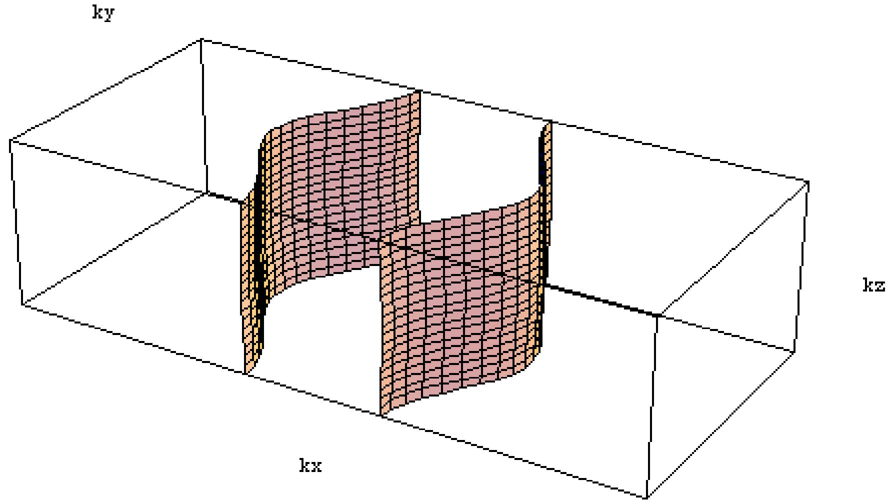

Fig. 5-12 Calculated q1D Fermi surface when only (m,n)=(1,0),(0,1) are considered. We used $t_a:t_b:t_c$=80:25:1

First, we will assume that only the corrugation (m,n) of q1D FS will appear in the q1D POR, which means that only (m,n)=(-1,1),(0,2),(0,4),(1,1) will be considered. Fig. 5-13 shows the calculated FS from eq.(5.8) where only (m,n)=(-

1,1),(0,2),(0,4),(1,1) are considered. We have taken the same transfer integral ratio used in Fig. 5-12 and the phase factors φ_{mn} are also taken to zero. In Fig. 5-13, we find quite complex corrugations of the FS and there are small peaks at the middle (i.e. $k_y=k_z=0$) and each corner (i.e. $(k_y,k_z)=(\pi/b,\pi/c),(\pi/b,-\pi/c),(-\pi/b,\pi/c),(-\pi/b,-\pi/c)$) of the FS. It can be easily guessed that the corrugations (-1,1), (1,1) have influences to those peaks and corrugations (0,2), (0,4) have influences to the direction parallel to the k_z-axis.

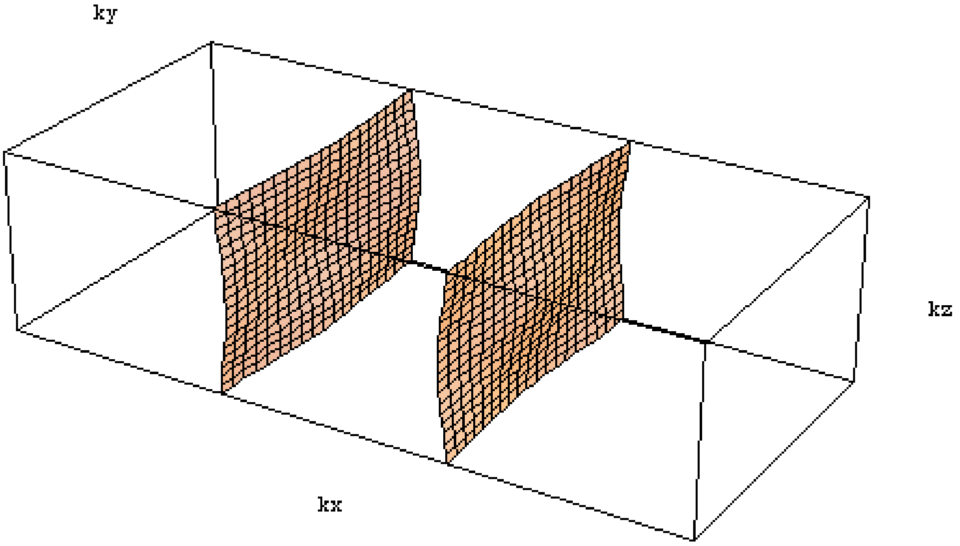

Fig. 5-13 Calculated q1D Fermi surface where only (m,n)=(-1,1),(0,2),(0,4),(1,1) are considered. We used $t_a:t_b:t_c$=80:25:1.

The biggest difference between Fig. 5-12 and Fig. 5-13 is the absence of the (1,0) corrugation. Theoretically, we can not observe the (1,0) resonance of q1D POR, because the (1,0) corrugation (i.e. $t_{10}=t_b$) does not contribute to the ac interlayer conductivity (see section 3.3.4). However, we can not ignore the transfer t_b which is relatively large. Therefore, we have to take into account also the (1,0) corrugation with other observed corrugations and this should represent the FS of $(DMET)_2I_3$. Fig. 5-14 is the estimated FS of $(DMET)_2I_3$ where we have consider the (m,n)=(-1,1),(0,2),(0,4),(1,1) and (1,0) corrugations and we have used the same transfer integrals ratio $t_a:t_b:t_c$=80:25:1. We note that the peaks observed in Fig. 5-13 are also visible in Fig. 5-14 and the peak on the k_x axis (i.e. $k_y=k_z=0$) is more apparent and jutted than the standard q1D FS which is shown in Fig. 5-12.

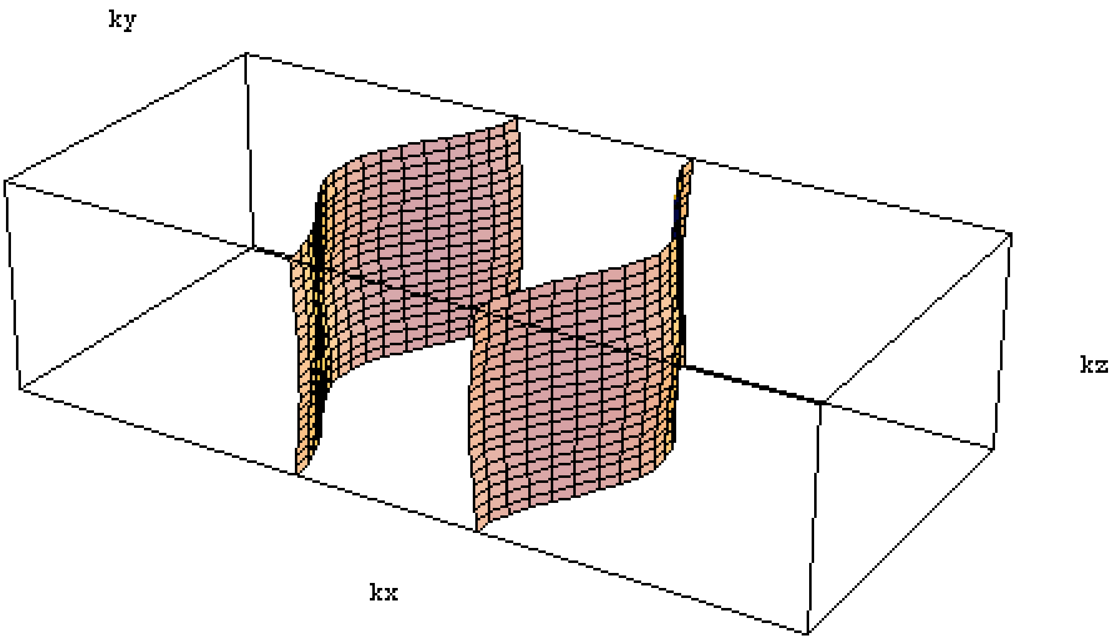

Fig. 5-14 Estimated q1D Fermi surface of $(DMET)_2I_3$. Only the corrugation (m,n)=(-1,1),(0,2),(0,4),(1,1) and (1,0) are considered, and the transfer integrals ratio t_a:t_b:t_c=80:25:1 is used.

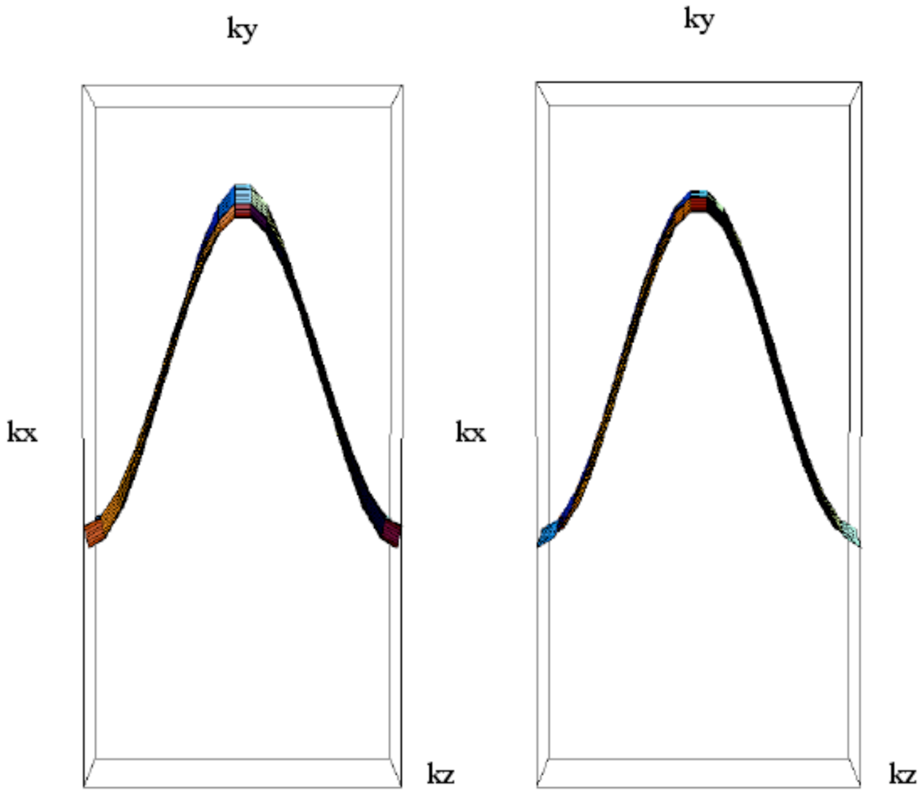

Estimated FS of $(DMET)_2I_3$
(m,n)=(-1,1),(0,2),(0,4),(1,1),(1,0)

Standard q1D FS
(m,n)=(0,1),(1,0)

Fig. 5-15 Two calculated FS, one is the estimated FS of $(DMET)_2I_3$ and the other is the standard q1D FS, viewed along the k_z-axis.

We have mentioned earlier that t_a/t_b~0.31 is obtained from the *ab*-plane results, this ratio means that $(DMET)_2I_3$ is more 2D than the well-known q1D organic conductors such as $(TMTSF)_2ClO_4$. We think that this relatively high t_a/t_b ratio and the (m,n)=(-1,1),(0,2),(0,4),(1,1) corrugations are the origin of the jutted peak. We show, in Fig. 5-15, the two calculated FSs (Figs 5-14 and 5-12) viewed along the k_z axis. We can clearly see that the peak in the estimated $(DMET)_2I_3$'s FS is more jutted than the standard q1D FS. Now, let me remind that third angular effect has been observed by Yoshino *et al.* in ADMRO measurements of $(DMET)_2I_3$ around the *b*-axis (see Fig. 5-10) and three humps in conductivity have been observed instead of one [48]. This result is different from other q1D organic conductor (e.g. $(TMTSF)_2ClO_4$ [57]) results and the jutted FS may play an important role to the observed humps. Moreover, the big difference in the behavior of Danner-Chaikin oscillation (2nd angular effect) between $(DMET)_2I_3$ (see Fig. 2-25) and $(TMTSF)_2ClO_4$ (see Fig. 3-6) may be due to the FS shape difference [46,47]. We note that the observation of q1D POR is a valuable technique for FS's topology studies because the Fourier component of the corrugations of the q1D FS, (m,n), can be obtained separately in contrast to the ADMRO measurements where only the value m/n is obtained, and the estimation of the transfer integral ratio t_a/t_b is also valuable for giving the idea of the FS's topology.

Finally, when the field is applied along the *a*-axis (i.e. $\theta=90^\circ$, $\psi=0^\circ$), the second largest absorption does not seem to fit well with the (0,4) resonance as shown in Fig. 5-11. Uji *et al.* have also reported the anomaly in the conductivity when the field is applied along the *a*-axis and they have explained the anomaly as follows [46,47]. When the field is applied along the *a*-axis, the Lorentz force causes the electrons on the warping q1D FS to move in the k_z direction. In real space, the electrons proceed along the *b*-axis, but sinusoidally oscillates along the *c**-axis. The amplitude of the sinusoidal motion is inverse proportional to the applied field, and when the field is strong enough, the amplitude of the sinusoidal motion becomes less than the layer spacing which means that the electron is effectively confined into a single conduction layer. In this case, the electron motion along the *c**-axis will be incoherent and should cause an anomaly on the conductivity [46,47,78]. We think also that this incoherent motion along the *c**-axis may possibly disturb the (0,4) resonance. However, the problem remains why the main resonance data for $\theta=90^\circ$ seem to fit well with the (-1,1) resonance (Fig. 5-11) and we need more precise angular dependence measurements to discuss about this behavior more deeply. This will remain as a subject for the future.

-Fermi velocity and scattering time-

As it was shown in Fig. 5-11, the observed resonances seem to fit well to the q1D POR curves when the Fermi velocity is set to 2.7x10^4 m/s. Here, we will discuss about this obtained Fermi velocity and the scattering time deduced from the line width.

First, we will compare the Fermi velocity obtained from other measurements. Unfortunately, there are no measurements in $(DMET)_2I_3$ which argue about the Fermi velocity. So we have to see other organic conductors. In magnetooptical measurements, Kovalev *et al.* have observed q1D POR in α-(BEDT-$TTF)_2KHg(SCN)_4$ and the Fermi velocity 6.5x10^4 m/s is obtained and this value is very close to the value obtained from fits to optical conductivity data using Drude model [16,79]. 8.0x10^4 m/s is obtained from the same organic conductors by ADMRO measurements under a strong electric field [80]. All of these data seem to be in a good agreement with our obtained Fermi velocity 2.7x10^4 m/s. However, if we use $v_F = \sqrt{2} t_b b / \hbar$ which is the Fermi velocity when the energy band is quarter filled, and assuming that t_b=80 meV b=7.761 Å for $(DMET)_2I_3$, we get 1.3x10^5 m/s which is an order of magnitude larger than the value obtained from the q1D POR measurements. We think that this difference occurs because we are probing the averaged Fermi velocity of the entire FS in a q1D POR measurements. Therefore, we think that the obtained value 2.7x10^4 m/s is consistent. Using a tight-binding approximation for the band dispersion, $E(k) = -2t_a \cos(ka)$, the effective mass is given by

$$m^* = \frac{\hbar}{a v_F} \tan(k_F a), \qquad (5.10)$$

where a is the lattice constant. If the band is quater-filled, eq.(5.10) becomes $m^* \cong \hbar / a v_F$ and such an estimate gives a value of m^*~$5.5 m_e$. The obtained value is rather larger than the effective mass obtained from q2D organic conductors. However, the obtained value is reasonable if the low dimensionality increases the effective mass. As SdH, dHvA and CR measurements are not possible in the q1D conductors, we would like to point out that this is the only way to estimate the effective mass in the q1D conductor. Anyway, we should stress that this q1D POR measurement gives the most straightforward way in the determination of the Fermi velocity as it was mentioned in Ref. 16 and the observation by this useful novel technique in other q1D organic conductors will remain as a subject for the future.

Finally, let us discuss about the scattering time. We have shown in section 3.3.4 that the scattering time can be obtained from the linewidth of the q1D POR. The obtained scattering time is approximately the same for each resonance where the average is $9.4\text{x}10^{-12}$ s. Here again, it is difficult to argue about the obtained scattering time because there exist little reports about the value of scattering time in the q1D organic conductor. However, Danner *et al.* have fitted the experimental data by the calculated ADMRO curves and deduced $\tau\sim4.3\text{x}10^{-12}$ s for $(\text{TMTSF})_2\text{ClO}_4$ [49] and Kovalev *et al.* have reported $\tau\sim1.5\text{x}10^{-11}$ s for α-(BEDT-$\text{TTF})_2\text{KHg(SCN)}_4$ [16]. We note that our obtained scattering time is about a half smaller than the value obtained from the q2D CR (i.e. $\sim2\text{x}10^{-11}$ s) and relatively similar to the value obtained from the q2D POR (i.e. $\sim6\text{x}10^{-12}$ s) (see section 4.4). Consequently, both the q1D and q2D POR are the resonant absorption of the interlayer ac conductivity and it seems that the scattering time turned out to be similar.

5.3. Conclusion

We have performed the magnetooptical measurements of q1D organic conductor $(\text{DMET})_2\text{I}_3$. and we have succeeded in observing the resonances coming from its q1D FS. The angular dependence of the resonance seems to show a characteristic behavior of q1D POR. For example, in the angular dependence of the *ab*-plane, we have observed the resonance which shifts to higher field as the angle ψ increases and the resonance has a 1/cosψ dependence which means that the resonance strongly depend on the magnetic field component parallel to the q1D FS. However, the resonance disappears above ψ=60° which suggests that the resonance disappears when the closed cyclotron orbits appear in the q1D FS. Hence, the carriers' trajectories, which is perpendicular to the applied magnetic field and parallel to the q1D FS sheets, need to be opened to observe q1D POR (i.e. the carriers' velocity need to be modulated). We have also obtained the ratio $t_a/t_b\sim0.31$

from the *ab*-plane angular dependence which is in good agreement with the conductivity results. On the other hand, we have observed a quite interesting resonance's behavior in the *ac**-plane measurements where *ac**-plane is parallel to the q1D FS. The resonance seems to fit well with the q1D POR curves and Fermi velocity $2.7\text{x}10^4$ m/s is obtained. The obtained Fermi velocity seems to be consistent with other salts, however, we have observed quite unusual higher-ordered harmonics which correspond to the $(m,n)=(0,2),(0,4)$ resonance. We think that these harmonics are related to the $(\text{DMET})_2\text{I}_3$'s FS and this FS seems to be different with well-known q1D FS such as $(\text{TMTSF})_2\text{ClO}_4$ or $(\text{TMTSF})_2\text{PF}_6$. The FS of $(\text{DMET})_2\text{I}_3$ seems to be more 2D and jutted to the *b*-axis which may be the origin of not having a SDW state in a low temperature region and the strange behavior in transport measurements around the *b*-axis. We have also showed numerically that the observation of Gor'kov-Lebed' CR is not possible for this salt and have showed that the oscillatory *H*-field should be applied to the conducting axis to observe q1D POR. We have also showed that the q1D POR observation is the most straightforward way to obtain the Fermi velocity and the scattering time, and (m,n) can be obtained separately compared to the ADMRO measurements where only the value m/n is obtained. In principle, observation of q1D POR is possible for all the sample where ADMRO have been observed because the origin of q1D POR and ADMRO are the same. Therefore, this technique will give us a new way for studying the FS topology.

6. Concluding Remarks

In this study, magnetooptical measurements of q1D and q2D organic conductors, which have simple FS, have been performed.

First, in q2D organic conductors, we have shown that the mechanism responsible for resonant absorption in some q2D organic conductors is quite different from the conventional CR and this novel resonance, which is named POR, is coming from the periodic modulation of the carrier's velocities due to the corrugated q2D FS. The obtained results for q2D conductors are as follows.

-θ-(BEDT-TTF)$_2$I$_3$-

CRs corresponding to the α and β orbits are observed. The angular dependence of CRs shows that both resonances are coming from the q2D FS which are in good agreement with SdH, dHvA and ADMRO results. Obtained effective masses for α and β orbits correspond to $1.0m_e$ and $2.1m_e$, respectively, which are about a half smaller than those obtained by SdH and dHvA measurements. The Kohn's theorem may be the origin of these differences which imply also that there exists not negligible electron-electron interaction in the system.

-(BEDT-TTF)$_2$Br(DIA)-

Higher-order harmonic resonances, up to the 7th order, have been observed for the first time in organic conductors. The observed resonance is assigned as a POR which arises from a q2D elliptic FS and these results are in good agreement with ADMRO results. The obtained effective mass $4.7m_e$ is also consistent with the SdH measurements which may suggest that the effective mass is enhanced for POR and is different from the conventional CR masses.

-(BEDT-TTF)$_3$Br(pBIB),(BEDT-TTF)$_3$Cl(DFBIB)-

CR and POR were observed for (BEDT-TTF)$_3$Br(pBIB) and (BEDT-TTF)$_3$Cl(DFBIB), respectively. The obtained effective masses are $1.0m_e$ and $2.9m_e$ for (BEDT-TTF)$_3$Br(pBIB) and (BEDT-TTF)$_3$Cl(DFBIB), respectively, and these results clearly suggest that Kohn's theorem is valid when CR is observed and the effective mass for POR is enhanced.

From these results, we found that the selection of the observation between POR and CR is due to the difference of interlayer skindepth (i.e. dc conductivity) for each sample. In principle, POR must be observed in all q2D conductors due to its anisotropic conductivity. However, if the interlayer skindepth is small and the oscillatory *E*-field is applied correctly parallel to the conducting plane, it is possible to observe conventional CR. We found also that the effective mass of CR is about a half smaller and the scattering time is an order of magnitude larger than those obtained from SdH measurements. This difference of the effective mass suggests that Kohn's theorem is valid for organic conductors which are q2D system, and not negligible electron-electron interaction exists in the system. On the other hand, effective mass and scattering time of POR are consistent with those obtained from SdH measurements which suggests that a mass enhancement for POR's effective mass is due to the many-body effect. The reason why Kohn's theorem is not valid in POR, may be due to the difference of probing in-plane conductivity (i.e. CR) or interlayer conductivity (i.e. POR).

Next, in q1D conductors, magnetooptical measurements of $(DMET)_2I_3$ have been performed and we succeeded in observing the resonances coming from its corrugated q1D FS. The observed resonances can be attributed to q1D POR from the angular dependence parallel to q1D FS sheets. The Fermi velocity 2.7×10^4 m/s is obtained from the q1D POR fitting which seems to be in a good agreement with other results, however, quite unusual higher-order harmonics were also observed. These unusual higher harmonics seem to be coming from the characteristic FS of $(DMET)_2I_3$. Furthermore, the transfer integral ratio $t_a/t_b \sim 0.31$ has been obtained from the angular dependence measurement in the *ab*-plane. This suggests that the FS of $(DMET)_2I_3$ is more 2D than the well-known q1D organic conductors, such as $(TMTSF)_2ClO_4$ or $(TMTSF)_2PF_6$, which may be the cause of not having SDW in a low temperature region.

As seen above, the q1D POR gives us valuable information about the q1D FS and it is the most straightforward way to obtain the Fermi velocity and the scattering time of q1D organic conductors, and the integers (m,n), which are the Fourier components of the corrugated FS, can be obtained separately in contrast with the ADMRO measurements in which only the value m/n is obtained.

In summary, q1D and q2D organic conductors show rich varieties of physics in the magnetooptical measurements and we conclude that CR, POR and q1D POR can be observed in q2D and q1D conductors, respectively.

We have mentioned earlier that this study has started from when Akioka *et al.* have observed four resonances in magnetooptical measurements of α-(BEDT-TTF)$_2$KHg(SCN)$_4$ [9], however, the assignment of these resonances could not be established. In addition, some groups have reported the observation of q1D POR in magnetooptical measurements of α-(BEDT-TTF)$_2$KHg(SCN)$_4$ [13,16] and reported also that the observed resonances which thought to be CRs were in fact q2D POR [3,12]. However, we believe, from this study, that the resonances observed by Akioka *et al.* are CRs coming from the q2D FS. The reasons are as follows, first, the angular dependence of CRs show a q2D behavior which is inconsistent if it is q1D POR. Secondly, the observed four resonances do not show harmonic behavior such as q2D POR. Finally, the measurements have been performed by using the transmission technique which means that the electromagnetic environment around the sample is not controlled and the observation of POR (ac interlayer conductivity) is coincidental. Therefore, the four resonances should not appear all the time, if it is a POR.

However, it is still difficult to assign the observed four CRs to the FS of α-(BEDT-TTF)$_2$KHg(SCN)$_4$. If all the resonances are coming from independent orbits, this means that there exist multi-pockets FS, however, this model contradicts with the observation of q1D POR. Recently, we are also working if these multiple resonances could be explained from one closed orbit FS, and the multiple resonances are due to the incoherent spin-splitting of the Landau levels. If so, it will be in a good agreement with q1D POR results. At the moment the determination of the FS is still difficult, and it remains as a subject for the future.

Moreover, recent interest has excited the question whether the organic conductors possess true 3D FS (i.e. warped cylindrical FS) or whether the interlayer transport is incoherent [81,82]. McKenzie and Moses have proposed that the FS of BEDT-TTF salts are not necessary extended in the interlayer direction and showed that the phenomena such as ADMRO and q1D/q2D POR do not necessarily imply FS which are extended in the interlayer direction; alternative 'weakly incoherent interlayer transport', in which a quasiparticle tunnels coherently between adjacent layers but is scattered before subsequent tunneling processes, can give rise to similar phenomena [75,81]. Some SdH, dHvA measurements report the beats in quantum oscillation arising from the minimum and maximum of the cross-sectional area of q2D FS (i.e. coherent interlayer transport), however, these observations are still extremely rare.

It is difficult to conclude from this present study if the interlayer transport is incoherent or not. However, it is true that some anomalies appear when the magnetic field is applied parallel to the conducting layer. For example, in $(DMET)_2I_3$, the (0,4) resonance is shifted to higher field when the field is applied along the *a*-axis, or no CR are observed when the magnetic field is thought to be applied perpendicular to the FS sheet (i.e. closed orbits should appear). All these results may suggest that the interlayer transport is incoherent.

In this study, we have shown that the magnetooptical measurement is now a powerful tool for FS studies and is developing to other fields. And we hope that this study will shed some lights for further studies.

References

[1] D. Jérome, A. Mazaud, M. Ribault and K. Bechgaard, J. Physique Lett. **41** (1980) L 95.

[2] T. Ishiguro, K. Yamaji and G. Saito, *Organic Superconductors* (Springer, 1998).

[3] J. Singleton, Rep. Prog. Phys. **63** (2000) 1111.

[4] G. Dresselhaus, A. F. Kip and C. Kittel, Phys. Rev. **92** (1953) 827.

[5] M. Ia. Azbel' and E. A. Kaner, J. Exptl. Theoret. Phys. (U.S.S.R.) **30** (1956) 811; Soviet Phys. JETP **3** (1956) 772.

[6] T. Sasaki, H. Sato and N. Toyota, Synth. Met. **42** (1991) 2211.

[7] P. Christ, W. Bilberacher, M. V. Kartsovnik, E. Steep, E. Balthes, H. Weiss and H. Müler, JETP Lett. **71** (2000) 303.

[8] K. Miyagawa, A. Kawamoto and K. Kanoda, Phys. Rev. B **56** (1997) R8487.

[9] K. Akioka, H. Ohta, S. Kimura, S. Okubo, K. Kanoda and M. Motokawa, Physica B **246-247** (1998) 311.

[10] J. Singleton, F. L. Pratt, M. Doporto, T. J. B. M. Janssen, M. Kurmoo, J. A. A. J. Perenboom, W. Hayes and P. Day, Phys. Rev. Lett. **68** (1992) 2500.

[11] W. Kohn, Phys. Rev. **123** (1961) 1242.

[12] S. Hill, Phys. Rev. B **55** (1997) 4931.

[13] A. Ardavan, J. M. Schrama, S. J. Blundell, J. Singleton, W. Hayes, M. Kurmoo, P. Day and P. Goy, Phys. Rev. Lett. **81** (1998) 713.

[14] C. Palassis, M. Mola, J. Tritz, S. Hill, S. Uji, K. Kawano, M. Tamura, T. Naito and H. Kobayashi, Synth. Met. **120** (2001) 999.

[15] J. M. Schrama, J. Singleton, R. S. Edwards, A. Ardavan, E. Rzepniewski, R. Harris, J. Schlueter, M. Kurmoo and P. Day, J. Phys. C. M. **13** (2001) 2235.

[16] A. E. Kovalev, S. Hill and J. S. Qualls, Phys. Rev. B **66** (2002) 134513.

[17] M. -H. Whangbo, W. M. Walsh, R. C. Haddon and F. Wudl, Solid State Commun. **43** (1982) 637.

[18] P. M. Grant, Phys. Rev. B **26** (1982) 6888.

[19] T. Mori, A. Kobayashi, Y. Sasaki and H. Kobayashi, Chem. Lett. (1982) 1923.

[20] T. Mori, A. Kobayashi, Y. Sasaki, H. Kobayashi, G. Saito and H. Inokuchi, Bull. Chem. Soc. Jpn. **57** (1984) 627.

[21] T. Mori, Bull. Chem. Soc. Jpn. **71** (1998) 2509.

[22] T. Mori, H. Mori and S. Tanaka, Bull. Chem. Soc. Jpn. **72** (1999) 179.

[23] T. Mori, Bull. Chem. Soc. Jpn. **72** (1999) 2011.

[24] H. Kobayashi, R. Kato, A. Kobayashi, Y. Nishio, K. Kajita and W. Sasaki, Chem. Lett. (1986) 789.

[25] H. Kobayashi, R. Kato, A. Kobayashi, Y. Nishio, K. Kajita and W. Sasaki, Chem. Lett. (1986) 833.

[26] H. Kobayashi, R. Kato, A. Kobayashi, S. Moriyama, Y. Nishio, K. Kajita and W. Sasaki, Synth. Met. **27** (1988) A283.

[27] A. Kobayashi, R. Kato, H. Kobayashi, S. Moriyama, Y. Nishio, K. Kajita and W. Sasaki, Chem. Lett. (1986) 2017.

[28] M. Tamura, H. Tajima, H. Kuroda and M. Tokumoto, J. Phys. Soc. Jpn. **59** (1990) 1753.

[29] T. Terashima, S. Uji, H. Aoki, M. Tamura, M. Kinoshita and M. Tokumoto, Solid State Commun. **91** (1994) 595.

[30] M. Tamura, K. Yakushi, H. Kuroda, A. Kobayashi, R. Kato and H. Kobayashi,

J. Phys. Soc. Jpn. **57** (1988) 3239.

[31] M. Tokumoto, A. G. Swanson, J. S. Brooks, M. Tamura, H. Tajima and H. Kuroda, Solid State Commun. **75** (1990) 439.

[32] M. Tokumoto, N. Kinoshita, H. Anzai, A. G. Swanson, J. S. Brooks, S. T. Hannahs, C. C. Agosta, M. Tamura, H. Tajima, H. Kuroda, A. Ugawa and K. Yakushi, Synth. Met. **41-43** (1991) 2459.

[33] M. Tokumoto, A. G. Swanson, J. S. Brooks, C. C. Agosta, S. T. Hannahs, N. Kinoshita, H. Anzai, M. Tamura, H. Tajima, H. Kuroda, A. Ugawa and K. Yakushi, Physica B **184** (1993) 508.

[34] M. Tamura, H. Kuroda, S. Uji, H. Aoki, M. Tokumoto, A. G. Swanson, J. S. Brooks, C. C. Agosta, and S. T. Hannahs, J. Phys. Soc. Jpn. **63** (1994) 615.

[35] K. Kajita, Y. Nishio, T. Takahashi, W. Sasaki, R. Kato, H. Kobayashi, A. Kobayashi and Y. Iye, Solid State Commun. **70** (1989) 1189.

[36] T. Terashima, S. Uji, H. Aoki, M. Tamura, M. Kinoshita and M.Tokumoto, Synth. Met. **70** (1995) 845.

[37] H. M. Yamamoto, J. Yamaura and R. Kato, J. Mater. Chem. (1998) 15.

[38] H. M. Yamamoto, J. Yamaura and R. Kato, J. Am. Chem. Soc. **120** (1998) 5905.

[39] H. M. Yamamoto, R. Maeda, J. Yamaura and R. Kato, J. Mater. Chem. **11** (2001) 1034.

[40] S. Uji, C. Terakura, T. Terashima, H. Aoki, H. M. Yamamoto, J. Yamaura and R. Kato, Synth. Met. **103** (1999) 1978.

[41] S. Uji, *unpublished.*

[42] S. Yasuzuka, C. Terakura, T. Terashima, T. Yakabe, Y. Terai, H. M. Yamamoto, R. Maeda, R. Kato and S. Uji, *unpublished.*

[43] K. Kikuchi, K. Murata, Y. Honda, T. Namiki, K. Saito, T. Ishiguro, K. Kobayashi and I. Ikemoto, J. Phys. Soc. Jpn. **56** (1987) 3436.

[44] M. Z. Aldoshina, L. O. Atovmyan, L. M. Gol'denberg, O. N. Krasochka, R. N. Lyubovskaya, R. B. Lubovskii and M. L. Khidekel', Dokl. Akad. Nauk SSSR **289** (1986) 1140.

[45] H. Yoshino, K. Saito, K. Kikuchi, H. Nishikawa, K. Kobayashi and I. Ikemoto, J. Phys. Soc. Jpn. **64** (1995) 2307.

[46] S. Uji, C. Terakura, T. Terashima, H. Aoki, H. Nishikawa, I. Ikemoto and K. Kikuchi, *Proceedings of PPHMF III*, World Scientific (1998) 277.

[47] S. Uji, C. Terakura, T. Terashima, H. Aoki, H. Nishikawa, I. Ikemoto and K. Kikuchi, *4th Int. Symposium on Advanced Physical Fields: Quantum Phenomena in Advanced Materials at High Magnetic Fields* (1999) 295.

[48] H. Yoshino, K. Murata, T. Sasaki, K. Saito, H. Nishikawa, K. Kikuchi, K. Kobayashi and I. Ikemoto, J. Phys. Soc. Jpn. **66** (1997) 2248.

[49] G. M. Danner, W. Kang and P. M. Chaikin, Phys. Rev. Lett. **72** (1994) 3714.

[50] D. Shoenberg, *Magnetic Oscillations in Metals* (Cambridge University Press, 1984).

[51] M. V. Kartsovnik, P. A. Kononovich, V. N. Laukhin and I. F. Shchegolev, Pis'ma Zh. Eksp. Teor. Fiz. **48** (1988) 498. [JETP Lett. **48** (1988) 541.]

[52] K. Yamaji, J. Phys. Soc. Jpn. **58** (1989) 1520.

[53] R. Yagi, Y. Iye, T. Osada and S. Kagoshima, J. Phys. Soc. Jpn. **59** (1990) 3069.

[54] T. Osada, S. Kagoshima and N. Miura, Phys. Rev. B **46** (1992) 1812.

[55] S. J. Blundell and J. Singleton, Phys. Rev. B **53** (1996) 5609.

[56] T. Osada, A. Kawasumi, S. Kagoshima, N. Miura and G. Saito, Phys. Rev. Lett. **66** (1991) 1525.

[57] T. Osada, S. Kagoshima and N. Miura, Phys. Rev. Lett. **77** (1996) 5261.

[58] T. Osada, H. Nose and M. Kuraguchi, Physica B **294-295** (2001) 402.

[59] K. Kanki and K. Yamada, J. Phys. Soc. Jpn. **66** (1997) 1103.

[60] S. Hill, J. S. Brooks, Z.Q. Mao and Y. Maeno, Phys. Rev. Lett. **84** (2000) 3374.

[61] S. Hill, *private communication.* There is a mistake on eq.(6) of Ref.[12] and the prefactors of Ω_1 and Ω_2 must be switched.

[62] M. Motokawa, H. Ohta and N. Makita, Int. J. Infrared Millimeter Waves **12** (1991) 149.

[63] H. Ohta, M. Sumikawa, K. Kita, M. Motokawa, T. Seixas and J. M. Machado da Silva, Physica B **216** (1996) 341.

[64] K. Koyama, M. Yoshida, H. Nojiri, T. Sakon, D. Li, T. Suzuki and M. Motokawa, J. Phys. Soc. Jpn. **69** (2000) 1521.

[65] C. P. Poole, Jr., *Electron Spin Resonance, A comprehensive treatise on experimental techniques, Second edition* (Dover, 1997).

[66] O. Klein, S. Donovan, M. Dressel and G. Grüner, Int. J. Infrared Millimeter Waves **14** (1993) 2423; S. Donovan, O. Klein, M. Dressel and G. Grüner, *ibid* **14** (1993) 2459; M. Dressel, O. Klein, S. Donovan and G. Grüner, *ibid* **14** (1993) 2489.

[67] M. Mola, S. Hill, P. Goy and M. Gross, Rev. Sci. Insrum. **71** (2000) 186.

[68] S. Hill, Phys. Rev. B **62** (2000) 8699.

[69] The EPR signal linewidth for θ-(BEDT-TTF)$_2$I$_3$ is around 1 mT at 4.2 K, *see* Y. Oshima, Master thesis (Kobe University, 2000).

[70] Y. Oshima, N. Nakagawa, K. Akioka, H. Ohta, S. Okubo, M. Tamura, Y. Nishio and K. Kajita, Synth. Met. **103** (1999) 1919.

[71] Y. Oshima, H. Ohta, S. Okubo, K. Koyama, M. Motokawa, M. Tamura, Y. Nishio and K. Kajita, Physica B **294-295** (2001) 431.

[72] H. Kobayashi, R. Kato, A. Kobayashi, T. Mori, H. Inokuchi, Y. Nishio, K. Kajita and W. Sasaki, Synth. Met. **27** (1988) A289.

[73] M.Ya. Azbel' and E.A. Kaner, Zh. Eksp. Teor. Fiz. **32** (1956) 896. [Sov. Phys. JETP **5** (1957) 730.]

[74] L.P. Gor'kov and A.G. Lebed', Phys. Rev. Lett. **71** (1993) 3874.

[75] R. H. McKenzie and P. Moses, Phys. Rev. B **60** (1999) R11241.

[76] K. Akioka, Master thesis (Kobe University, 2000).

[77] H. Schwenk, K. Andres and F. Wudl, Phys. Rev. B **29** (1984) 500.

[78] S. P. Strong, D. G. Clarke and P. W. Anderson, Phys. Rev. Lett. **73** (1994) 1007.

[79] M. Tamura, R. Masuda, T. Naito, H. Tajima, H. Kuroda and A. Kobayashi, Synth. Met. **41-43** (1991) 2499.

[80] K. Kobayashi, E. Ohmichi and T. Osada, J. Phys. Chem. Solids **63** (2002) 1267.

[81] R. H. McKenzie and P. Moses, Phys. Rev. Lett. **81** (1998) 4492.

[82] P. Moses and R. H. McKenzie, Phys. Rev. B **60** (1999) 7998.

List of Publications

1. "Cyclotron resonance study of θ-$(BEDT\text{-}TTF)_2I_3$"
Y. Oshima, N. Nakagawa, K. Akioka, H. Ohta, S. Okubo, M. Tamura, Y. Nishio and K. Kajita
Synthetic Metals **103** (1999) 1919-1920.

2. "Circularly polarized cyclotron resonance measurement system and its application to BEDT-TTF salts"
H. Ohta, Y. Oshima, N. Nakagawa, K. Akioka, S. Okubo and K. Kanoda
Synthetic Metals **103** (1999) 1913.

3. "Fermi surface study of θ-$(BEDT\text{-}TTF)_2I_3$ by cyclotron resonance measurements"
Y. Oshima, H. Ohta, S. Okubo, K. Koyama, M. Motokawa, M. Tamura, Y. Nishio and K. Kajita
Synthetic Metals **120** (2000) 853-854.

4. "High-field magnetooptical measurements of BEDT-TTF salts"
Y. Oshima, H. Ohta, S. Okubo, K. Koyama, M. Motokawa, M. Tamura, Y. Nishio and K. Kajita
Physica B **294-295** (2001) 431-434.

5. "Observation of direct transition in S=1/2 quantum spin system $Cu_2(C_5N_{12}N_2)_2Cl_4$ by high field ESR"
H. Ohta, Y. Oshima, T. Sakurai, S. Okubo, T. Tanaka, K. Koyama, M. Motokawa, H. Kikuchi, H. Nagasawa and J. P. Boucher
J.Magnetism and Magnetic Materials **226-230** (2001) 439-440.

6. "Magnetism of C_{60}-based molecular complexes: High field magnetisation and magneto-optical study"
S. V. Demishev, N. E. Sluchanko, L. Weckhuysen, V. V. Moshchalkov, H. Ohta, S. Okubo, Y. Oshima and N. G. Spitsina
Physics of the Solid State **44** (2002) 425.

7. "Magnetooptical measurements of BEDT-TTF salts containing supramolecular assemblies"
Y. Oshima, H. Ohta, H. M. Yamamoto, R. Kato, K. Koyama and M. Motokawa
Synth. Met. **130** (2002) -, *in press.*

8. "High field ESR and magneto-optical measurements in millimeter and submillimeter wave regions"
H. Ohta, S. Okubo, Y. Oshima, T. Sakurai, M. Saruhashi, Y. Uwatoko, K. Koyama, M. Motokawa, H. M. Yamamoto and R. Kato
Proceedings of IRMMW 2001.

9. "ESR studies of BEDT-TTF organic conductors containing supramolecular assemblies"
Y. Oshima, H. Ohta, H. M. Yamamoto and R. Kato
EPR in the 21st century (Elsevier Science B.V., 2002), p.312

10. "Observation of high order harmonic resonances in magneto-optical measurements of $(BEDT\text{-}TTF)_2Br(DIA)$"
Y. Oshima, H. Ohta, K. Koyama, M. Motokawa, H. M. Yamamoto and R. Kato
J. Phys. Soc. Jpn. **71** (2002) 1031.

11. "Magnetooptical measurements of quasi-one-dimensional conductor $(DMET)_2I_3$"
Y. Oshima, H. Ohta, K. Koyama, M. Motokawa, H. Nishikawa, K. Kikuchi and I. Ikemoto
Proceedings of ICSM 2002. *to be published in* Synth. Met.

12. "Fermi surface study of quasi-two-dimensional organic conductors by magnetooptical measurements"
Y. Oshima, H. Ohta, K. Koyama, M. Motokawa, H. M. Yamamoto, R. Kato, M. Tamura, Y. Nishio and K. Kajita
J. Phys. Soc. Jpn. **72** (2003) 143.

Acknowledgments

The present work has been done under the guidance of Professor Hitoshi Ohta. The author would like to express sincere gratitude for many valuable discussions, advices and encouragement.

The author would like to thank to Professor Takao Nanba and Professor Keisuke Tominaga for accepting to be the jury of this thesis and their suggestions and comments were very helpful to achieve this work. The author would also like to express sincere gratitude to Dr. Shinya Uji (National Institute for Materials Science) for accepting to be the jury of my thesis and for many valuable suggestions and helpful discussions. This work has not been completed without his excellent transport measurements data and valuable suggestions.

The author would like to acknowledge Assistant Professor Keita Kishigi (Kumamoto University) for enlightening discussions and encouragement. His stay in Kobe during three months was very helpful and important for me. The author is also grateful to Assistant Professor Keiichi Koyama (HFLSM, IMR Tohoku University) for letting me to use the MVNA in HFLSM and giving me advices and encouragement. This work has not been done without his help and his guidance.

The author gratefully acknowledges Dr. Masafumi Tamura, Dr. Hiroshi M. Yamamoto and Dr. Reizo Kato of RIKEN for providing me many attractive samples, valuable discussions and encouragement. The author would like to thank also Dr. Hiroyuki Nishikawa, Assistant Professor Koichi Kikuchi, Professor Isao Ikemoto of Tokyo Metropolitan University and Professor Yutaka Nishio, Professor Koji Kajita of Toho University for providing very attractive and interesting samples.

The author would also like to thank all the colleagues in Kobe University. Thanks to Dr. S. Okubo for helping me the experiment done in Kobe and to Dr. Y. Inagaki, Dr. T. Kunimoto and Dr. M. Kuwabara for their encouragement and technical advices. The author is also grateful to Dr. T. Sakurai-san and M. Kimata-kun for helping me the experiment done in HFLSM and for valuable discussions. The work has not been achieved without their help, many thanks. And many thanks also to Soryu-san (S. Takeda), Y. Miura, K. Hazuki, J. Yoshikawa, K. Kirita, K. Kawakami, T. Kamikawa, M. Saruhashi, Y. Nagasaka, D. Fukuoka, T. Hirano, K. Hiraka and others.

The author gratefully acknowledges also Dr. A. Ardavan (University of Oxford), Professor J. S. Brooks (NHMFL, FSU), Professor. S. V. Demishev (GPI, Russian Academy), Assistant Professor S. Hill (University of Florida) and Assistant Professor T. Osada (ISSP, University of Tokyo) for valuable and helpful discussions.

Also many thanks to all my friends especially Dr. T. Fujita, Dr. K. Enomoto, Dr. H. Tanaka, Dr. T. Koyama, M. Seiho, T. Yagi, T. Gotoh, K. Nishida, T. Matsuo, Y.

Takahashi, A. Ueda, C. Urakawa, R. Maji, K. Horiyama and other friends I've forgotten.

Finally, I am profoundly grateful to my family to keep me encouraging and supporting me during my study.

Yugo Oshima

Kobe, February 2003

Corresponding author.
Yugo Oshima (yugooshima@mac.com),
The Graduate School of Science and Technology, Kobe University,
Rokkodai 1-1, Nada, Kobe 657-8501, Japan.
Tel.: +81-78-803-5656
Fax: +81-78-803-5770
e-mail: yugo@phys.sci.kobe-u.ac.jp
The PDF version of this doctoral thesis is also available at *http://homepage.mac.com/yugooshima/*